Strange Particle Production In Awayside Jets In High P_T π^0 And Direct Photon Triggered Events In π^- + Be/Cu Interactions At 515 GeV.

By

John P. Bacigalupi

February 1996

DISSERTATION

Submitted in partial satisfaction of the requirements for the degree of

DOCTOR OF PHILOSOPHY

in

Physics

in the

GRADUATE DIVISION

of the

UNIVERSITY OF CALIFORNIA

DAVIS

Approved:

.....

.....

.....

Abstract

Fermilab experiment E706 studies high P_T interactions in pion–nucleon collisions using copper and beryllium targets at an incident energy of 0.5 TeV. The experiment uses a liquid argon calorimeter to detect and trigger on high P_T electromagnetic showers. We report on the fragmentation properties of jets with leading K^0_{short}, Λ or $\overline{\Lambda}$ in high P_T π^0 and direct photon triggered events. The strange particles are reconstructed via the charged decay modes: $K^0_{short} \rightarrow \pi^+ \pi^-$, $\Lambda \rightarrow \mathrm{p}\ \pi^-$, and $\overline{\Lambda} \rightarrow \overline{p}\ \pi^+$. Proportional wire chambers and straw tube drift chambers are used to reconstruct strange particle decays upstream of the center of the dipole analysis magnet.

To my wife, Chungsue, for all her love and support.

Acknowledgements

There are many people who have helped me over the past six years to bring this thesis to a conclusion. First and foremost is my wife, Chungsue. During most of the work that went into this thesis, I was working at Fermilab in Batavia, IL. I was completely focused during the next four years on the work that I was doing there. As a result, I neglected just about everything else including most of my responsibilities at home. For four long years my wife quietly took up the slack. Now that this thesis is complete, it is time for us to finally start our lives together.

I would like to thank my advisor, David Pellett, without whose help this thesis would not be possible. When I first came to U.C. Davis from Santa Cruz, I went to work for Dave doing radiation damage studies in his lab. I was fortunate enough to work for him as a research assistant during my first year of graduate courses. During this time I learned about setting up a small experiment, executing it, and analyzing the data. Finally, when it was time to find a thesis experiment, Dave got me into a first rate collaboration out at Fermilab.

I would also like to thank Sudhindra Mani for his guidance and support while I was out at Fermilab. Mani was a big help when it came time to start doing the physics that was necessary to complete my thesis. He also made my introduction to the experiment a very smooth experience.

Once out at Fermilab, I was fortunate to work with many excellent graduate students, post docs, and professors from a variety of universities. I am especially grateful to Steve Blusk. Steve was kind enough to introduce me to the basic principles of work on a real life particle physics experiment. He taught me most of what I know about particle tracking and our particle tracking system at Meson West.

I am grateful to Professor Gene Engels, with whom I spent my first Thanksgiving holiday out at Fermilab. Gene was always a pleasure to talk to and had many entertaining stories to tell.

I am also grateful to Lee Sorrell for teaching me all I know about the trigger system (a little knowledge can be a dangerous thing, Lee) and also introducing me to the Midwest Martial Arts Academy in Naperville, IL.[1]. We had a lot of fun together both on the experiment and throwing each other around in karate class.

I would like to thank David Striley for teaching me about the Cerenkov detector. Dave is a good friend and hopefully is still working out.

I reserve a special thanks to Andre Maul. Andre and I worked together for about two years on the alignment of the downstream tracking system. Andre

[1]Currently called the Eagle Academy of Martial Arts in Warrenville, IL.

taught me a lot about alignment as well as generally how the straw chambers and proportional wire chambers worked. Also thanks to Professor Bill Toothacker who was helpful in getting me started with the alignment program and answered many of the questions that I had when I started this monumental task.

Just about every thesis that comes out of E706 has a reference to George Ginther in the Acknowledgements and there is good reason for that. George knows plenty about every aspect of the experiment and has taught me something about just about everything. I found George to be extremely patient and even when under tremendous time presure, he will always take time out to explain something to a student (or a professor). I don't expect to meet many George Ginthers in my lifetime.

My thanks to Michael Begel, for being a good friend and doing the energy scale. This was one of the few projects that I believe to be more difficult than the alignment. Thanks also, Michael, for your help with TEX and other computer related issues.

I would also like to thank Woohyun Chung for his help and tutorledge regarding the E706 jet reconstruction program. This code was invaluable to this thesis and with Woohyun's help I was able to modify it quickly to incorporate strange particle finding.

My fellow graduate students including, Lenny Apanasevich, Paoti Chang, Wiesiek Dlugosz, Lucy de Barbaro, Woohyun Chung, Rob Roser, Nikos Varelas,

George Osborne, Dhammika Weerasundara, and Vishnu Zutshi deserve a special thanks for all their help and for the good times we've had. Lenny, I really hope the knicks can win a championship some day (unless their playing against the Warriors, of course).

Among those which I consider "honorary" graduate students which I would like to thank are Leonard Nelson, our building manager at Meson West, and Dan Ruggiero, the other guy (Just kidding Dan). Dan and I shared many an early morning at Meson West. Dan is a great guy with a great sense of humor.

I would also like to thank Vijay Kapoor for his help with my thesis topic. Vijay accelerated my introduction to strange quark analysis issues and his thesis was a guide book in which I could find the answer to many of my questions.

I would like to thank the following post docs at mwest for answering my questions and making my experience at mwest an enjoyable one: Dave Brown, Bill Desoi, Jim Dunlea, Casey Hartman, Jan Ftacnik, Chris Lirakis, John Mansour, Dane Skow, Carlos Yosef, and Marek Zielinski.

Finally, I would like to thank the various professors associated with E706 including, Carl Bromberg, Tom Ferbel, and Paul Slattery.

Contents

List of Tables

List of Figures

Chapter 1

Introduction and Theoretical Motivation

1.1 The Data Set

This thesis presents results from the 1990-91 run of the E706 fixed target experiment at Fermilab. E706 is a second generation direct photon experiment designed specifically to measure the production of high transverse momentum (P_T) direct photons and neutral mesons in proton-nucleon and pion-nucleon interactions. This analysis concentrated on the 1990 data sample (see table 1.1.)

SUMMARY OF E706 DATA SETS

Run	Interaction	Beam Momentum (GeV/c)	Number of Events	Sensitivity (events/pb)
1988	π^-Be	500	2×10^6	0.5
	π^-Cu			0.1
	(p,π^+)Be		3×10^6	0.75
	(p,π^+)Cu			0.1
1990	π^-Be	515	30×10^6	8.6
	π^-Cu			1.4
1991	pBe	800	23×10^6	7.3
	pCu			1.8
	pH			1.5
	(p,π^+)Be	530	14×10^6	6.4
	(p,π^+)Cu			1.6
	(p,π^+)H			1.3
	π^-Be	515	4×10^6	1.4
	π^-Cu			0.3
	π^-H			0.3

Table 1.1: Summary of data taken by the E706 experiment during the 1988 and 1990-1991 fixed target runs at Fermilab.

1.2 Introduction

The interactions of quarks and gluons are difficult to investigate due to confinement and other properties of the strong interaction. Because of the confinement mechanism we can not examine the properties of partons directly. Instead we must rely on indirect measurements such as the study of hadron jets.

According to Quantum Chromodynamics (QCD), quarks and gluons can only appear in colorless combinations. This means that they can appear in either a color-anticolor combination (meson) or a combination which includes all three colors (baryon) or all three anticolors (anti-baryon). States which contain gluons only (glue balls) are also predicted. When a quark or gluon scatters from the interaction with another quark or gluon, it begins to radiate gluons as it moves away from the site of the interaction. These gluons split into quark-antiquark pairs and radiate more gluons and finally form the colorless mesons and baryons which are detected in our spectrometer. In order to study QCD we must infer the properties of the original struck parton by reconstructing the final state particles of the hadron jet. What we want to study are quarks and gluons; what we get are jets of hadrons.

1.3 Quarks, Gluons, And QCD

Quantum Chromodynamics (QCD) postulates that all hadronic matter is made of quarks. It describes the strong interaction with a local non-abelian gauge

theory[1]. The quarks are fundamental representations of SU(3) $\otimes$ SU$(n_f)_C$. There are n_f flavors $\otimes$ three colors of quarks [2]. The gauge bosons which mediate the strong force are called gluons. The gluons come in eight bicolored varieties each with a different color-anticolor combination. Quarks come in fractional electric charges of $-1/3|\ e\ |$ or $2/3|\ e\ |$ while the anti-quarks have charges of $1/3|\ e\ |$ and $-2/3|\ e\ |$. The electric charges of the quarks, however, are not predicted by QCD but rather are input into the standard model. The various flavors and charges of the six known quarks along with their mass estimates are listed in table 1.2 [22].

QCD is modeled after the highly successful theory of electromagnetic interactions, Quantum Electrodynamics (QED). The fine structure constant of QED, $\sqrt{\alpha}$, is replaced by $\sqrt{\alpha_s}$ in QCD calculations. Like QED, the scattering amplitudes are represented by Feynman diagrams. The basic vertices are shown in figure 1.1. As in QED, the various scattering amplitudes which are used in cross section calculations are expanded in a perturbation series.

Quark Flavor	Electric Charge (e)	Mass Estimate (GeV/c^2)
d (down)	$-1/3$	0.0099 ± 0.0011
u (up)	$+2/3$	0.0056 ± 0.0011
s (strange)	$-1/3$	0.199 ± 0.033
c (charm)	$+2/3$	1.35 ± 0.05
b (bottom)	$-1/3$	~ 5
t (top)	$+2/3$	174 ± 10

Table 1.2: Physical properties of quarks.

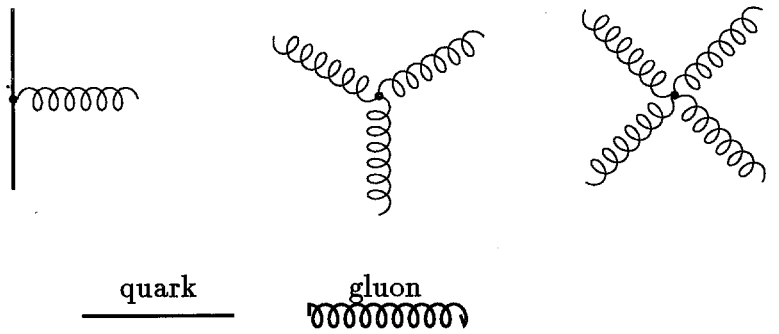

Figure 1.1: Elementary vertices of QCD.

One problem that arises in QCD calculations is that of infrared and collinear divergences. Terms like $E_{\bar{q}}E_g(1-cos\theta_{\bar{q}g})$ can appear in denominators. These terms originate from the assumption that the quarks and gluons are massless. These terms vanish if the emitted gluon is soft (infrared) or the gluon is emitted collinear to the quark. This problem is handled by the process of regularization [3].

In QED the fine structure constant α is the parameter used for the expansion i.e. we have terms of order α, α^2, α^3, etc. The value of α is approximately equal to $\frac{1}{137}$. Unlike QED where the value of α can be fixed directly by coulomb scattering, the determination of α_s is very difficult. It is conventional to write the following relation for α_s:

$$\alpha_s(Q^2) = \frac{12\pi}{(33-2f)ln(\frac{q^2}{\Lambda^2})} \tag{1.1}$$

This equation is only valid for $q^2 \gg \Lambda^2$[2]. The value of Λ is typically chosen to be

between 0.2 and 0.4 GeV. α_s is referred to as a running coupling constant. In order for the perturbation series to converge the value of the momentum transfer, q^2, must be very large. This fact alludes to the situations known as asymptotic freedom and confinement. Asymptotic freedom refers to the situation that the quarks seem to be "free" at short distances. The quarks are confined within the hadron.

1.4 Hadron Jets

Hadron jets are one of the consequences of confinement. When a photon or gluon with a large q^2 value interacts with a quark in a hadron, that quark will gain enough momentum to seperate from the other quark(s). As it seperates it will begin to radiate gluons. These gluons will split into quark–antiquark pairs which radiate more gluons until the energy drops below the threshold to create a quark–antiquark pair. These quarks will bind together in some complicated way to form mesons and baryons [15]. Perturbative QCD, because of the running coupling constant, is only a useful description of the quark-quark or quark-gluon interactions when the distances involved are small. Because the fragmentation of quarks into jets of hadrons is not a short range phenomena, it can not be explained by perturbative QCD.

In order to study jet production it is necessary to use a phenomenological model. If we consider the reaction $A + B \rightarrow C + X$ we can write down the following formula:

$$E_C \frac{d^3\sigma}{dp_C^3}(A+B \to C+X) = \sum_{abcd} \int dx_a dx_b dz_c \delta(\hat{s}+\hat{t}+\hat{u}) \frac{\hat{s}}{z_c^2 \pi} \times G_{a/A}(x_a, M_d^2) G_{b/B}(x_b, M_d^2) \frac{d\sigma}{d\hat{t}}(ab \to cd) D_{C/c}(z_c, M_f^2) \tag{1.2}$$

$\frac{d\sigma}{d\hat{t}}(ab \to cd)$ is the parton level hard scattering cross section, and $\hat{s}$, $\hat{t}$ and $\hat{u}$ are the parton level Mandelstam variables defined by the following relations:

$$\begin{aligned} \hat{s} &= (p_a + p_b)^2 \\ \hat{t} &= (p_a - p_c)^2 \\ \hat{u} &= (p_b - p_c)^2 \end{aligned} \tag{1.3}$$

Where p_A, p_B, and p_C are the hadron momenta and $p_a = x_a p_A$, $p_b = x_b P_B$, $p_c = P_C/z_c$ are the parton momenta. The G functions are called parton distribution functions. $G_{a/A}$ is the probability of parton a having fraction x_a of the original hadron A's momentum. Similarly $G_{b/B}$ is the corresponding probability for parton b. $D_{C/c}$ is called the fragmentation function. $D_{C/c}$ is the probability that, in the jet, the hadron C will have a fraction z_c of the original struck quark's momentum. The fragmentation function is used as a tool for understanding jets. A schematic diagram of this formula is shown in figure 1.2. The parton distribution and fragmentation functions must be measured experimentally. It is assumed that they are invariant with respect to the type of process we use to measure their properties. In this way we can use results from deep inelastic scattering experiments for the quark distribution functions and fragmentation functions from e^+e^- annihilation[4].

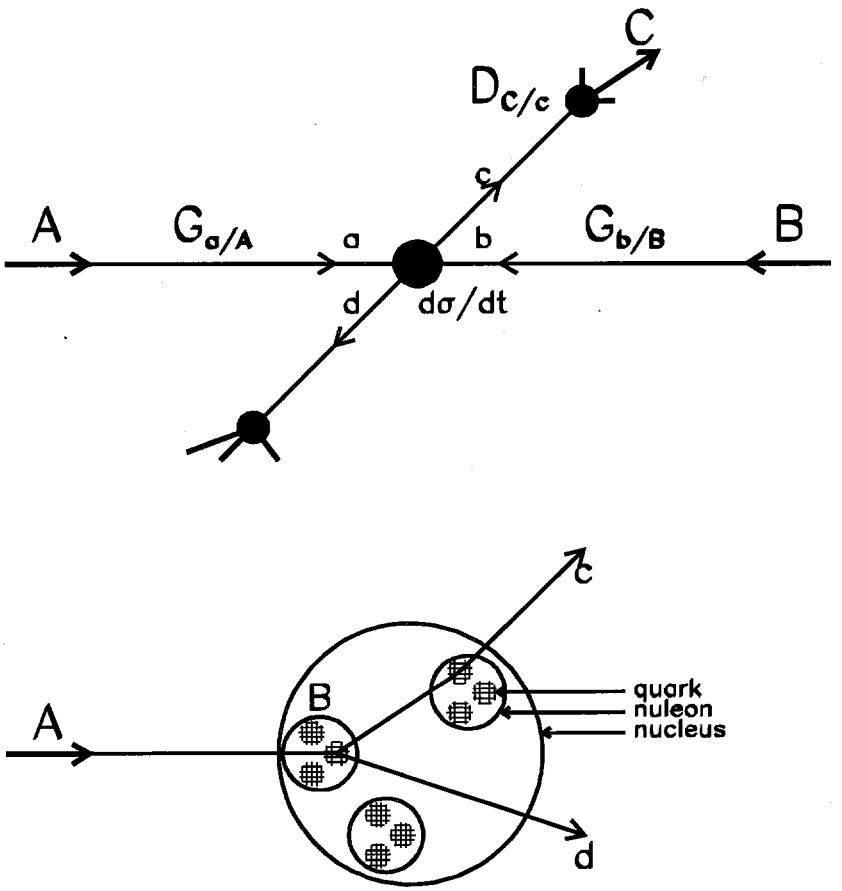

Figure 1.2: Top: A hadron hadron collision. Bottom: A hadron nucleus collision.

1.5 The HERWIG Monte Carlo

The data presented in this thesis will be compared with the predictions of the HERWIG Monte Carlo event generator. HERWIG is an acronym for Hadron Emission Reactions With Interfering Gluons. HERWIG is a general purpose particle physics event generator. It includes a simulation of hard lepton-lepton, lepton-hadron, and hadron-hadron scattering and soft hadron-hadron scattering in one package. It uses the parton shower approach for initial and final state QCD radiation. It includes color coherence effects and azimuthal correlations both within and between jets. Whereas other simulations sum the leading collinear singularities for initial and final state radiation and in some cases the leading infrared contributions from outgoing partons, HERWIG is the first simulation to take into account both the infrared and collinear contributions to both the incoming and outgoing partons [7]. In this way the HERWIG Monte Carlo uses a complete description of the asymptotic behavior (order α_s) of the parton distributions.

HERWIG uses a cluster hadronization model which is local in color and independent of the hard process and the energy. The clusters are fragmented into hadrons [8].

1.6 Direct Photons

As mentioned above, quarks have an electric charge as well as a color charge.

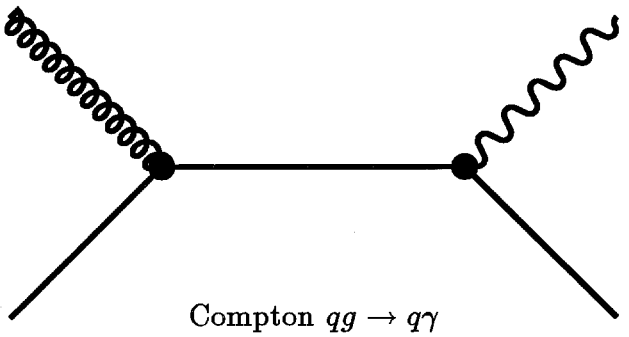

Compton $qg \rightarrow q\gamma$

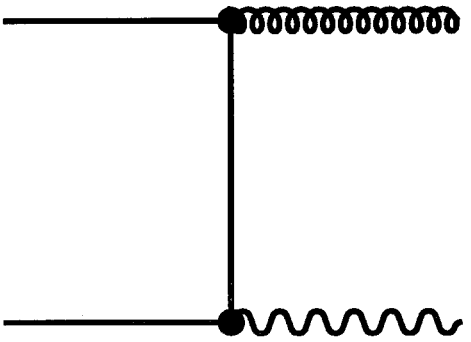

Annihilation $q\bar{q} \rightarrow g\gamma$

Figure 1.3: First Order Sub-Proceses of Direct Photon Production

This means that quarks interact with photons directly. This fact is very useful because it simplifies many areas of study. For example in the reaction $A+B \rightarrow \gamma+X$ we eliminate the fragmentation term $D_{C/c}$ from equation 1.3 since photons do not fragment (considering only up to order $\alpha\alpha_s$ contributions) like quarks and gluons. To first order there are two processes contributing to direct photon production: (See figure 1.3.)

- Compton gq $\rightarrow \gamma$q

$$\frac{d\sigma_{comp}}{d\hat{t}} = -\frac{\pi\alpha\alpha_s}{\hat{s}^2} \times \frac{e_q^2}{3} \times [\frac{\hat{u}}{\hat{s}} + \frac{\hat{s}}{\hat{u}}] \tag{1.4}$$

- annihilation q$\bar{q} \rightarrow \gamma$g

$$\frac{d\sigma_{anni}}{d\hat{t}} = \frac{\pi\alpha\alpha_s}{\hat{s}^2} \times \frac{8e_q^2}{9} \times [\frac{\hat{u}}{\hat{t}} + \frac{\hat{t}}{\hat{u}}] \tag{1.5}$$

Direct photons are photons which come directly from the hard scatter, parton-parton interaction. These are not to be confused with photons coming from other sources such as meson decays. Direct photons carry off the total momentum of the hard scatter. This is unlike the case in which a parton is the scattered particle. The scattered partons as discussed above, will fragment and in general many hadrons will share the momentum of the struck parton.

The main source of background to the direct photon signal comes from the decay $\pi^0 \rightarrow \gamma\gamma$ in which one of the photons is not reconstructed. A π^0 can fail to be reconstructed for several reasons:

- One of the photons goes out of the geometrical acceptance.
- A highly asymmetric π^0 decay occurs. One photon has a small enough energy that it is not reconstructed in the calorimeter.
- The two photons have a very small separation and they coalesce in the calorimeter.

The relationship between the angle between the two photons from a symmetric π^0 decay is $\theta_{\gamma\gamma} \cong \frac{2m_\pi}{E_\pi}$.

One way of looking at the contribution that the π^0 decays make to the reconstructed photon sample is to plot the $\frac{\gamma}{\pi}$ vs. P_T distribution (see figure 1.4). Because the direct photon will carry the total transverse momentum of the interaction while the π^0 will share this momentum with other particles in the jet, a signature for direct photons is that the $\frac{\gamma}{\pi}$ will increase with P_T.

1.7 Advantages Of Studying Direct Photon Triggered Events

Naively, since momentum is conserved, one should be able to calculate the momentum of the outgoing quark by summing the momenta of the hadrons in the reconstructed jet. In practice, due to rapidity holes in the coverage of the detectors, inefficiencies, finite resolution, etc. it is extremely difficult to reconstruct

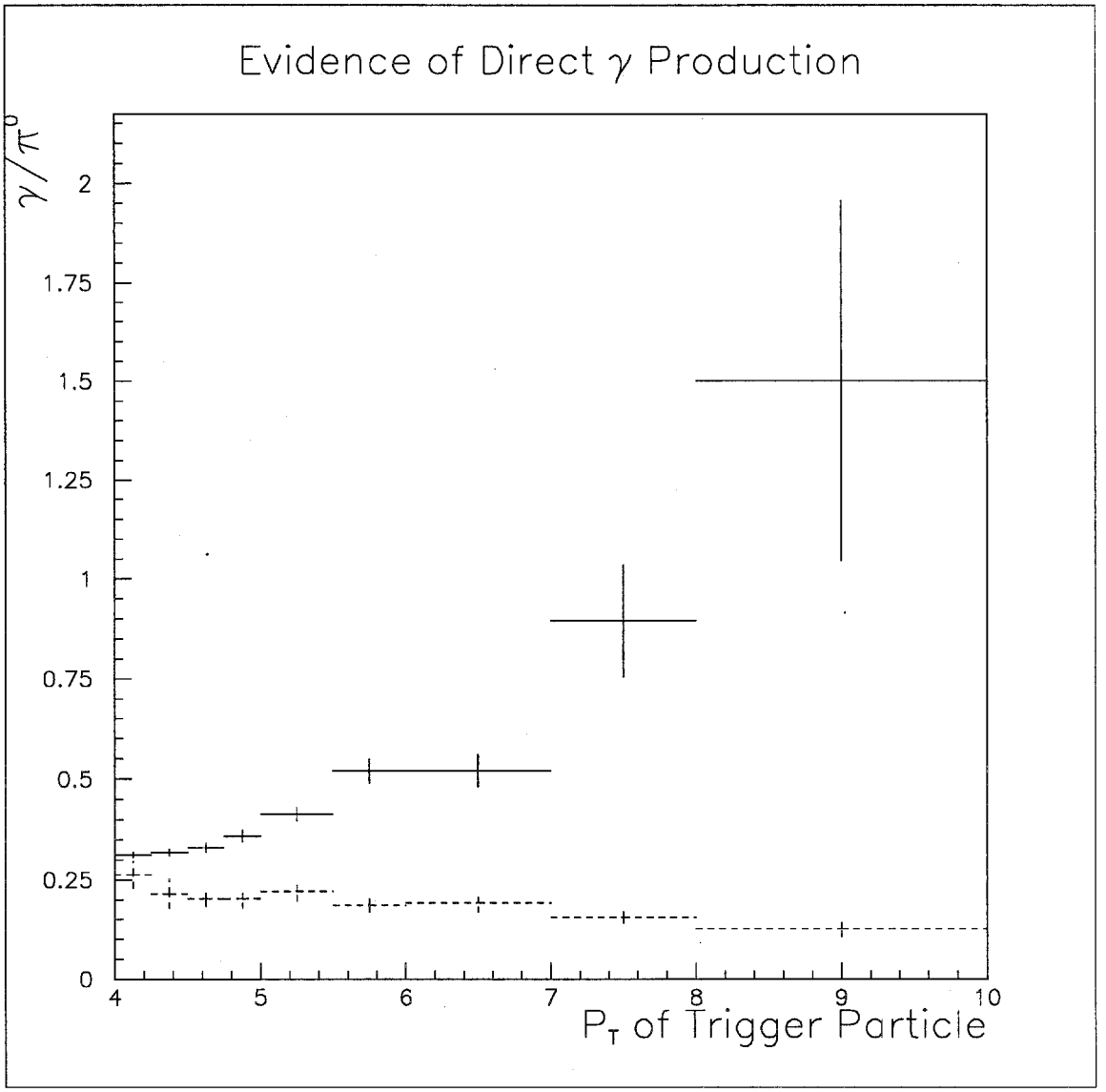

Figure 1.4: γ/π^0 for data (solid) and HERWIG Monte Carlo. The Monte Carlo generates no direct photons so that all single photons in the $\frac{\gamma}{\pi^0}$ are decay photons from misreconstructed π^0's.

all of the hadrons. Other things we would like to know include what the parton level subprocess was that produced the jets. Unfortunately, for π^0 production for example, there are many subprocesses that can contribute[5].

Direct photon events give us a handle on some of these difficulties. As mentioned previously, to first order there are only two subprocess which can contribute to direct photon production. Another advantage mentioned above is that, to order $\alpha\alpha_s$, the direct photon does not fragment: It goes straight from the interaction into our spectrometer. This gives us a direct probe into the dynamics of the hard scatter. Direct photons give us information about the recoil side opposite the photon. Since momentum must be conserved we know the momentum of the recoil jet (neglecting effects due to the intrinsic transverse momentum of the scattered partons, k_T).

Different beam particles give us different relative contributions of the Compton and annihilation subprocesses. For example, using a π^- beam on a nuclear target introduces a $\bar{q}q$ at the valence level. This increases the likelihood of an annihilation subprocess. The relative contributions are P_T dependent (see figures 1.5 and 1.6.) This can be understood by considering the x distributions of the valence quarks, gluons, and sea quarks. The valence quarks have the hardest distributions followed by the gluons and finally the sea quarks. In π^-p interactions, for example, with increasing P_T we would expect a larger contribution of the annihilation with respect to the Compton subprocess. This is because in the Compton diagram we need an initial state gluon in the interaction. This gluon will on average carry a

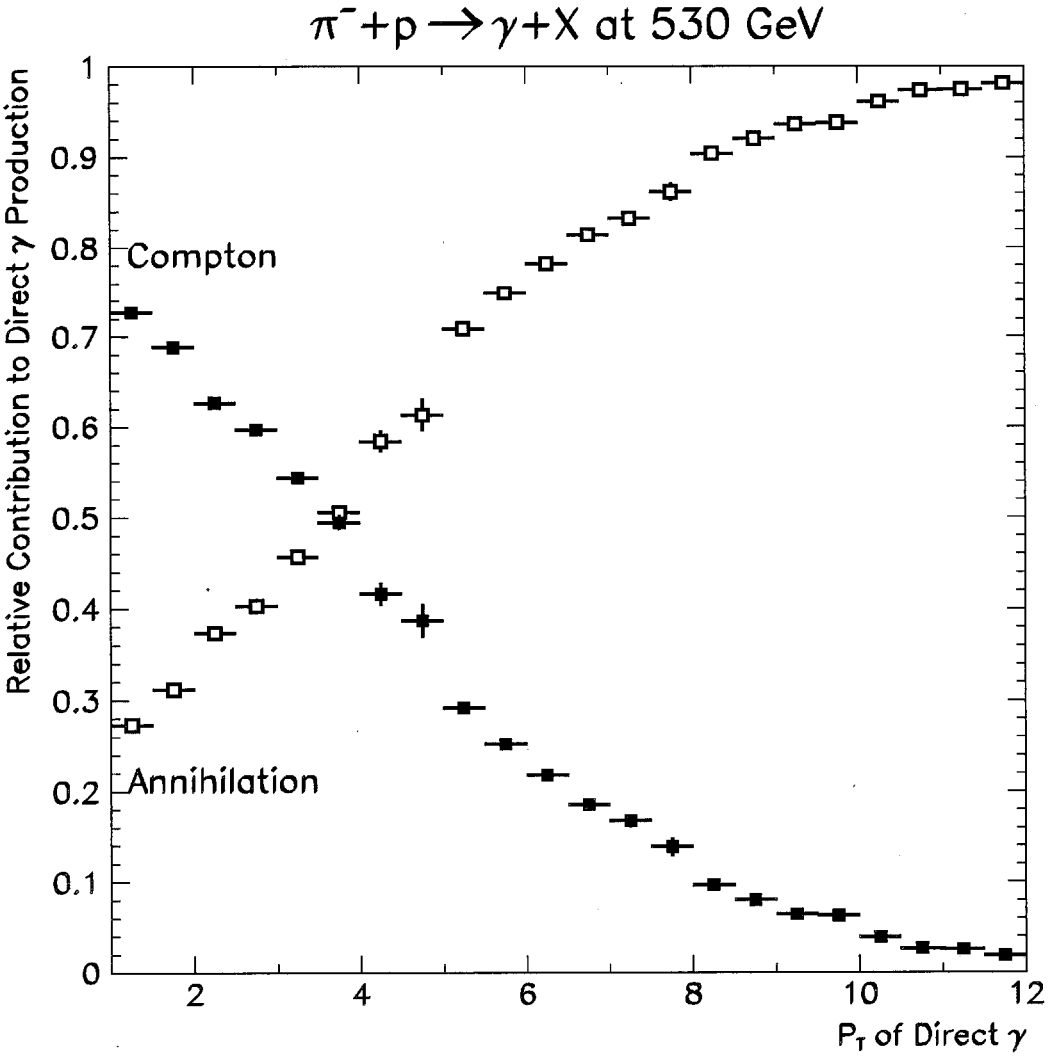

Figure 1.5: Relative contributions of Compton and annihilation sub-processes in direct photon events vs P_T of the direct photon. The figure shows that at high values of direct photon P_T the annihilation subprocess dominates in π^-p$\rightarrow \gamma$+X. These results are HERWIG Predictions

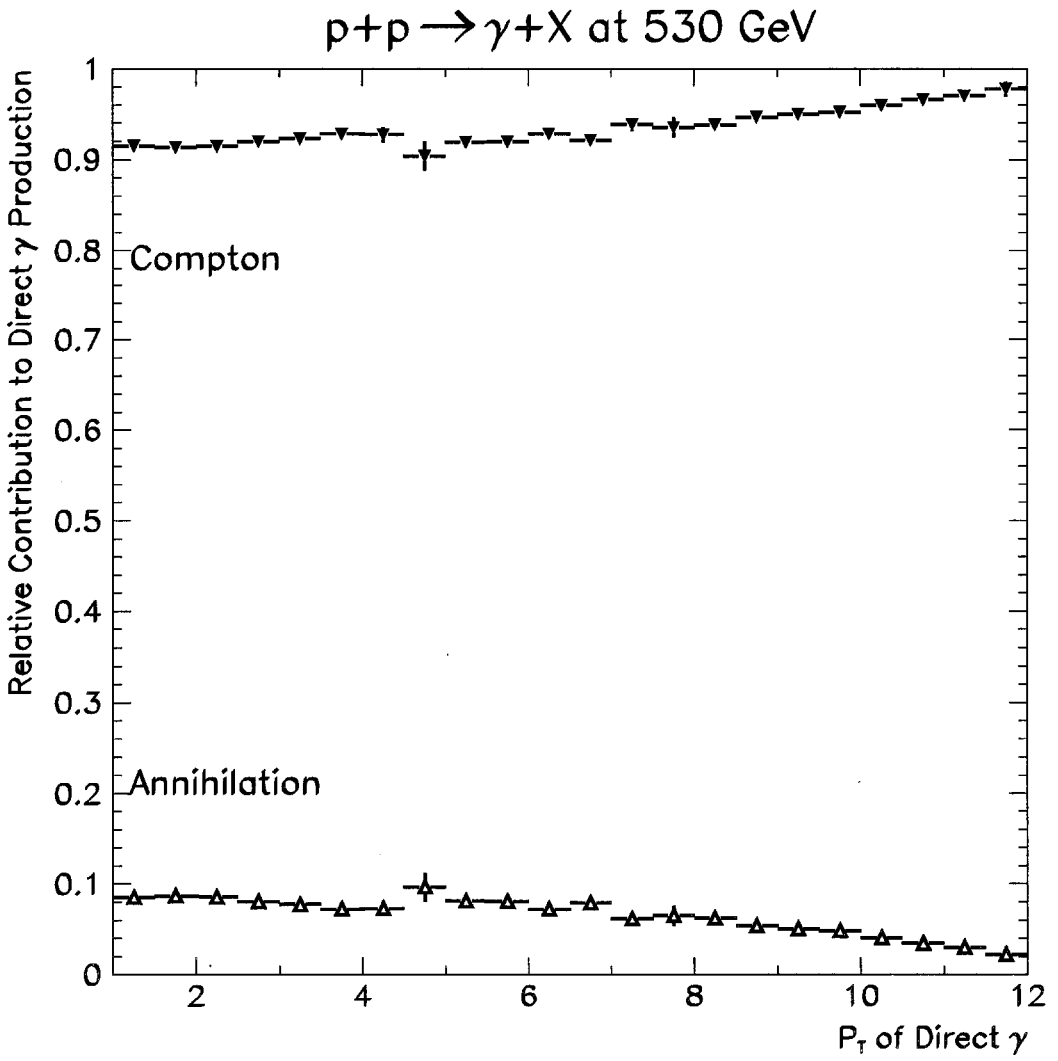

Figure 1.6: Relative contributions of Compton and annihilation sub-processes in direct photon events vs P_T of the direct photon. The figure shows that for pp$\rightarrow \gamma$+X the Compton diagram dominates. These results are HERWIG predictions.

smaller amount of momentum than the valence anti-quark of the π^-. At higher P_T we expect a $\bar{q}q$ interaction to be more likely. This situation is reversed in pp interactions. In this case there are no valence anti-quarks available. Since gluons have a harder distribution than sea quarks it is more likely that a gluon will participate in a high P_T event than a sea anti-quark.

We can use this information to study quark and gluon jets. With a π^- beam incident on a nucleon target, we expect an increasingly larger percentage of gluon recoil jets at larger values of direct photon P_T.

1.8 High P_T π^0 And Direct γ Triggered Events

Although the concept of a direct photon is simple enough, experimentally there are certain difficulties which much be addressed. First of all we must be able to show some differences between direct photon events and events triggered by a $\pi^0 \rightarrow \gamma\gamma$ decay. We can use some intuitive concepts to guide us.

For reasons mentioned above, a direct photon will come out of the interaction alone. In a π^0 triggered event we expect that since the π^0 is one of many hadrons in the trigger jet it will be accompanied by other particles. To look for differences in this area we can make a plot of the $\Delta\phi$ distribution between the high P_T trigger particle and the rest of the particles in the event [20]. As we increase the minimum required P_T for the trigger particle we begin to observe a qualitative difference between the

π^0 and single photon triggered events. The direct photons in the sample cause the values near $\Delta\phi = 0$ to be enhanced relative to larger angles.

In proton-proton interactions, due to the e_q^2 term in the cross section formula, we expect the recoil jet to have a more positive net charge in direct photon production than in high P_T events with a hadron trigger[5].

Comparisons can be made between the Cosθ^* distributions of π^0 and direct photon triggered events. Θ^* is defined as the angle that the awayside jet makes with respect to the boost axis in the center of momentum frame. Because both of the first order diagrams responsible for direct photon production contain quark (fermion) propagators, we expect a $1/(1 \pm \cos\theta^*)$ dependence. On the other hand most of the Feynman graphs responsible for π^0 production contain gluon (boson) propagators. In this case we expect a $1/(1 \pm cos\theta^*)^2$ dependence. As a result the cosθ^* distribution for direct photon triggered events should be flatter than the distribution for π^0 triggered events.

1.9 Recent Strange Particle Experimental Results

The study of strange particles can provide theoretical insight into many of the currently open questions in high energy physics. This section is meant to serve as a summary of some of the most recent investigations.

1.9.1 Strange Particle Multiplicities

One of the important outstanding questions in the Standard Model is $\frac{s}{u}$: the strange quark suppression with respect to the lighter up and down quarks. Many Monte Carlo generators have this ratio as an input parameter. Multiplicity distributions are often plotted as a function of X_{Bj}, W^2, E, Q^2, X_f, etc. These plots are compared to Monte Carlo predictions with different $\frac{s}{u}$ values. There is remarkable agreement between experiments with different incident particles [11, 13, 12, 9, 15]. The consensus is that an $\frac{s}{u}$ of between 0.2-0.3 produces good agreement between Monte Carlo and data. The variation is due to a possible beam energy dependence.

Another parameter of interest is the relative strange diquark suppression $(\frac{us}{ud})(\frac{d}{s})$. This parameterizes the suppression associated with the production of a strange diquark in contrast to the production of a diquark composed of lighter quarks. Typical values of this parameter range from 0.4 to 0.59 [11, 13, 12, 9, 15].

It is currently believed that Λ baryons are produced by a combination of the target spectator quarks (diquark) and strange quarks from the sea. Multiplicity distributions plotted as a function of $X_f = \frac{2p_l}{\sqrt{s}}$ indicate that Λ's are peaked more backward than K^0's or $\bar{\Lambda}$'s which are peaked in the central region [12, 13, 11]. In fact experiment E665 (a muon-nucleon experiment) shows that the ratio $\frac{\langle n_\Lambda \rangle}{\langle n_{\bar{\Lambda}} \rangle}$ is consistent with unity for $X_f > 0$.

1.9.2 Λ Polarization

Since the Λ and $\bar{\Lambda}$ are spin $\frac{1}{2}$ objects [22], it is possible that under certain conditions, that they may be produced polarized.

Convenient axes are chosen to measure this polarization. For example, a typical convention for Λ's produced via the strong interaction is the following: The y axis is chosen in the $\vec{p}_{beam} \otimes \vec{p}_{\Lambda}$ direction. The beamline is the z axis and the x axis is perpendicular to y and z. An angle Θ is defined as the angle between the decay proton and the relevant axis. The fraction of Λ's as a function of Θ is given by [11] $\frac{df}{d(cos\Theta)} \propto (1 + \alpha P cos\Theta)$, where $\alpha = 0.642$ is the weak decay parameter [11] of the Λ. The polarization, P, is extracted as the slope in a plot of $\frac{df}{d(cos\Theta)}$ vs. cosΘ. The observed values of the Λ polarization are strongly connected to the details of the production process. For example, in accordance with parity conservation in strong interactions, any non-vanishing polarization must be transverse to the production plane constructed from the beam and Λ momenta [14, 10], $\hat{n}_{prod} = \hat{k}_{beam} \otimes \hat{k}_{\Lambda}$. On the other hand, a neutrino scattering experiment[11] finds polarization along the direction opposite the W boson but no polarization perpendicular to the production plane. An analysis by Bigi [11], which postulates that Λ polarization originates from a polarized diquark, suggests that polarization would be especially apparent for Λ's in the target fragmentation region, $X_f < 0$. Experiment E632 had found that if they restrict Λ's to this region then the polarization in the direction opposite to the

W boson was modestly enhanced [11].

Meanwhile a π^-–Cu experiment [19] found evidence of Λ polarization in the $\hat{n}_{prod}$ direction only in the region $X_f > 0$, $P_T > 1.0$ GeV. They report the possibility of a $\bar{\Lambda}$ polarization in an intermediate P_T range (0.5–1.0 GeV). Interestingly enough, most experiments have reported no polarization for the $\bar{\Lambda}$.

Finally, experiment WA89 (using a Σ^- beam) reports no significant X_f dependence of the Λ polarization [10].

1.9.3 Quark–Gluon Plasma

A new state of hadronic matter, called quark–gluon plasma, has been hypothesized to form under conditions of extreme heating and/or compression. In the collisions of large nuclei at high energies, it is possible that conditions may be reached in which this new state of hadronic matter may form. Enhanced production of strange particles has been suggested as a possible indicator of QGP formation in relativistic nucleus–nucleus collisions [16, 17, 18].

1.9.4 $s - \bar{s}$ Correlations

Studies of correlations between Λ–Λ and Λ–$\bar{\Lambda}$ production give insight into baryon production. Events containing multiple strange particles can be used to determine what correlations exist between strange particles produced in the same event. Whether or not strange particles with opposite strangeness are more likely to

be in the same jet than in opposite jets is a question whose answer relates directly to the production process. There is considerable interest in how baryons in general are produced in the fragmentation process. The baryons most accessible for study are the proton and the Λ. Strange particles have the advantage that the combinatorics are much less and they are heavy enough that they are more likely to come from the initial hard scatter rather from the decay of some heavier particle.

1.9.5 Properties Of p+N $\rightarrow \gamma + K^0$ or Λ Events

The data presented here are among the first on the production of strange particles in high P_T π^0 or direct photon triggered events [21].

Perturbative Quantum Chromodynamics is useful only when α_s is small enough that the perturbation series converges. This happens during events in which the Q^2 exchanged between the two scattering partons is large (see equation 1.1.) In a hadron–hadron experiment, where we can not calculate the value of Q^2 directly, we rely on the transverse momentum, P_T, to identify a hard scatter event. A high P_T value indicates a hard collision has taken place.

Comparisons of strange particle fragmentation in π^0 and direct photon triggered events can give insight into strange particle production. As mentioned above, in π^--p interactions, we expect more high P_T direct photons from the annihilation subprocess than the Compton subprocess. This means that as the P_T of the direct photon (and awayside jet) increases so do the number of gluon initiated awayside

jets. We will search for differences in strange particle production between jets opposite high P_T π^0 or direct photon triggers. In addition, the question as to whether strange mesons or baryons separately show any differences in their production between the two types of jets will be investigated.

Chapter 2

The Meson West Spectrometer

Because cross sections at large P_T are small, direct photon experiments must have a spectrometer with large acceptance that has the capability to run at high intensities [6]. Good acceptance is also needed to identify and remove photons from π^0 and η meson decays. A highly segmented calorimeter is necessary in order to distinguish between single photons and two overlapping photons from the decay of a high energy π^0. The calorimeter must have a large energy range, needed to detect high energy photons as well as soft photons from an asymmetric decay of a π^0 or η meson. To resolve two photons from a high energy π^0 decay the spectrometer must be as long as possible. However, the farther away the detector is from the target, the larger it must be to cover the same solid angle. A high-resolution charged particle tracking system is necessary in order to identify and reject electrons as direct photon candidates. Charged particle detection is also necessary for study of the awayside

jet accompanying the direct photon.

The Meson West spectrometer was designed with all of these considerations in mind. It also included included the following elements:

- a cerenkov detector, for beam particle identification. This is important for making probabilistic statements, for example, about which subprocess (Compton or annihilation) was involved in the interaction (see figures 1.5 and 1.6.)
- A muon veto system for rejecting events triggered by a bremsstrahlung photon from a muon in the beam halo.
- A hadronic calorimeter for hadron identification.
- A forward calorimeter for total energy measurement of the beam and target jets.

2.1 The Spectrometer

The main goals of E706 were measurements of the direct photon cross section and the associated awayside jet. The accuracy of our measurements were limited by how well we understood the sources of background. For example, a π^0 decays into two photons with a 99% probability: These photons could emerge with a very small separation. If we are unable to separate and identify these two photons as

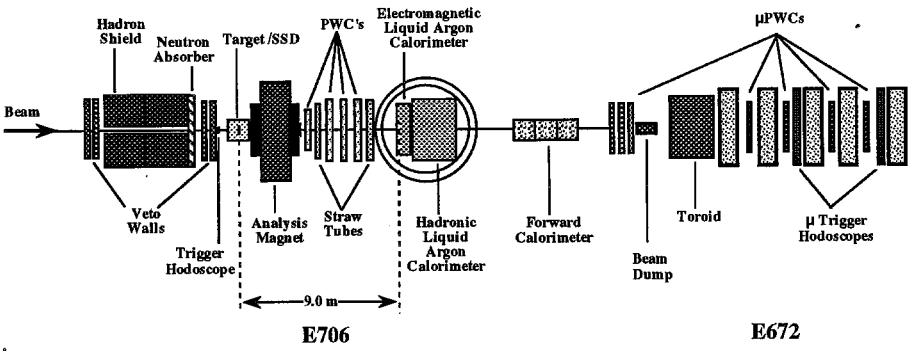

Figure 2.1: Layout of the Meson West spectrometer.

decay products of the π^0, then we are likely to treat the resulting shower as a direct photon candidate.

Our main tool for these measurements was the Electromagnetic Liquid Argon calorimeter (EMLAC.) The EMLAC was specially designed to measure high transverse momentum electro-magnetic showers. It was also designed with the ability to resolve two nearby photons from a π^0 or η decay.

Electrons, which shower in the EMLAC in a manner very similar to photons, were another source of background. To address this, we designed a tracking system capable of reconstructing the trajectories of charged particles so that they could be removed from the direct photon sample. The tracking system provided this protection in addition to many other benefits including the reconstruction of jets on the awayside and vertex location.

Neutral hadrons also presented a source of background. The hadron calorimeter (HALAC) was created for this purpose. Since hadronic showers tend to develop later than electro-magnetic ones, the HALAC was placed downstream of the EMLAC.

Because of the high beam rates, another source of background was due to muon bremsstrahlung. A muon in the beam halo could interact with some material in the spectrometer and emit a photon which would mimic a high P_T electromagnetic object in the EMLAC.

Veto Walls were installed along the beam direction to combat this type of

pollution in our direct photon sample.

A brief explanation of how each component operated will be given in the following sections.

2.2 The Meson West Beamline

Experiment E706 operated in the FNAL Meson West beamline. The MW beamline extended north, tangent to the main ring, to the MW9 experimental hall. The Tevatron provided a beam of 800 GeV protons which could be used in either of two modes: primary mode or secondary mode. In primary beam mode, approximately 1% of the Tevatron protons were directed down the primary beam line [28]. In secondary beam mode, in which 800 GeV protons were used to produce 515 GeV beams of primarily negative pions or protons, up to 30% of the total Tevatron beam was delivered to the production target [28]. E706 ran in both modes. The 1990 run used the negative secondary beam almost exclusively while the 1991 run used both the primary and the secondary beams.

The primary beam from the tevatron had a 19.1 nanosecond bucket structure [24], (meaning that the length of time between each proton was 19.1 ns.) Approximately 1-2x10^{13} protons were extracted during a 23 second spill[28] out of which approximately 5x10^{12} protons were directed down to the MWest primary target in negative secondary mode. The spills were separated by a 35 second period [24] which

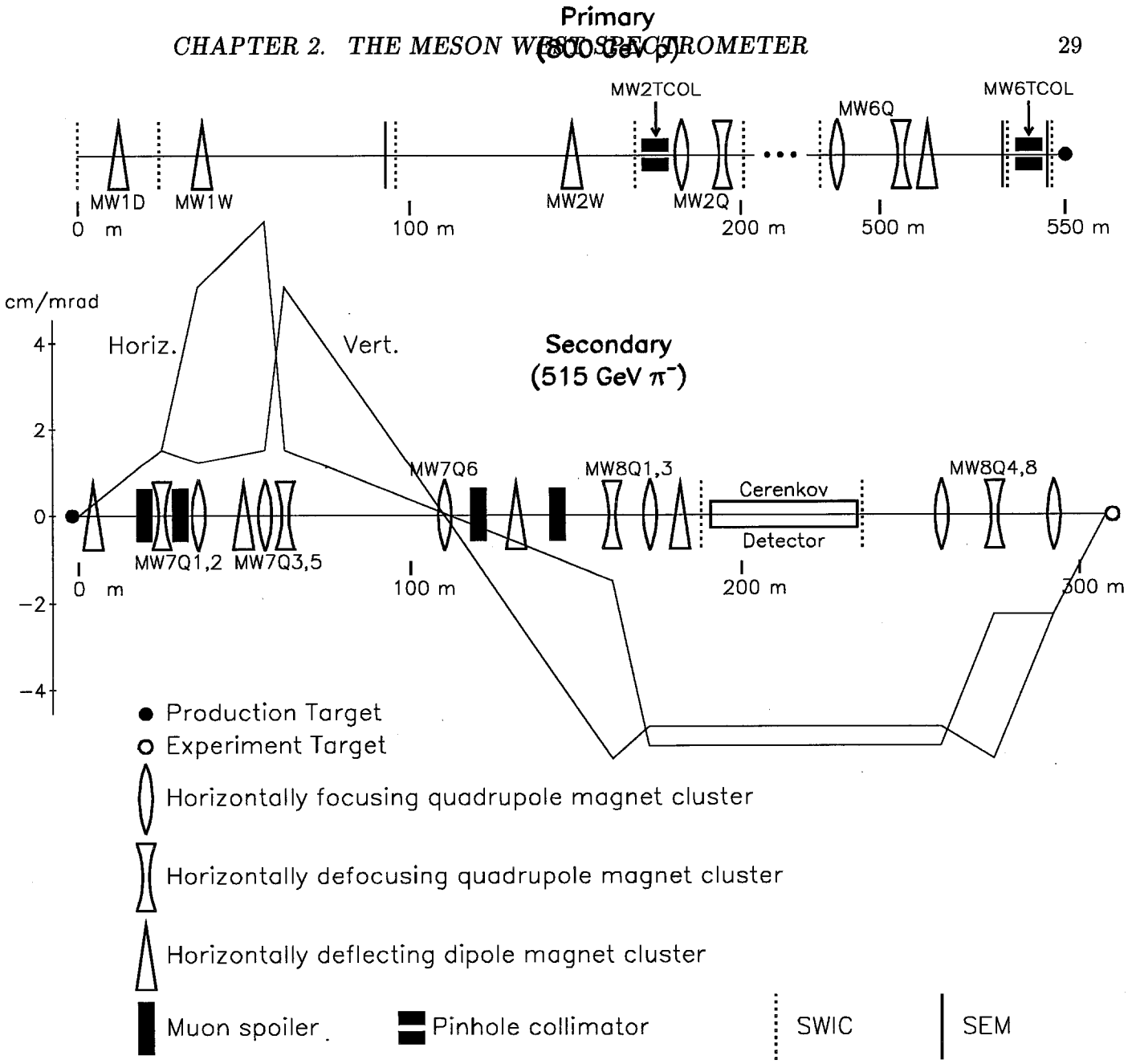

Figure 2.2: The Meson West Beamline

was used by the tevatron to accelerate the next batch of protons to the required energy.

In secondary mode, the proton beam interacted with a beryllium primary target producing many particles with various momenta. Using momentum selecting magnets, the secondary particles of interest were directed into the secondary beam. The magnets were tuned to select a reference secondary beam momentum of 530 GeV. This was a convenient momentum since comparisons were made with 800 GeV protons which had an average momentum per quark of 800/3 GeV = 267 GeV. Then the negative secondary beam, which was mostly pions, had an average momentum per quark of 530/2 = 265 GeV. The mean momentum of the secondary pion beam for the 1990 run turned out to be 515 GeV when a study was done [23]

The secondary beam intensity on the MW9 target was $\leq$ 2x10^8 per spill.

The positively charged secondary beam mainly consisted of protons but included about 1% positively charged K^+ and 3% π^+ [31]. The protons in the secondary beam were useful for comparisons with the 800 GeV proton results and the results from the negatively charged π^- beam used during most of the 1990 run.

The negatively charged secondary beam consisted mainly of π^- but also contained a non-negligible fraction of negatively charged K^- and anti-protons.

2.2.1 Cerenkov Detector

The beam was transported down the secondary beam line through a cerenkov detector which identified the particles in the beam. According to the laws of electrodynamics, as the velocity of a particle traversing a medium exceeds the speed

of light in that medium a cone of coherent radiation is emitted at an angle which depends on the velocity of the particle and the index of refraction of the medium.

$$cos(\theta) = \frac{1}{n\beta} \tag{2.1}$$

By filling the cerenkov detector with helium gas and adjusting the pressure, the index of refraction of the medium was adjusted. The momentum of the beam was fixed upstream by the selection magnets. Lenses used to focus the cerenkov light into photo multiplier tubes were placed at fixed angles in the detector. By varying the pressure of the gas, to select a particular index of refraction, and with the beam momentum measured upstream, the mass of the particle traversing the cerenkov detector was deduced. The angles of the cerenkov radiation were typically very small so that in order to resolve radiation at different angles it was necessary to use a very long detector in order to get enough separation. The cerenkov detector was located 98 meters upstream of the target and was 42 meters long. A mirror was placed on the downstream end of the detector to reflect the light back to the upstream end where the various lenses were located. This effectively doubled the length of the detector. At the upstream end three concentric rings consisting of six phototubes each were placed to collect the radiated photons. The geometry and spacing of the rings was such that at the optimum pressure, all three of the major components of the beam could be resolved at once. Helium gas, kept at a pressure between 4-8 psia, was used as the medium.

2.2.2 Hadron Shield

The hadron shield sat at the end of the beamline, just inside the MW9 experimental hall. It was 4.3 m wide, 4.7 m long and 3.7 m high [24]. The function of this pile of steel was to absorb hadrons from the beam halo so that they would not impinge upon the spectrometer. This was important since any interactions in addition to that of the beam particle with the target could confuse our event reconstruction. The beam halo was created far upstream during the interaction of the proton beam from the tevatron with the primary target. The beam halo traveled parallel with the beam but was displaced transversely. The beam particles passed through a tunnel in the hadrom shield.

Just downstream of the hadron shield there was a tank of distilled water used to absorb neutrons which might make it this far downstream.

2.2.3 Muon Identification

The first line of defense against muons in the beam halo were the spoiler magnets positioned upstream near the primary target. The purpose of these magnets was to redirect particles in the beam halo out of the beamline. Muons in the beam halo which made it past the spoiler magnets were not stopped by the hadron shield so it was necessary to identify them as they passed through the spectrometer. To this end three veto walls made of scintillators were placed, one just before the hadron

shield and two after. This would enable us to distinguish the bremsstrahlung photon of a muon from a high P_T photon characteristic of a direct photon event. It was possible for an event to veto itself if a particle passed through the downstream veto wall after back scattering off of the calorimeter. We decrease the probability of this self vetoing by requiring a hit in the upstream veto wall in coincidence with a downstream veto wall hit.

2.2.4 Beam Particle and Interaction Identification

The beam hodoscope was downstream of the veto walls. The hodoscope consisted of three scintillators in three different views: horizontal(X), vertical(Y), and rotated(U). A signal from the beam hodoscope was the first indication that a beam particle was approaching the target region.

Finally. there were four scintillator counters placed around the beamline to detect interactions in our target region.

2.3 Calorimetry

The Meson West spectrometer contained three separate calorimeters. Each calorimeter was designed with a specific purpose in mind.

The electromagnetic calorimeter was used to measure the energy deposition

of electrons and photons. Due to their small masses, electrons and photons with energies above 100 MeV tend to lose energy through the mechanisms of bremsstrahlung and pair production, respectively. It was this fact among others which motivated the division of the EMLAC into a front and a back section. The front section provided 10 radiation lengths of material while the back section provided an additional 20 radiation lengths. Electrons and photons with energies less than 100 GeV, deposited most of their energy in the front section of the EMLAC. A typical electron had energy of a few GeV. This division also helped us resolve two closely spaced photons, since the showers in the front section would have a narrower profile than those in the back section [24].

We also defined an offline muon bremsstrahlung cut using position information from the front and back sections separately.

The hadronic calorimeter (HALAC) was placed immediately downstream of the electromagnetic calorimeter in the cryostat (See figure 2.3.) The physical processes that cause the propagation of a hadronic shower are not the same as for electro-magnetic showers. About half of the incident hadron energy is passed on to secondary particles in collisions [33]. Hadronic showers tend to be more spread out and take longer to develop than electromagnetic showers. Therefore the hadron calorimeter had to be thicker than the electro magnetic calorimeter. The HALAC was 8 interaction lengths deep plus the 2 interaction lengths represented by the EMLAC.

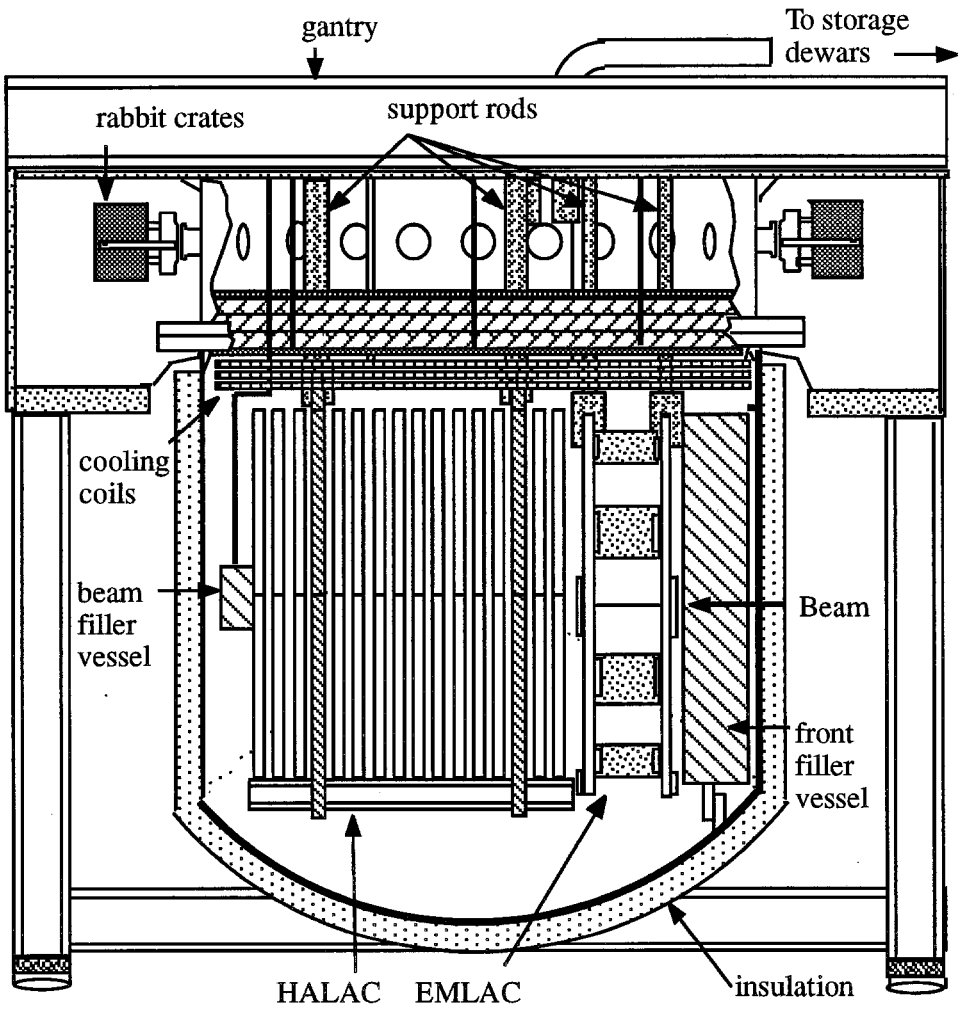

Figure 2.3: A view of the gantry

Finally, the forward calorimeter was placed downstream of the hadron calorimeter outside of the cryostat. The forward calorimeter was designed to measure the total energy of the beam and target jets.

2.3.1 The Electro-Magnetic Liquid Argon Calorimeter

When a π^0 decays symmetrically, the separation angle of the two photons are proportional to M_{π^0}/E_{π^0}. It was necessary, in order to separate the showers of two closely spaced photons, to have a very fine segmentation for the EMLAC. The position resolution of the EMLAC is a function of energy:

$$\sigma_{x,y} = 0.024 + \frac{1.53}{E}(cm) \tag{2.2}$$

where E is in GeV [30]. A π^0 can also decay asymmetrically. Since the π^0 is a spin zero meson, there is no preferred angle for a decay photon in the π^0 rest frame. The two–photon asymmetry is defined as $A = \beta * Cos(\theta)$ where θ is the angle of a photon in the π^0 rest frame. This means that in the lab frame the asymmetry distribution, defined in terms of photon energies as $A = (E_1 - E_2)/(E_1 + E_2)$, is flat. Therefore the EMLAC must be able to resolve both high and low energy photons or we risk having our direct photon sample contaminated. The intrinsic energy resolution of the EMLAC was $14\%/\sqrt{E}$ for photons and $21\%/\sqrt{E}$ for electrons[30].

The transverse segmentation of the EMLAC was designed so that a trigger

based on the deposition of electro-magnetic P_T was easily formed. The EMLAC used an alternating $r - \phi$ geometry. The first plane consisted of concentric circles of increasing radius (for measuring the radial distance of the shower) while the next plane consisted of radial strips (for measuring the azimuthal angle). There were 256 R-strips. The R-strips were focused on the target so that the strip width increased with depth into the calorimeter. The depth dependence of the strip width is given by the following equation:

$$w(cm) = \frac{0.5466}{900}(900 + 1.56(i-1)) \tag{2.3}$$

where i represents the i^{th} r-board, 1.56 cm is the distance between two consecutive R boards and 0.5466 cm is the strip width of the first R-board [25]. The widths of the R-strips on successive R boards were adjusted such that a particle which originated in the target would pass through the same sequential r-strip in each successive cell.

The ϕ boards were composed of inner and outer sections. The number of ϕ strips were doubled at a distance of r=40.2 cm. The outer section had twice as many ϕ strips as the inner section. This improved the position and energy resolution in the EMLAC. The inner section consisted of 96 strips, each covering an azimuthal angle of $\pi/192$ while the outer section consisted of 192 strips each subtending an angle of $\pi/384$.

The r-ϕ geometry was a convenient choice of coordinate system since we were interested in high P_T events. For trigger purposes, P_T was defined as $E_R sin\theta$ where

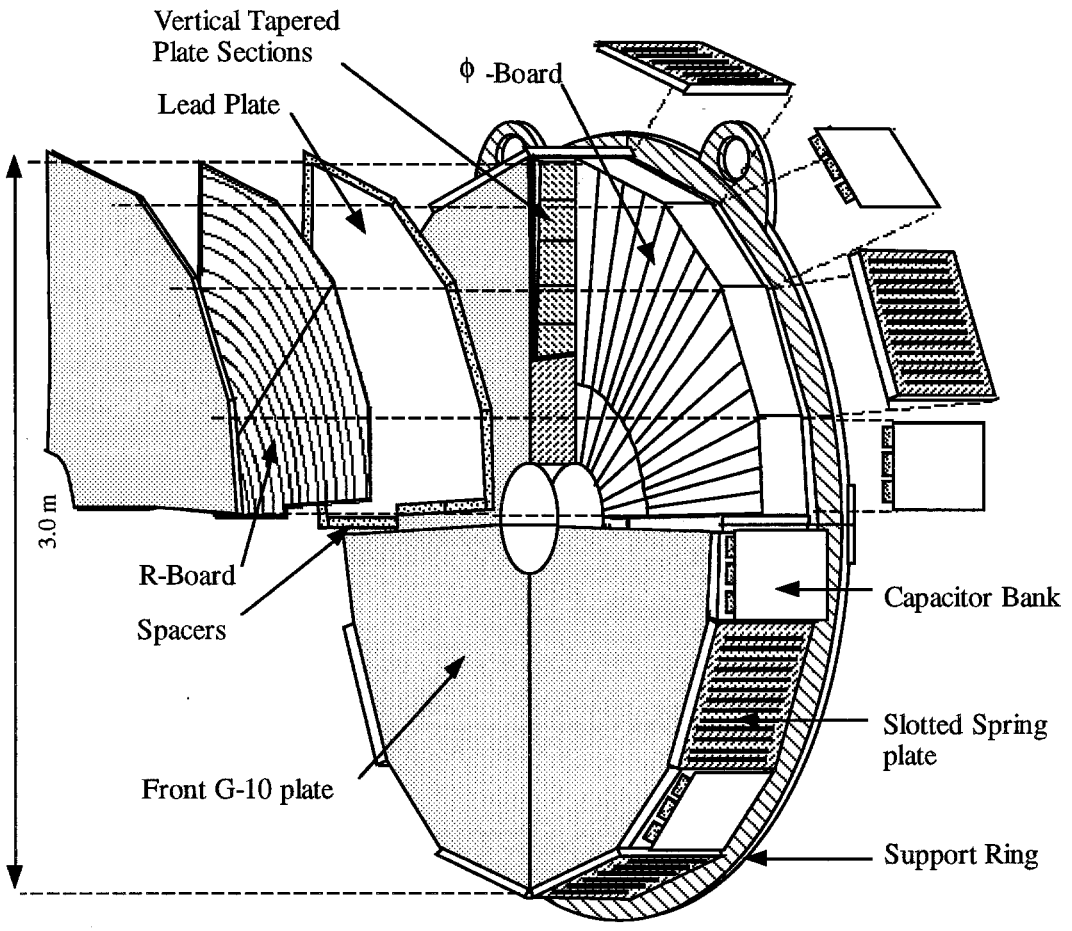

Figure 2.4: Exploded view of the EMLAC

θ is the angle subtended from the target to the r position of the energy deposition (See Trigger description 3).

The EMLAC was divided into front and back sections. There were 22 layers in the front section and 44 layers in the back section of the EMLAC.

Each layer consisted of a 0.2 cm lead absorber sheet followed by 0.25 cm of liquid argon, followed by a G-10 copper clad anode (either of r or ϕ orientation), followed by another 0.25 cm argon gap. The lead sheets also functioned as high voltage cathodes, while the showers ionized the liquid argon and the electrons were collected on the copper anode strips [24].

2.3.2 The Hadronic Liquid Argon Calorimeter

As mentioned earlier, one of the reasons for splitting the EMLAC into front and back sections was to distinguish between electromagnetic showers and the showers due to hadrons. The HALAC was constructed to further identify charged and neutral hadrons.

The HALAC was constructed of 53 layers with each layer consisting of a 1 inch thick steel absorber plate followed by a 1/8 inch thick liquid Argon gap, and a sampling module called a cookie. Like the EMLAC the, HALAC was longitudinally segmented into a front and a back section. The front section had 14 layers while the back section had 39 layers [29].

Since hadronic showers were typically broader than electromagnetic ones, a

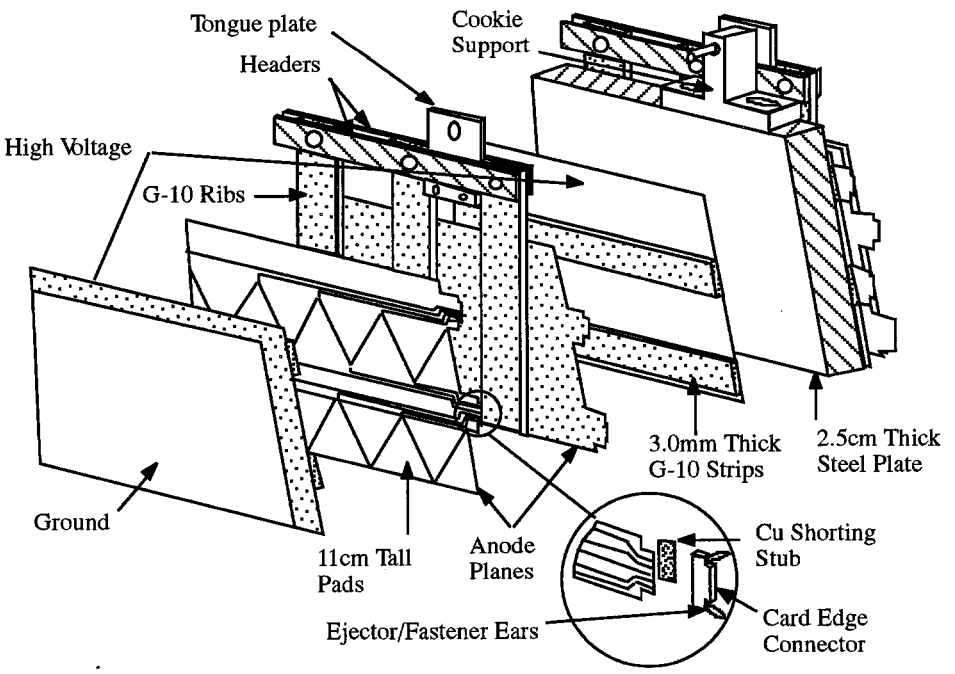

Figure 2.5: Structure of a HALAC cell

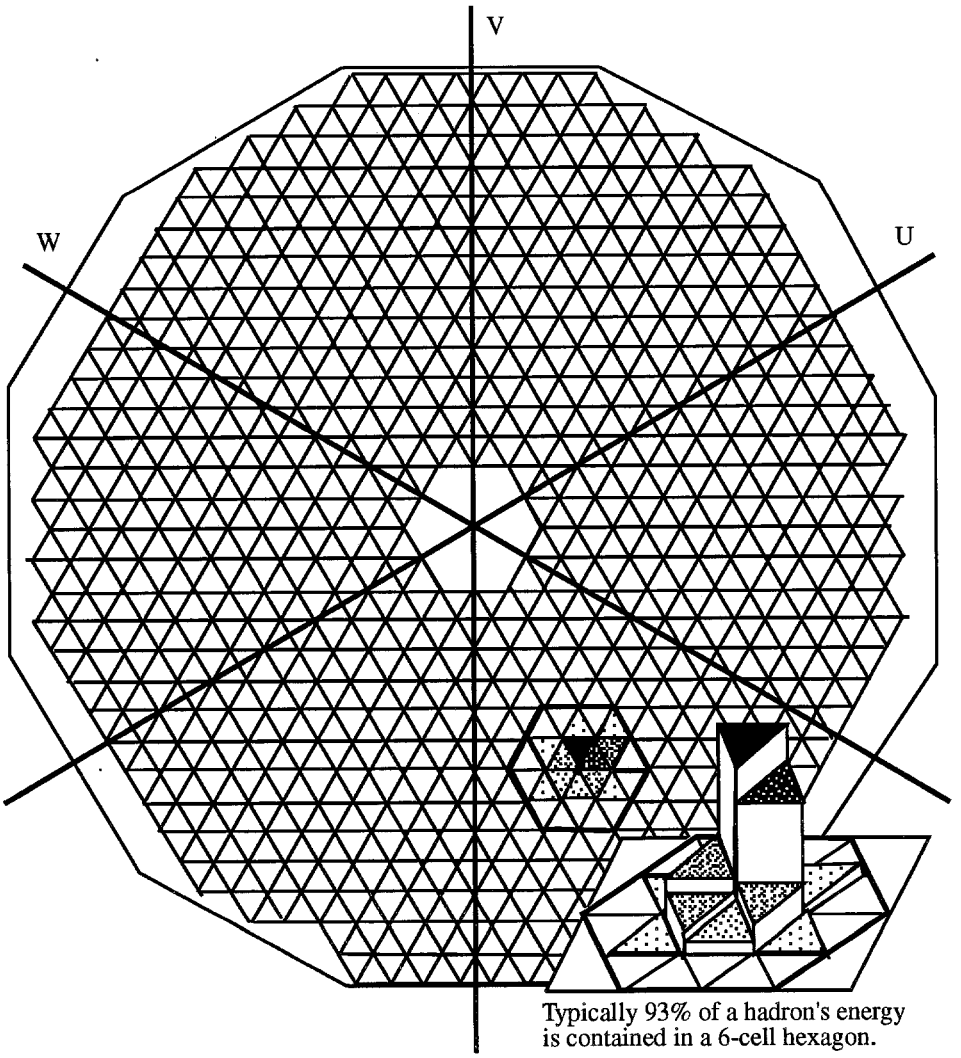

Figure 2.6: Geometry of the HALAC readout pads

coarse pad geometry was chosen for the readout of the HALAC. The HALAC had a focused geometry like the EMLAC. The pads grew larger as one moved downstream of the target. The height of the pads ranged from 10 to 14 cm [29]. The geometry of the HALAC readout pads is shown in figure 2.6

Figure 2.5 shows an exploded view of a single cookie. In the center of the cookie, two copper clad anode planes are placed back to back. The copper was scribed into rows of electrically isolated triangles with every other triangle inverted to its neighbor. The copper anode planes faced the high voltage planes.

2.3.3 The Forward Calorimeter

The forward calorimeter was located approximately 15 m downstream of the target. The FCAL measured the energy and P_T of the forward beam jet. It was 114 cm in diameter and its geometrical acceptance covered the region of the beam hole in the center of the EMLAC and HALAC except for a 1.5 cm hole in the center of the FCAL that provided passage for noninteracting beam particles. The FCAL was a sampling calorimeter with 1.9 cm thick steel absorber plates and 0.46 cm acrylic scintillator plates as a sampling medium [29]. (see figure 2.7).

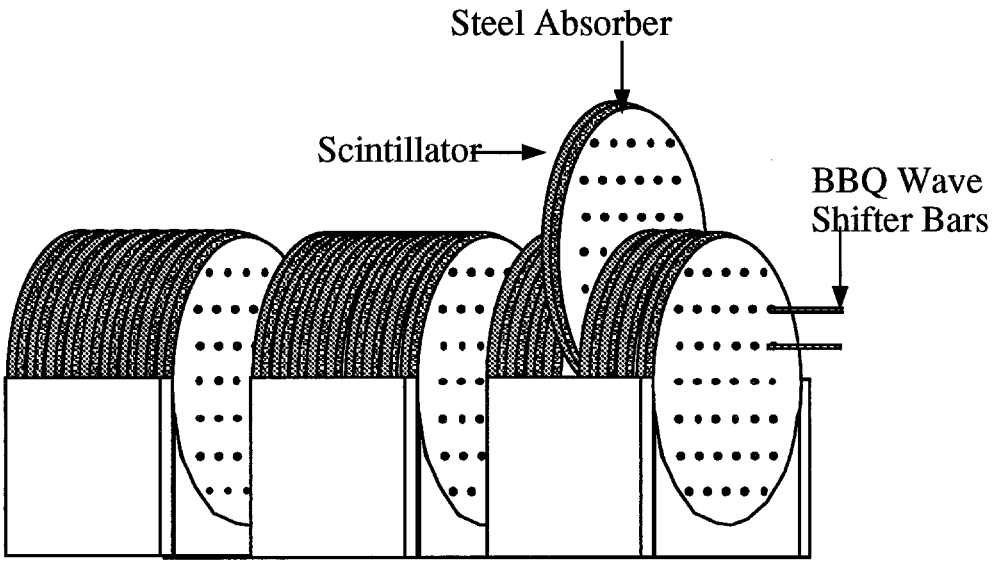

Figure 2.7: The Forward Calorimeter

2.4 The E706 Tracking System

Although the main goal of E706 was the measurement of the direct photon cross section, a good tracking system was useful in order to identify electrons which could mimic the response of a photon in the calorimeter and to essential reconstruct the primary vertex as well as the awayside jet. The E706 tracking system consisted of several sections (see figure 2.1). The beam tracking system consisted of six beam silicon strip detectors (ssds) which were placed upstream of the target. Following the target were 10 vertex ssds: 5 x-view and 5 y-view. Next we had the analysis magnet which was used to help determine the particle momentum in the x-z plane. The first straw tube drift chamber was downstream of the analysis magnet and contained four x-view followed by four y-view planes. Following the straw tubes were four pwc modules. In each module there were x,y,u,v-view planes that enabled us to reconstruct 3-dimensional space tracks. Finally following the last pwc module was the second straw tube drift chamber. Straw tube drift chamber 2 contained four x planes followed by four y planes. Each component of the tracking system will be discussed in turn, going from upstream to downstream.

2.4.1 The Silicon Strip Detectors

The Beam Chambers

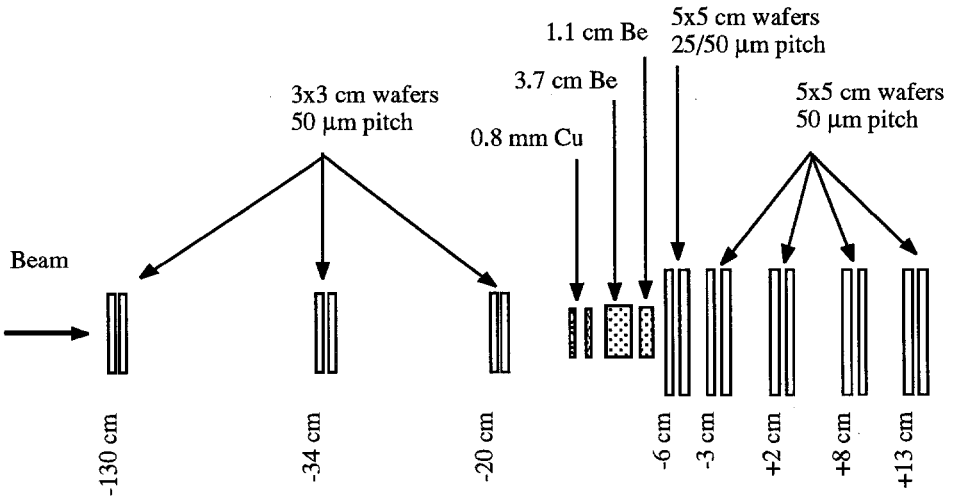

Figure 2.8: The 1990 Target region

To precisely measure the direction of the incoming beam, it was necessary to supplement the information available from the beam hodoscopes with a device of much finer resolution. To this end three modules of silicon strip detectors were placed downstream of the beam hodoscope (see figure 2.8). Each module contained two ssd planes. The first plane had the individual strips placed horizontally. This plane was used to measure the horizontal displacement of a given particle from the beam (z) axis. The next plane had the individual strips placed vertically. This plane was used to measure the vertical displacement of a give particle. The beam planes were 3cm x 3cm x 300 microns thick. They had a 50 micron pitch i.e. 50 microns from strip center to strip center. These planes gave us a theoretical resolution of 50 microns/$\sqrt{12}$ per strip.

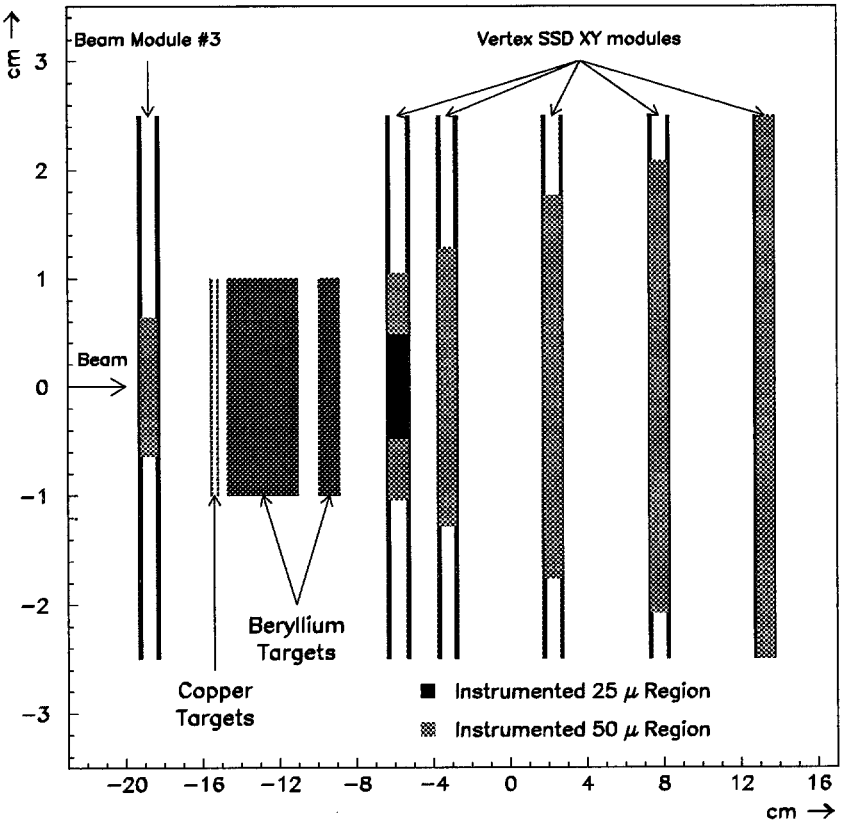

Figure 2.9: The Silicon strip detectors and 1990 target

The Vertex SSDS

The vertex silicon strip detectors were used to measure the primary vertex position with high precision. These were five modules located just after the target and before the analysis magnet (see figure 2.9.) Like the beam SSDs, each module contained both an x-view and a y-view plane. In order to increase our resolution in the forward rapidity region, the first two planes were hybrids of 25 and 50 micron

spacings (pitch) between successive silicon strips. These planes had strips spaced 25 microns apart in the central region of the planes and 50 microns in the outer regions. In the forward region the tracks are very dense and it was likely that two adjacent tracks had a separation of less than 50 microns. The rest of the planes had a 50 micron pitch throughout the entire plane. The vertex resolution was 10 microns in the transverse (x-y) plane and about 350 microns in the longitudinal (z) direction [32].

A charged particle passing through a silicon strip detector will knock off electrons from the silicon atoms creating an electron-hole pair. The e-h pairs then drift in opposite directions when an electric field was applied. The charge was collected at the electrodes to give a signal proportional to the deposited energy. A minimum ionizing particle passing through the SSD would produce about 25,000 electron-hole pairs [27]. The collection time for the total charge depended on the electric field strength and the mobility of the charge carriers and the thickness of the SSD. The collection time at E706 is about 25 nano–seconds [27].

2.4.2 The Proportional Wire Chambers

The proportional wire chambers (PWC) were located downstream of the dipole analysis magnet. The purpose of the PWCs was to track the particles as they exited the aperture of the dipole magnet. The PWC system was the only system which could do independent space tracking. Each module contained four

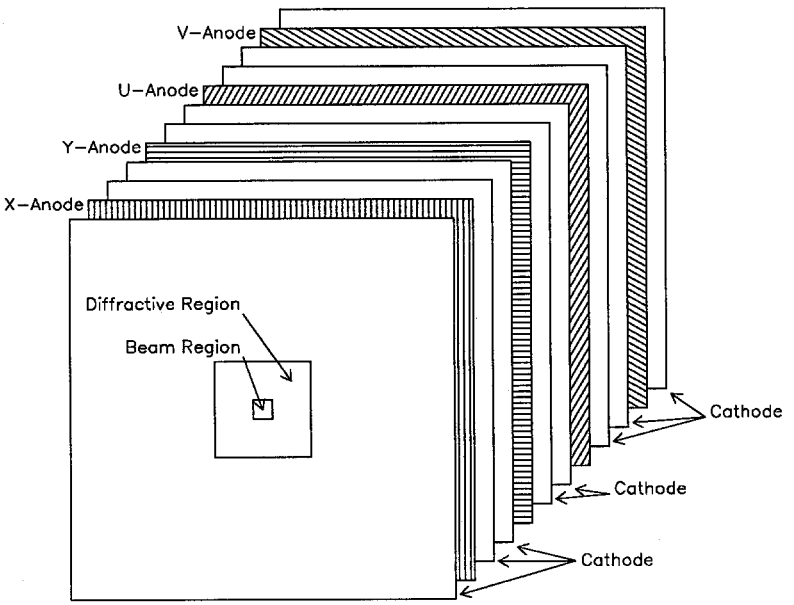

Figure 2.10: The proportional wire chambers

planes: The first two planes, the x plane and the y plane were orthogonal to each other. The next two planes were also orthogonal to each other but rotated with respect to the coordinate system defined by the x and y planes. The relationship was given by the following expressions [26]:

$$\begin{aligned} u &= \frac{4}{5}x + \frac{3}{5}y \\ v &= \frac{-3}{5}x + \frac{4}{5}y \end{aligned} \tag{2.4}$$

The x view and y view were approximately 90 degrees apart while the u view and v view was at 37 and -53 degrees respectively with respect to the vertical dimension (see figure 2.10). This second rotated coordinate system gave us enough constraints to match x hits with y hits and thus form space tracks. The SSD's and the STD's used the space tracking information of the PWC's to match there own x and y views. E706 used four separate PWC modules for a total of four planes in each view. Each module contained 4 anode planes each in one of the four views for a total of 16 planes. The PWC's used a wire spacing of 0.1 inches. Each anode plane was sandwiched between two cathode planes for a total of twelve planes per module. The cathodes were held at a voltage of -2900 V while the anode planes were grounded [26]. When a charged particle passed through the plane it ionized the electrons in the gas. The resulting electrons drifted toward the wire. As the electrons got close to the wire they acquired enough kinetic energy to further ionize the gas until an avalanche of electrons occurred.

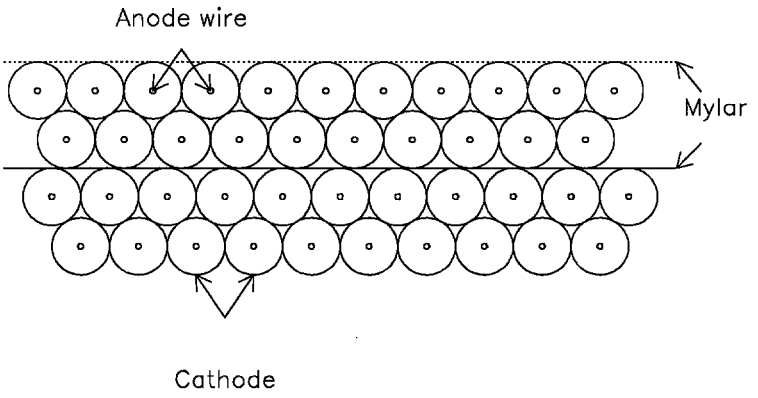

Figure 2.11: The close-packed formation of the straw tube drift chambers

2.4.3 The Straw Tube Drift Chambers

The E706 tracking system employed high resolution straw tube drift chambers (STD). The enhancement in resolution provided by the straw chambers allowed us to greatly improve the linking of downstream space tracks (PWC) with upstream SSD tracks. Because of the higher resolution of the STD's we were able to cut the

size of our linking window thus reducing the number of multiple links and therefore giving us more confidence in our linked track and therefore better momentum resolution.

There were two straw tube drift chamber modules: The first one, henceforth called "straw one", was located approximately 450 cm downstream of the target. It was placed between the first and second PWC module. It contained four x-planes (tubes running vertically) followed by four y-planes (tubes running horizontally). The diameter of the tubes in straw one was 1.034 cm. Every two planes were placed in a close-packed formation meaning that the tubes from one plane fit into the gaps of the tubes of the second plane and vice versa (see figure 2.11). The next two planes were a repeat of the first two, except that the planes were staggered by half a wire space. This gave us better coverage and eliminated uninstrumented regions for a particle to slip through undetected. Straw one was made up of 160 vertical tubes per plane in the x view and 128 horizontal tubes in the y-view.

The second straw tube drift chamber (henceforth called "straw two") was located downstream of the fourth PWC module and was attached to the LAC gantry. This chamber also contained four x planes and four y planes with every two planes in the close packed formation as described above. The tube diameter of the straw tubes in straw two was 1.626 cm. Straw 2 had 168 tubes per plane in both of the views.

The straw tubes were made of mylar coated with aluminum on the inside.

A gold-platted tungsten wire was threaded down the middle of the straw tubes. A high voltage of about 1.7-1.8 kilovolts was placed on the wire. The tube was filled with a standard gas mixture of argon and ethane. The charged particle would pass through the tube and ionize the gas. The free electrons would migrate toward the wire while the positive ions would migrate to the inner walls of the tube. This would create a voltage drop across the tube which would be read out through the electronics. Information about which wire was hit as well as timing information from the charge collection was used to find the hit position with a resolution of approximately 250 microns per tube. The centers of the central four tubes of each plane were deadened so that the electronics were not swamped by the interactions due to the beam particle.

2.4.4 The Analysis Magnet

In order to measure the momentum of the charged particles created in the interaction it was necessary to use a large dipole magnet. The magnetic field created by this magnet approximated a square field. When a charged particle passed through the magnet field its path would be curved in the x-z plane. Using standard methods the momentum of the particle could then be determined. The center of the magnet was located at approximately 198 cm downstream of the target. The magnetic field imparted a 450 MeV transverse momentum impulse to any charged particles [26].

Chapter 3

The E706 Trigger and Data Acquisition

3.1 The E706 Data Acquisition System

The data acquisition system was an important aspect of E706. We had many components to our spectrometer and the information from each one had to be read out and concatenated into a single event. A block diagram of the DA is shown in figure 3.1.

The central unit was a DEC μVax which ran VAXONLINE, Fermilab's data acquisition software. The readout of the various pieces of the spectrometer were accomplished by four separate subsystems. These subsystems are listed in table 3.1. The LAC and straw tube drift chambers were read out by the FASTBUS system

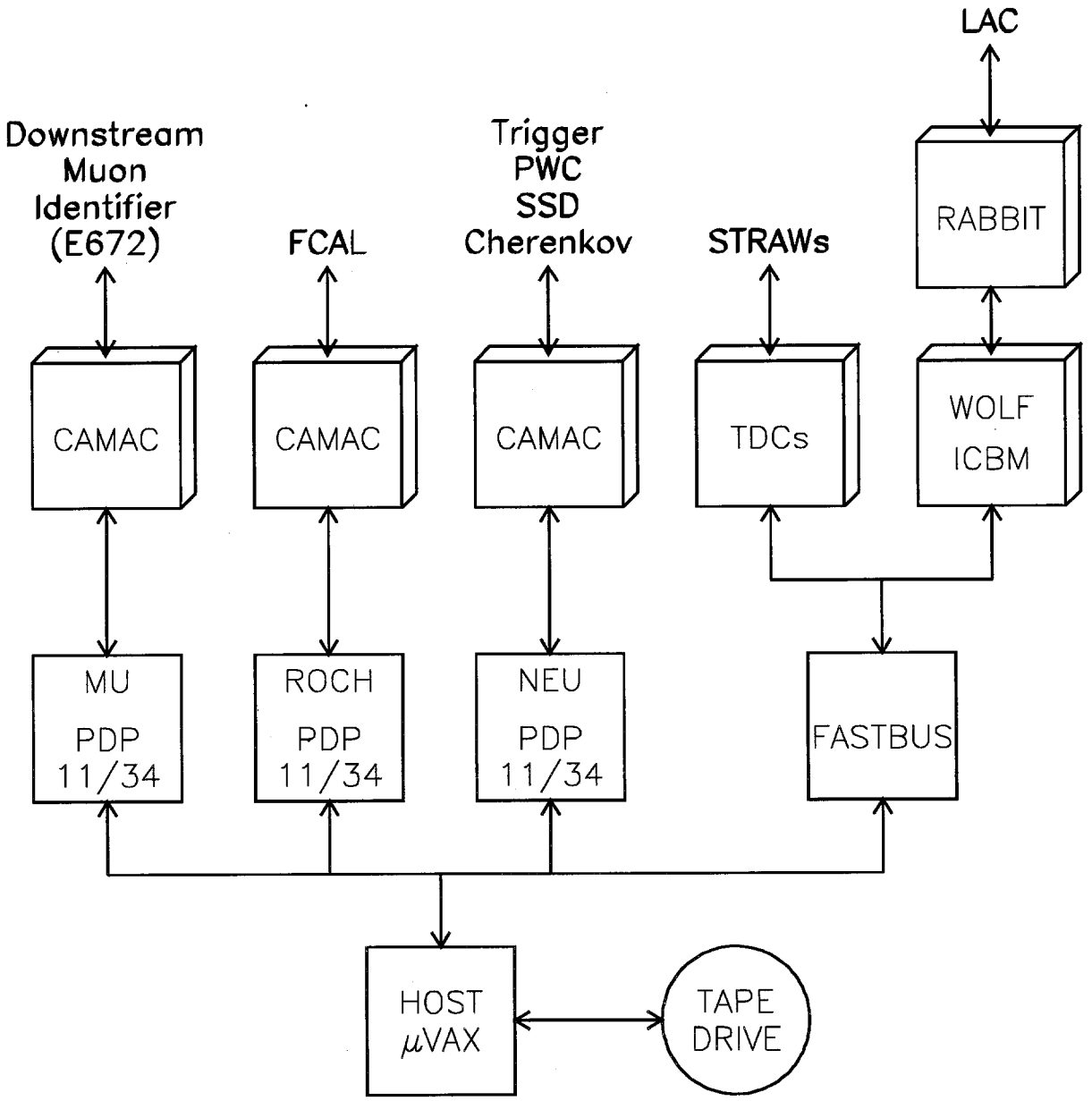

Figure 3.1: Block diagram of the E706 data acquisition system

System	Device to be read out
FASTBUS	LAC AND STD
PDP NEU	SSD's,PWC's,TRIGGER
PDP ROCH	FCAL
PDP MU	E672 Muon Chambers

Table 3.1: Subsystems and their responsibilities

Component	Purpose
Event Builder	Concatenated individual pieces into one record
Output	Wrote the events to 8 mm cassette tape
Run control	managed processes and initiated begin run tasks
Global menu	User interface for all VAXONLINE processes

Table 3.2: VAXONLINE SUBSYSTEMS

while the SSD's, PWC's, trigger, FCAL were read out by the various PDP-11's [24].

Data read out by the slave components were concatenated into a single event by the μVax and written to 8 mm magnetic tape. All these processes were supervised by VAXONLINE. The four major components of VAXONLINE are shown in table 3.2 [28]

Triggered events were written to tape in sets called runs. Approximately 65000 events was the maximum that one run could contain. Two tape drives were used during running.

3.2 The E706 Trigger

One of the primary physics goals of experiment E706 was a measurement of the direct photon cross section. Since the major source of background to this measurement was photons from misreconstructed π^0's, it was necessary to measure the π^0 cross section to high precision. Furthermore, we wanted a sample of direct photons over as large a P_T range as possible. Photons with a large P_T are desirable since the gamma to π^0 ratio increases at large P_T. However, the number distribution of direct photons and π^0's are steeply falling functions of P_T (P_T^{-6}) [6]. Therefore, the set of events containing high P_T π^0's and photons was a very small fraction of the total number of interactions in the target. In order to preferentially select events of interest to us it was necessary to design a trigger system with the following properties:

- The trigger had to select high P_T events.
- The trigger had to decide quickly whether to save an event.
- The trigger had to be smart enough to reject "faked" high P_T events.
- Sufficient trigger information had to be recorded so that correlations could be checked offline and trigger efficiencies and biases could be studied.

The trigger was designed with all of the above criteria in mind. It made decisions at several stages as to whether an event should be written out or not.

The criteria were simple in the early stages. The later stages of the trigger became progressivly more selective. In this way we could reject an event early if it was not likely to be of interest for our physics goals. In the following paragraphs the various decision stages of the trigger are described. The event in question could be rejected anywhere in the decision making process.

3.2.1 Identifying Beam Particles

The first step in deciding whether an event was to be selected was to decide whether there was the *potential* for an interaction with the target. To accomplish this we needed to know when we had a beam particle passing through the target region.

Upstream of the experimental target, there were three planes of scintillation counters set up in X,Y, and U views. The X and Y views were orthogonal to each other while the U view was rotated by $\pi/4$ radians with respect to the Y axis. Each plane consisted of 12 elements that were 2mm thick and 35 mm long. The eight central elements were 1mm wide so that each element would receive only a small fraction of the beam. On the outside of the central elements there were 2mm wide elements followed by 5mm wide elements on the outside. We required that at least two of the planes registered a hit to satisfy the beam definition. [34].

In order to avoid triggering on beam particles which missed the target and/or passed outside the acceptance of the Silicon Strip Detectors (SSD), we installed a

beam hole counter. The beam hole counter was 4 by 4 by 1/8 inches thick. It was made of a plastic scintillator with a 3/8 inch hole in the center through which the valid beam particle(s) could pass. By rejecting events which registered a signal in this counter, we eliminated events generated by incident beam which did not pass through the target.

3.2.2 Identifying Interactions

Approximately 15% of the beam particles that pass through the target interact[34]. Therefore the next step in the triggering process was to identify interactions. To do this four scintillations counters were installed. Two of the scintillation counters were placed between the SSD/target box and the MW9AN analysis magnet (See figure 3.2.) Each of these counters was 6 by 3 by 1/16 inches thick with a semicircular hole of diameter 3/4 inches. The other pair of counters was installed on the downstream end of the analysis magnet. These counters were 8 by 4 by 1/16 inches thick with a semicircular hole of diameter 1 1/2 inches. The counters were designed to intercept most of the charge particles from an interaction while minimizing interactions due to particles in the beam halo. The interaction definition required a valid beam definition in coincidence with 2 or more interaction counters firing [34].

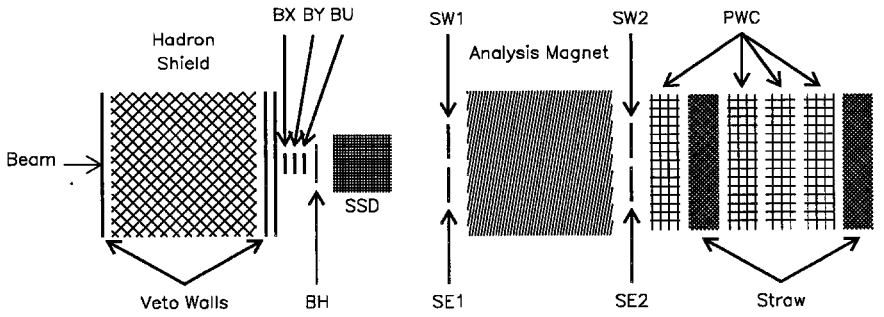

Figure 3.2: Configuration of beam and interaction counters used by the trigger

3.2.3 Identifying High P_T Depositions

Once it was decided that we had an interaction in the target, we had to decide whether the event contained the high P_T scattering signature that we were interested in. To do this we had to sample the energy deposition in the electro-magnetic liquid argon calorimeter (EMLAC) and give it the proper weight.

Signals from the EMLAC were fed into a custom designed RABBIT amplifier (LACAMP) cards. These cards produced a fast estimate of the energy deposited into a given strip in the EMLAC. The energy measurements from the LACAMPS for the R-view strips were then fed into RABBIT P_T Attenuator cards that attenuated each strip energy by approximately 2*Sin(θ) (see figure 3.3) where θ is the angle between the beam line axis and the I_{th} strip subtended from the target. With this information the various trigger definitions could be constructed [34].

3.2.4 The Pretrigger

During the time the trigger was busy, it was unable to respond to subsequent events. Therefore it was necessary to make quick decisions. The pretrigger was designed to reject the bulk of the very low P_T events which were not interesting. The pretrigger rejected about 99% of events [34]. The pretrigger also rejected an event if a muon was identified or if we had energy in the EMLAC from a previous event.

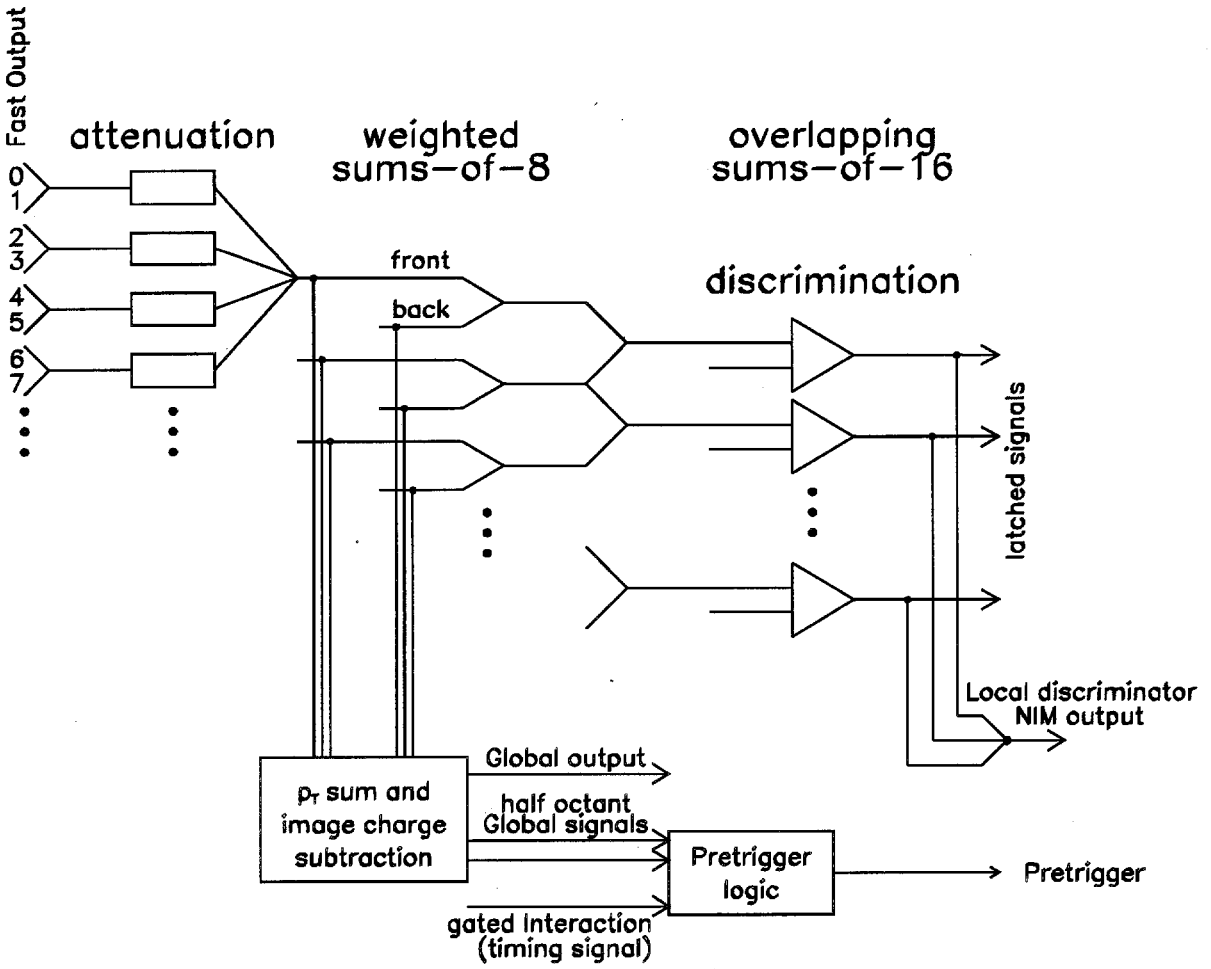

Figure 3.3: Local trigger signal formation

The Pretrigger Timing

One of the tasks of the pretrigger was to decide quickly whether to temporarily store the information from the LAC and the tracking system while a final trigger decision was being made. The zero crossing discriminators were used in this decision. They provided a stable timing requirement which enabled us to make fast calculations on the amount of P_T in the event. The pretrigger cut was about 2 GeV. The pretrigger requirement depended on the $\sum P_T$ in an octant.

Identifying Muons

Along with the particles of interest that were transported down the beam line, there were many particles from the debris of the primary interaction that traveled parallel to but outside of the beamline. This beam halo could have caused a large number of false triggers because the halo particles would hit the LAC at large radii and mimic a high P_T particle. Several precautions were taken to avoid this kind background (see chapter 2.)

Veto walls which were used to tag muons in the beam halo were placed downstream and upstream of the hadron shield. These were scintillation counters placed in such a way as to cover an area around the beamline. A hole in the center of the array allowed the beam to pass through.

The Early P_T System

An early P_T system was included to prevent us from triggering on pile-up events in the EMLAC. If an interaction produced a signal in the EMLAC it could take as long as several micro seconds for that signal to drop to a negligible level. If another deposition of energy was deposited in the same octant it would be added to whatever is left from the previous deposition. This could produce a fake high energy/P_T shower.

To prevent this kind of shower from firing the trigger, the global P_T signals were discriminated, delayed, and used as vetos on the pretriger high signals.

3.2.5 Trigger Level

The types of triggers and their respective thresholds were chosen to provide useful numbers of events across the accessible P_T range. They were also useful as cross checks on different kinds of triggers. Because of the steeply falling cross section vs P_T curve it was necessary to prescale events of lower P_T in order not to be swamped by them. By combining different selection topologies and multiple thresholds we were able to cover a large fraction of the physics signals that can be measured by the EMLAC.

The Local Triggers

The local triggers used the local discriminators to provide their primary threshold requirements. These were designed specifically to look at direct photons. They also provided good coverage for π^0 events. This is because high P_T π^0s as well as direct photons distribute their energy over a small region in the *LAC*. Most of their signals were confined within the 8 cm (16 strips) covered by a given local trigger (see figure 3.4).

The Global Triggers

The Global triggers were designed to trigger on π^0, η, and ω particles without having the inherent limitations of the local triggers. The global triggers were concerned with the integrated P_T over an octant. There was also a minimum P_T shower requirement to avoid pure noise events.

The Two Gamma Trigger

The two gamma trigger required a P_T deposition in an octant plus another in the octant diametrically opposed or adjacent to a diametrically opposed octant. The purpose of the two gamma trigger was to investigate double direct photon events and perhaps trigger on $J/\psi \rightarrow e^+e^-$ decays.

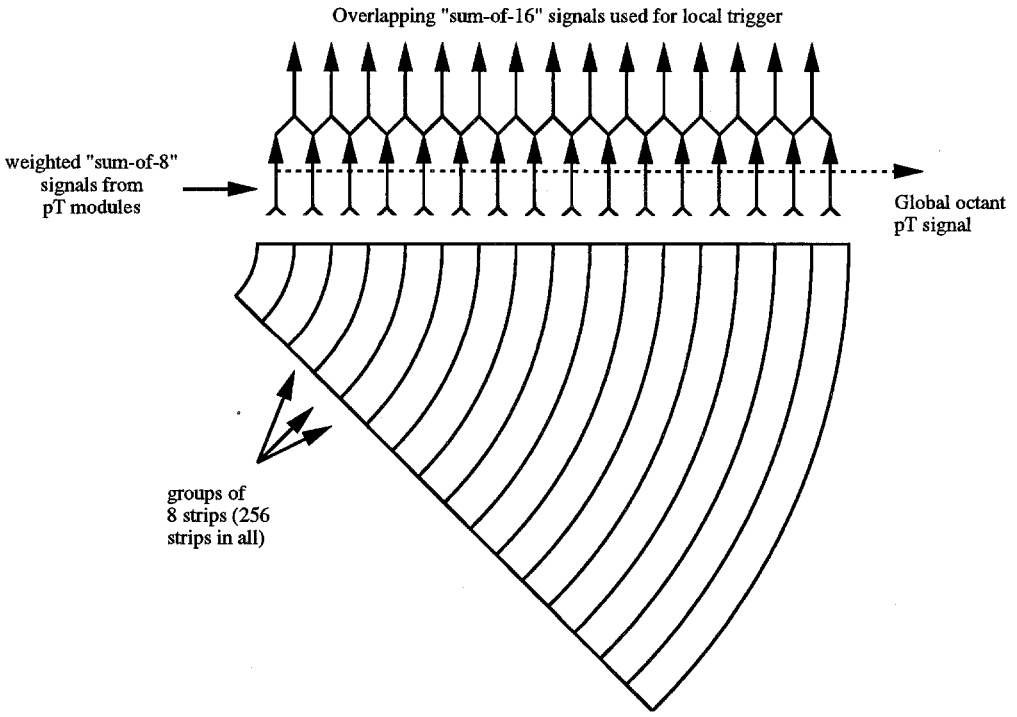

Figure 3.4: Local trigger signal formation from the R strip signals

The Prescaled Triggers

In order to study our trigger biases, we defined several low bias triggers. There were three prescaled triggers:

- The prescaled beam trigger
- The prescaled interaction trigger.
- The prescaled pretrigger.

Chapter 4

Event Reconstruction

4.1 Structure Of The E706 Reconstruction

Experiment E706 divided the data reconstruction into six distinct parts:

- DLREC(Discrete Logic REConstructor) was used for the trigger logic and cerenkov detector reconstruction.
- PLREC(PLanes REConstructor) was used for reconstructing the tracks of charged particles in our tracking system.
- EMREC(Electro-Magnetic REConstructor) was used to reconstruct electromagnetic showers in the EMLAC.
- HCREC(Hadron Calorimeter REConstructor) was used for the reconstruction of hadronic showers in the HALAC.

- FCREC(Forward Calorimeter REConstructor) was used for the reconstruction of energy in the FCAL.

- MUREC(MUon REConstructor) was used by E672 for the reconstruction of charged tracks in the downstream muon spectrometer.

MAGIC was the interface between the raw data written to tape and the various reconstruction packages. It was responsible for unpacking raw information from the various detector components, file handling, reading in the run constants, and other job initialization procedures. It then called the the reconstructors listed above.

MAGIC was written in FORTRAN 77. It used PATCHY for code management as well as ZEBRA for dynamic memory allocation. MAGIC was used for studies on its own and also wrote out ZEBRA banks with reconstructed data called DST's (Data Summary Tapes). These DST's were very convenient when used for physics studies. They allowed one to process high statistics in a short period of time. For the 1990 run approximately 700 raw data tapes were used to produce 100 DST's.

In the following sections a brief summary of the various reconstructors called by MAGIC to produce the DST's is given.

4.2 Reconstruction Of The Trigger Logic

DLREC had two basic purposes: First, DLREC checked the consistency of information read out by the trigger logic. If inconsistencies were found then various bits were set in the trigger quality words. These words were used during the analysis and during data acquisition to monitor the trigger logic units.

Second, DLREC produced the DL summary bank. This bank contained the status of the various triggers for each octant of the LAC. This gave us information offline about which of the triggers were satisfied for a given event.

4.3 Reconstruction Of Charged Tracks

The trajectories of charged particles were reconstructed using the upstream silicon beam and vertex chambers and the downstream proportional wire and straw tube drift chambers. The particle momentum was determined by measuring the bend of the reconstructed track in the dipole magnetic field. The routine used for the track reconstruction was called PLREC.

PLREC itself was divided into several routines corresponding to the steps of track reconstruction:

- PWC track finding
- SSD track finding

- PWC - SSD linking
- Primary vertex finding
- Beam track finding
- Straw track finding

4.3.1 PWC Tracking

The first step in track reconstruction was making PWC tracks downstream of the analysis magnet. The PWC's were constructed with four planes or views: the XZ and YZ planes were orthogonal to each other and the UZ and VZ planes were orthogonal. The UZ and VZ planes were rotated about the Z axis by the arctangent of $\frac{4}{3}$ with respect to the Y axis. Using the two coordinate systems we were able to correlate the x-view tracks with the y-view tracks and reconstruct 3-d space tracks.

View track finding was done in the following way:

- Using alternate sets of trial "seed" planes, all possible track candidates were made by connecting the hits of the first plane with the hits of the second. These track candidates are called "roads".
- Each road was projected into the remaining planes. A hit was searched for within 1.5 wire spacings of the road.

- The least squares method was use to create the most probable track given the hits along the "road".

After the view tracks were found an attempt was made to correlate them into 3-d space tracks. Each space track had to have at least 13 hits associated with it in order to be reconstructed in the first stage. In addition a thirteen hit space track must have a χ^2_{DOF} of 2.0 or less while 14, 15, and 16 hit tracks must have a χ^2_{DOF} of less that 3.0.

After reconstructing all space tracks with thirteen or more hits, hits used by these tracks were removed and the remaining hits were used in the second and third stage tracking. These stages endeavored to reconstruct tracks which were outside of the acceptance of PWC 3 and/or PWC 4. These tracks could have a maximum of 12 hits and so were not reconstructed in the first stage.

4.3.2 The Straw Tracking

The PWC tracks were projected into the straw chambers and a search was made for straw hits in the closest tube. The straw tubes had much finer resolution than the PWC's due to their use of timing information. Because of this high resolution we were forced to reduce other systematic errors such as those due to alignment uncertainty to much smaller levels than we would with the PWC's alone. Because of the improved resolution, we had to know the transverse position of each tube to

better than 200 microns.

As mentioned earlier, the straw tube drift chambers employed timing measurements to improve hit resolution. Relations between the distance of the hit from the wire and the tdc time had to be derived from the data. As a first approximation, PWC tracks were used. The distance between the track projection and the wire was plotted vs. the recorded tdc time. Then this relation was applied to reconstruct straw hits. These hits were then used to fit a new track and the process was repeated in an iterative method. A typical distance vs. time curve is shown in figure 4.1. The distance versus time curve is fit to a quadratic form. The range of the distance plotted represents the distance from the central wire to the tube wall. The flatening out of the curve near the wire is an artifact of the profile plot. For each value of tdc time, there is a range of corresponding distances which form a band about a mean value. However, Since time can never be negative, the average values are skewed at small distances. The quadratic shape of the curve is expected since the E field of the wire is inversely proportional to radial distance from the wire.

When hits were used to fit a track it had to be decided if the hit belonged on the track or was a noise hit or belonged to another track. To make this decision we had to have some idea of the error or resolution of the hit. It turned out that the resolution depended on the distance of the hit from the wire. Another way to parameterize this dependence was to use the tdc time. Residual plots were made of the reconstructed straw track and the hit for time bins of 7 ns. The plots were

fit to a gaussian and the widths of the gaussian were fit as a function of tdc time. Figure 4.2 shows a representative hit error vs. tdc time. In this figure the uncertainty minimum is approximately midway between the wire and the tube wall. At short times (hit very near the wire) an uncertainty exits due to the relatively few electrons that avalanch toward the wire. At large times (hit very near the tube walls) the electric field may be distorted contributing to a relatively large uncertainty in the timing. The straw tracking routine used weights based on the parameterization of this curve for the least squares track fitting.

4.3.3 PWC And STD Alignment

The precision alignment of the downstream chambers turned out to be a long and challenging task. The resolution of the PWCs was about 700 microns but the 250 micron resolution of the straws required that the alignment be known to 200 microns or better. Since I worked on the straw tube alignment I will limit my discussion to the straws. The PWC alignment will be discussed elsewhere [36].

The straw chambers were aligned with respect to the PWC coordinate system. PWC tracks where projected into the straw chambers and the residual, defined as the difference of the projected track and the nearest hit in the straw plane, was calculated. It was assumed that random processes might smear a hit to either side of a track and that the hit distribution would be gaussian, centered on the true trajectory of the particle. If the chamber was shifted to the right and we did not

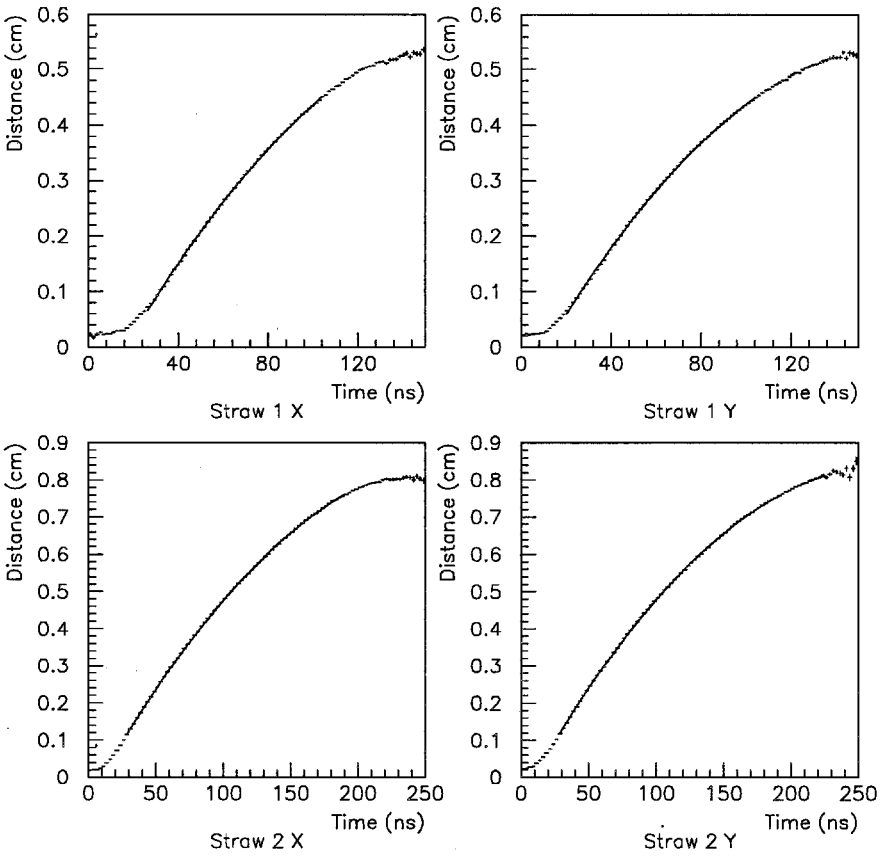

Figure 4.1: Distance of the straw chamber hit from the wire versus tdc time

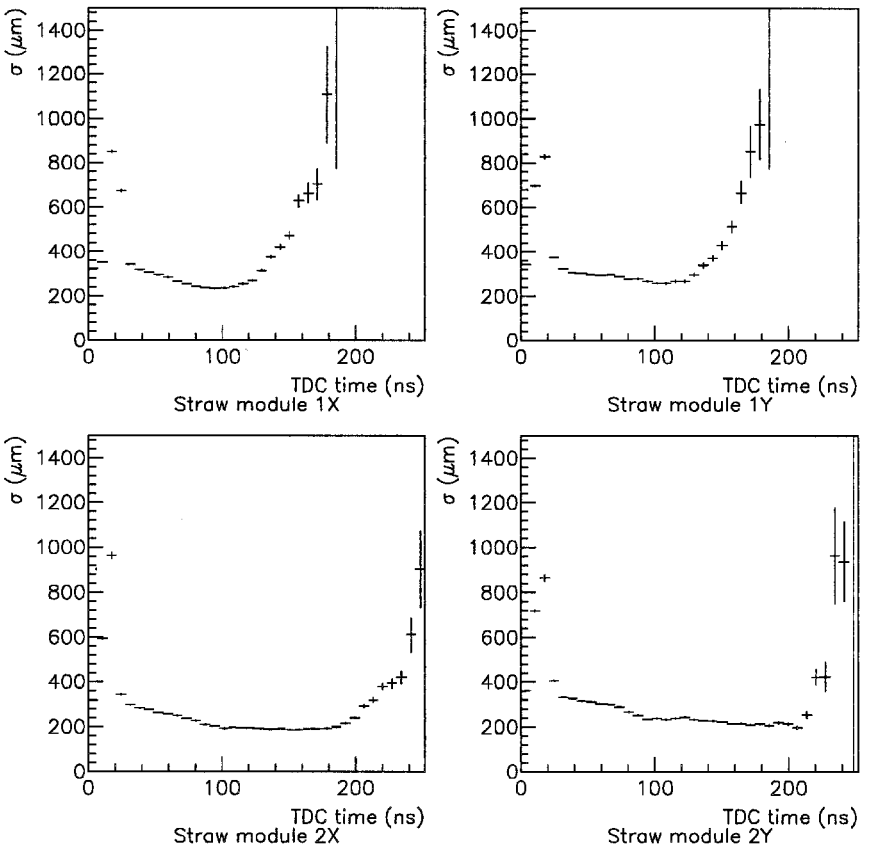

Figure 4.2: Uncertainty associated with straw chamber hit versus tdc time

account for this shift in the track reconstruction program, we would see that the residual gaussian would not lie on zero but would be shifted by an amount equal to the shift of the chamber. Making a residual plot for each straw plane gave us the transverse alignment for that plane.

We were also sensitive to shifts along the beam (longitudinal) direction. The signature of a longitudinal shift is a slope-dependent mean residual. If we plot the mean residual of the downstream track vs its slope, then a chamber shifted longitudinally will show a slope in this variable. A simple geometrical calculation showed that the slope of this plot is equal in magnitude to the shift of the chamber.

Often times the chambers were rotated about one or more of the three axes. For rotations about the z-axis, a plot of mean residual vs. transverse coordinate was made. To first order (i.e., small angles) the slope of this plot was equal in magnitude to the angle that the chamber was rotated. To get the other angles (about the x and y axes) we had to rely on surveyor measurements. These measurements were usually good to 1/128th of an inch.

It turned out that due to the unique construction of the first straw chamber, each bundle had to be adjusted for the transverse spacing between its neighbors and rotations about its center. These corrections were made for both straw chambers. We stopped short of aligning each tube individually. The results of the straw chamber alignment speak for themselves.

Figures 4.3 and 4.4 show the dramatic improvement obtained by using the

straw chambers. These figures show the window that is used to determine whether to link and upstream and downstream track. The window is made as small as possible in order to avoid multiple links between upstream and sownstream tracks. The high resolution of the straw chambers allow for a smaller window and more certainty in the link. Since any uncertainties in linking are propagated as uncertainties in the bend angle of the track at the center of the magnet, this improvement in linking shows up clearly in the momentum resolution.

4.3.4 Upstream Tracking

E706 employed a silicon strip detector, placed in the target box, to reconstruct the primary vertex. The upstream silicon tracking was done in a way similar to the downstream PWC tracking. Unlike the downstream tracking, the ssd's had only two views, xz and yz. We were thus forced to rely on the downstream tracking to associate upstream xz and yz tracks.

The SSD tracking was also done in two stages. The 4 and 5 hit tracks were reconstructed first, followed by the three hit tracks.

4.3.5 Upstream-Downstream Track Linking

In order to precisly determine the particles momentum, it was necessary to link tracks from the upstream and downstream systems. Tracks from each system were projected to the center of the magnet and matches were determined within

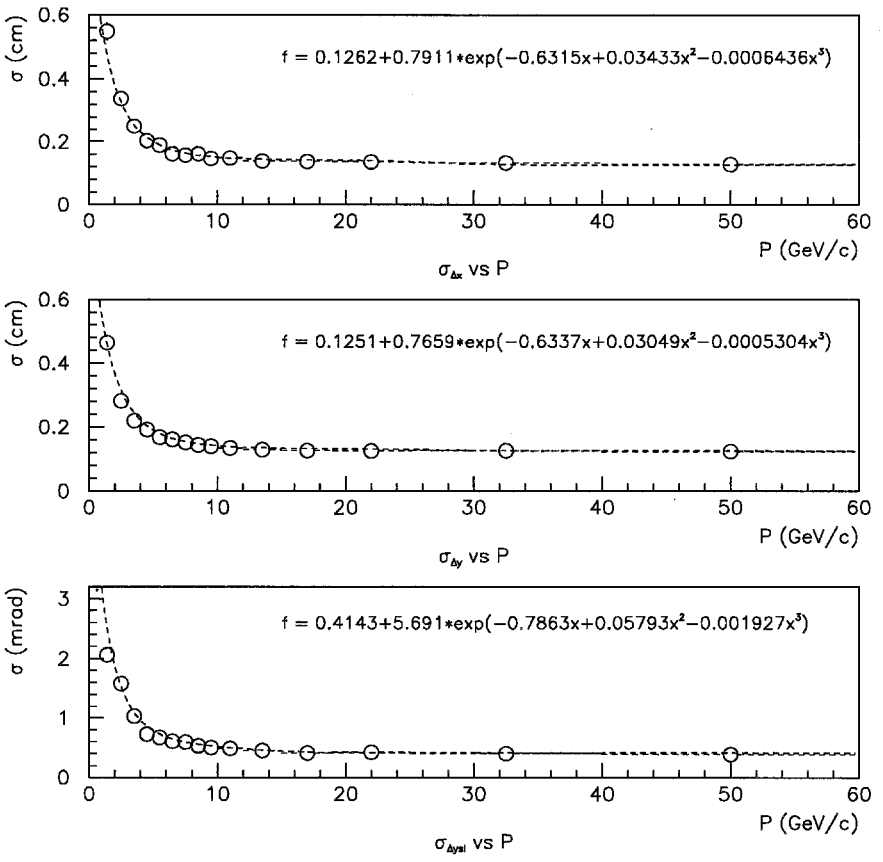

Figure 4.3: Momentum dependent linking window for PWC tracks. This plot shows the window used to determine whether or not to link an upstream and with a downstream track. Both track segments are projected to the center of the magnet and must each lie within a momentum dependent window determined by the above curve.

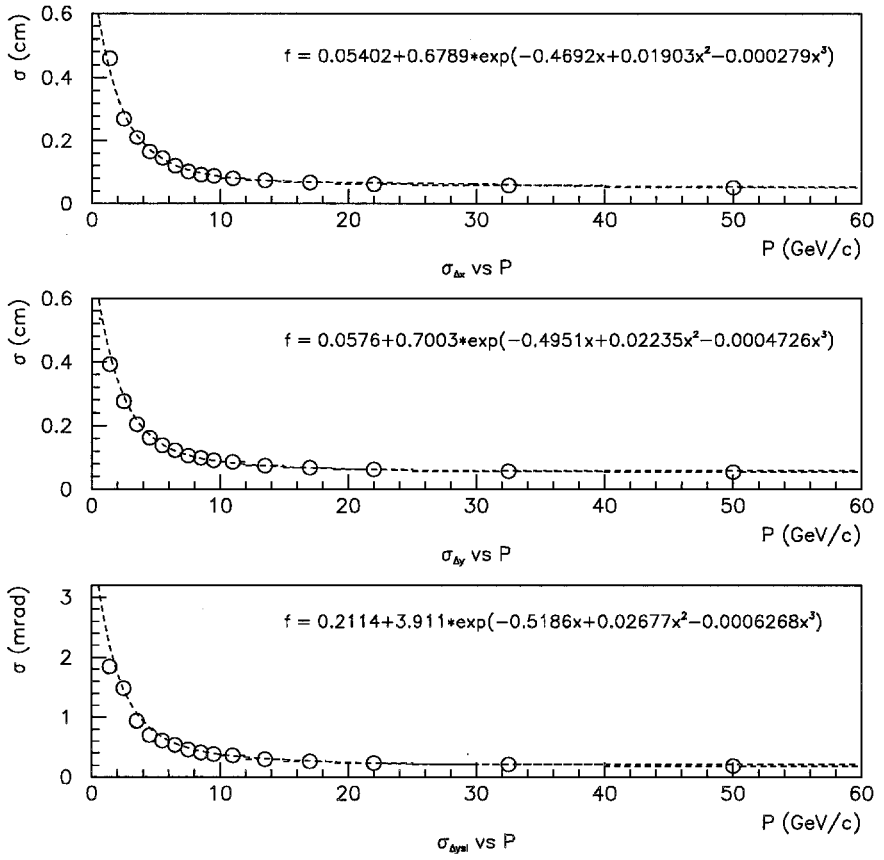

Figure 4.4: Momentum dependent linking window for STD tracks. This plot shows the advantages of including straw hit information in the reconstruction of the downstream track. Using the higher precision of the straw chambers translates to a smaller uncertainty in the track parameters. This in turn leads to a smaller projection uncertainty at the center of the magnet and therefore better linking resolution.

a momentum dependent linking window (see figure 4.3). A rough estimate of the momentum was needed, before the actual linking was done, to determine the size of this window. The estimated momentum was determined by assuming that the downstream track had originated from the primary vertex. In addition to the window requirement, the slopes of the upstream and downstream tracks in the non-bend (y-view) had to be consistant within a momentum dependent uncertainty. When the linking was completed, tracks could be catagorized as unlinked, linked in one view, linked in both views, or having multiple links in one or both views. The existance of a straw track aided in reducing the number of tracks with multiple links. Because of the much finer resolution of the straw tracks, a narrower linking window was used (see figure 4.4).

4.3.6 Momentum Determination

The momentum was determined after the the tracks were linked. The bend angle of the tracks in the x-view were used to measure the momentum using a square field approximation:

$$q = sign(\theta_1 - \theta_2) * sign(B_0) \tag{4.1}$$

$$P_T^{kick} = eB_0L_0 \tag{4.2}$$

$$\sqrt{p_z^2 + p_x^2} = \frac{p_T^{kick}}{sin\theta_1 - sin\theta_2} \tag{4.3}$$

$$\frac{p_x}{p_z} = tan\theta_x \tag{4.4}$$

$$\frac{p_y}{p_z} = tan\theta_y \tag{4.5}$$

The sign of the charged track, q, is calculated in equation 4.1. The magnitude of the effective magnetic field, B_0, and the effective magnetic field length, L_0, were used to calculate the P_T kick, in the thin lens approximation, in equation 4.2. The entrance and exit angles of the track in the xz plane, θ_1 and θ_2, and the P_T kick were used to calculate the three components of momentum, p_x, p_y, and p_z in equations 4.3, 4.4, 4.5. Tanθ_x and tanθ_y are the upstream x and y slopes, respectively.

4.4 The Electromagnetic Shower Reconstruction

Showers in the EMLAC were reconstructed by EMREC. EMREC used a two parameter shower shape function to find the energy and position of the shower. Since the total deposited energy was split evenly between the r and ϕ views, because the r and ϕ boards were alternated in the ENLAC, r and ϕ showers with similar energies were defined as one shower.

4.4.1 Shower Reconstruction: The EMREC Algorithm

As mentioned in chapter 2, the front and back sections of the EMLAC were read out independently. The summed section was created by adding corresponding strip contributions from these two sections. The summed section was searched for groups of adjacent strips whose energies exceeded 80 MeV (95 MeV for the outer ϕ

view) [28]. This was a potential electromagnetic shower.

The next step was a further refinement. A search was made for peaks and valleys within the groups. Each group was scanned from the left edge of the group to the right edge for local maxima and minima. A maximum bounded on either side by a minimum was defined as a peak. In chapter 2, it was mentioned that the separation of the EMLAC into a front and a back section was useful in resolving two closely spaced showers. To do this, a search for peaks was made in the front section only. Since showers tend to spread out laterally as they pass through the EMLAC, by looking in the front section at two closely spaced showers, we could often resolve both of them. This was very important later when we tried to reconstruct a π^0 with a small opening angle.

After finding the peaks and roughly estimating their positions and energies, the next step was to precisely determine these values. To this end, a shower shape function was fit to each of the peaks. The shower shape function was a parameterization of the average electromagnetic shower as determined by the E706 Monte Carlo. These fitted peaks were called gammas in the EMREC jargon. The energy, E, of the shower was determined by minimizing the following χ^2 equation [28]:

$$\chi^2 = \sum \frac{(E_i - x_i E)^2}{\sigma_i^2} \tag{4.6}$$

The sum was over all of the strips in the group. E_i is the energy of the i-th strip, x_i is the shower shape estimate of the fraction of the shower energy contained in

the i-th strip, and σ_i approximates the energy dependence of the resolution of the Emlac [28]:

$$\sigma_i^2 = (0.22)^2 + (0.16)^2 E + (0.01)^2 E^2 \tag{4.7}$$

At this point, the energy and position of the shower had been estimated in the particular view only. Correlating the showers from the r and ϕ views was the next step. The segmentation of the EMLAC into left and right r as well as inner and outer ϕ made correlation easier. R view and ϕ view gammas were matched if they had similar energies.

4.4.2 The Hadron Reconstructor: HCREC

The hadron reconstruction code was less complex than the electromagnetic reconstructor. Since the hadron calorimeter was built with a pad geometry it was unnecessary to correlate different views. The intrinsic resolution of the hadronic calorimeter was coarse in comparison with the resolution of the EMLAC. This meant that less effort was needed in designing a reconstructor. A simple reconstruction algorithm would do the trick.

Like EMREC, HCREC searched for groups of adjacent pads with energies above a threshold. Each group had to contain two or more pads with energies above 7.5 GeV [29]. Also like EMREC, a group might be resolved into more than one hadron. But the conditions were much simpler. There was no shower shape

function used in the HCREC algorithm.

Chapter 5

Event Selection

The data used in this analysis are from the 1990-91 data sample. Studies of strange particles in recoil jets opposite π^0 or single photon triggers were undertaken. In order to extract a clean sample of high P_T π^0 and direct photon triggers, it was necessary to apply cuts to the data at the event level. These cuts were based on our understanding of our detectors, the beamline and interactions in our target. The following paragraphs describe the cuts used in this analysis. Further information can be found in other documents [35, 20, 24, 25, 28]

The study of events containing strange mesons and baryons first required identification of the strange decays. To accomplish this, certain assumptions were made with respect to the decay tracks of the particles of interest. Invariant mass plots were made using the $K^0 \Rightarrow \pi^+\pi^-$, or $\Lambda \Rightarrow p\pi^-$ or $\bar{\Lambda} \Rightarrow \bar{p}\pi^+$ hypotheses. Cuts were applied to increase the signal to background ratios. Care was taken that

a kinematic region was not excluded when these cuts were applied. Corrections to the data due to these cuts were determined from a Monte Carlo program when necessary.

In this section the strange particle selection process is discussed as well as the various relevant algorithms used for particle identification.

5.1 Pre-Selection Of Events

The search for strange particle decays primarily used the tracking system. Before starting the search, the quality of the event with respect to the upstream and downstream tracking systems was investigated. The event was cut if any of the following occurred:

- Too many hits in the beam or vertex silicon strip detectors
- Too many hits in the proportional wire chambers
- Limits were reached in upstream or downstream tracking
- There was no matched vertex in the event
- There was no beam track within 50 μm of the primary vertex

5.2 Reconstruction Of The Strange Particle Candidate

The following steps were taken in order to reconstruct the decays of the strange particle candidates:

- Find the x, y, and z coordinates of the decay vertex
- Determine the momentum of each of the decay tracks
- Using the hypothesis that the secondary vee was due to either a $K^0 \Rightarrow \pi^+\pi^-$ decay, or a $\Lambda \Rightarrow p\pi^-$ decay, or a $\bar{\Lambda} \Rightarrow \bar{p}\pi^+$ reconstruct the candidate strange particles invariant mass.

5.2.1 Reconstruction Of The Decay Vertex

In order to reconstruct the location of the strange particle decay, it was necessary to cycle through all tracks in the event which met the following conditions:

- The track did not share too many of its hits with other tracks in the event.
    1. This helped to eliminate fake tracks constructed by the PLREC algorithm.
- The track was consistent with *not* coming from the primary vertex.

1. Since most tracks come from the primary interaction vertex this cut greatly reduces the number of track combinations used to make the secondary vees and thus increases the signal to background ratio.

The z coordinate of the intersection of pairs of tracks satisfying the above criteria was calculated using the slopes and intercepts of the downstream tracks in the yz plane. For the initial selection process, the z coordinate of the intersection was required to be between the downstream edge of the last beryllium target piece and the center of the dipole analysis magnet. The reconstruction of secondary vertices in the target was compromised due to the density of tracks in that region. Many track combinations were, however, already eliminated by the impact parameter cut. If a candidate neutral strange particle decayed downstream of the center of the analysis magnet there was not enough magnetic field length to get a reliable measurement of the momentum of the decay tracks. In both of these excluded regions the signal resolution was very poor.

Since to first approximation tracks were only bent in the x-z view, it was a simple matter to calculate the y position of the candidate vee.[1] The x coordinate of the vee, because of the magnetic field, required a more clever method.

[1]We often refer to a secondary vertex with only two decay tracks as a vee. We call it a vertex if it has three or more decay tracks. While the PLREC reconstructor gives us the slopes and intercepts of the two candidate tracks, it doesn't know where the tracks originate. We calculate the crossing point of the two tracks and assume that this "vee" is the origin of the tracks. Thus, by now calling it a vee instead of a crossing we have made a deduction that PLREC is unable to duplicate.

During the course of this analysis two methods were used. Both methods relied on the assumption that transverse momentum was conserved during the decay. We assumed that the decay particles had an equal and opposite momentum transverse to the strange particle's momentum vector. The first algorithm involved looping over x coordinate candidates, determining the momentum of the decay tracks based on the x,y, and z coordinates of the vee, (momentum determination will be discussed shortly) and calculating a normalized transverse momentum difference between the two tracks. These steps were repeated for a range of x coordinates based on our charged track acceptance. The x value which gave the minimum transverse momentum difference between the two tracks was taken to be the true vee x coordinate. This method was used to select events with candidate strange particles and write them to the strange selection tapes. All further analysis was done using these tapes.

The second method [38] involved the calculation of the momentum of the decay tracks as if they originated from the primary vertex. The sum of the momenta calculated in this manner was proportional to the actual K^0 momentum, i.e. this momentum vector lied along the line connecting the primary and secondary vertices. (See equation 4.1 thru 4.5). Using this information with the z coordinate of the decay vertex obtained from the non-bend view and some simple geometry, the x coordinate of the secondary vee was determined (See figure 5.1).

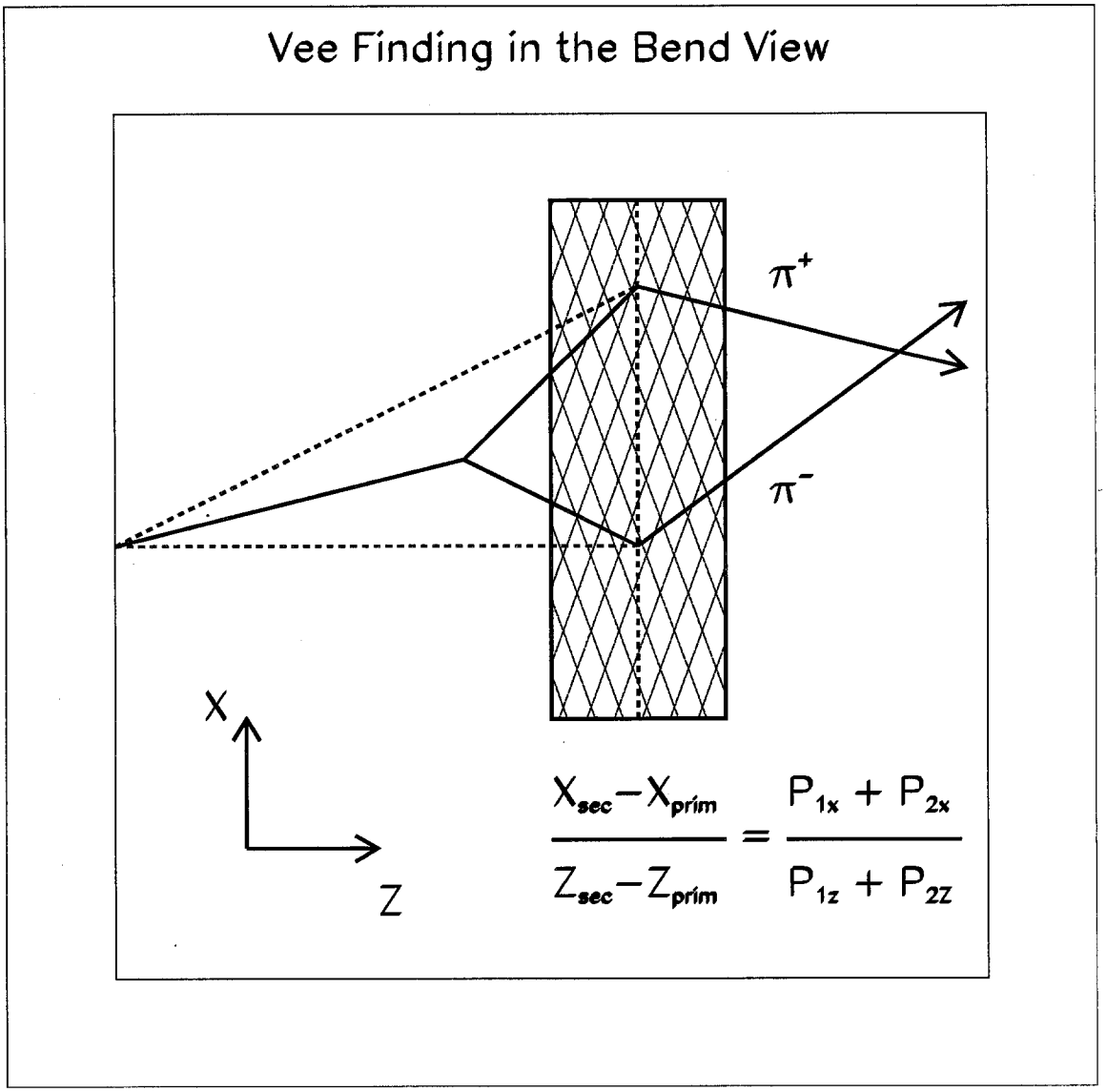

Figure 5.1: Reconstruction of the X-coordinate of the vee. The coordinates of the primary vertex ,Z_{prim} and X_{prim}, are used with the downstream track parameters in the momentum calculation. The momentum reconstructed in this manner ($\vec{P_1} + \vec{P_2}$) is proprotional to the true momentum of the K^0. This information, combined with the value of Z_{sec} calculated from the non-bend view, can be used to determine the value of the x coordinate of the decay vertex, X_{sec}.

Although both methods gave similar results, the second method had the additional advantage that no looping was involved. This cut the running time of the selection code in half. Therefore the second method was chosen for this thesis.

With all three coordinates of the vee computed the momenta of the two decay tracks were recalculated assuming that the tracks originated from the vee. For the momentum determination, the square field approximation was used, assuming that the tracks were bent at the center of the magnet. The momentum algorithm first decided where the *effective* center of the magnet was located. If the particle decayed upstream of the pole piece of the dipole magnet then the decay tracks would have experienced the whole magnetic field length. Otherwise, if it decayed inside the magnet, they would have experienced only a fraction of the field length so that the effective center of the magnet would be shifted downstream relative to the geometric center. The slopes and intercepts of the downstream tracks were calculated by PLREC. To reproduce the upstream trajectories, it was assumed that the decay tracks came from the vee and that they connected with their downstream counter parts at the center of the magnet. The $\int \vec{B} \cdot d\vec{l}$ was divided by the difference between the sine of the entrance angle (upstream track) and the sine of the exit angle (downstream track).

Since we were interested in the decay of neutral strange particles into two oppositely charged decay products, we also demanded that the electric charge of the two tracks be opposite in sign.

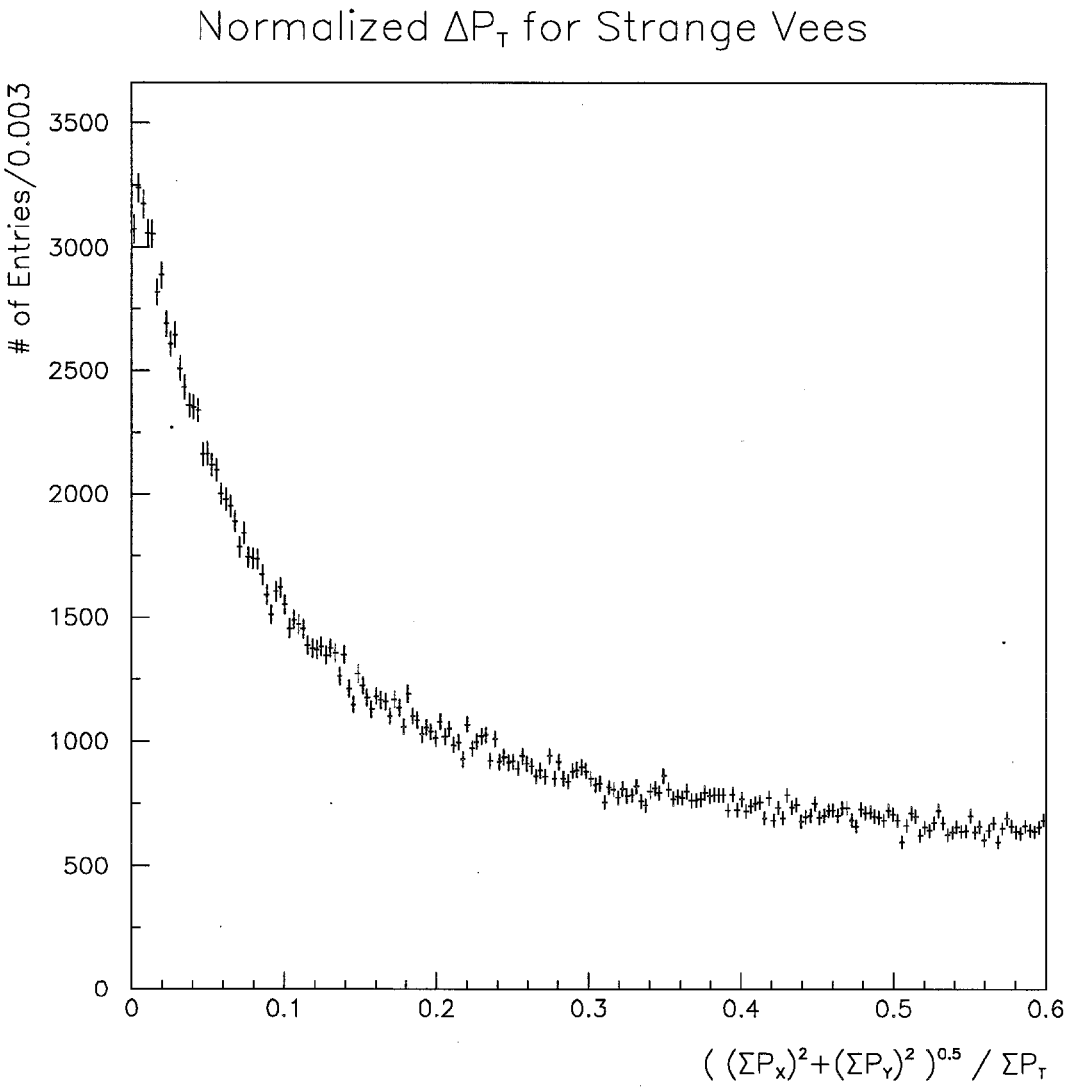

Figure 5.2: Normalized ΔP_T for reconstructed secondary vees. P_T is with respect to the candidate neutral strange particle.

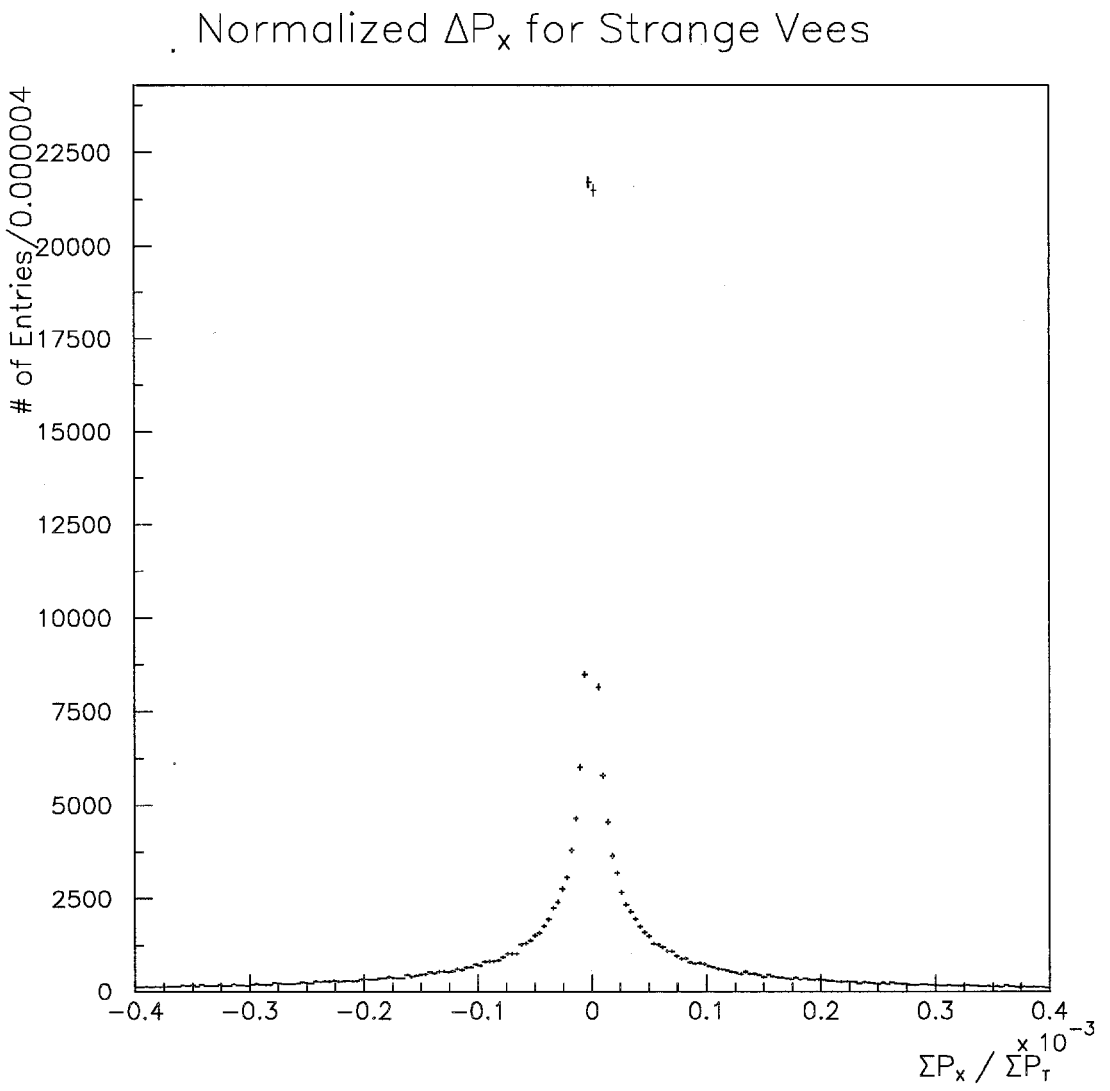

Figure 5.3: Normalized ΔP_X for reconstructed secondary vees. P_X is with respect to the candidate neutral strange particle.

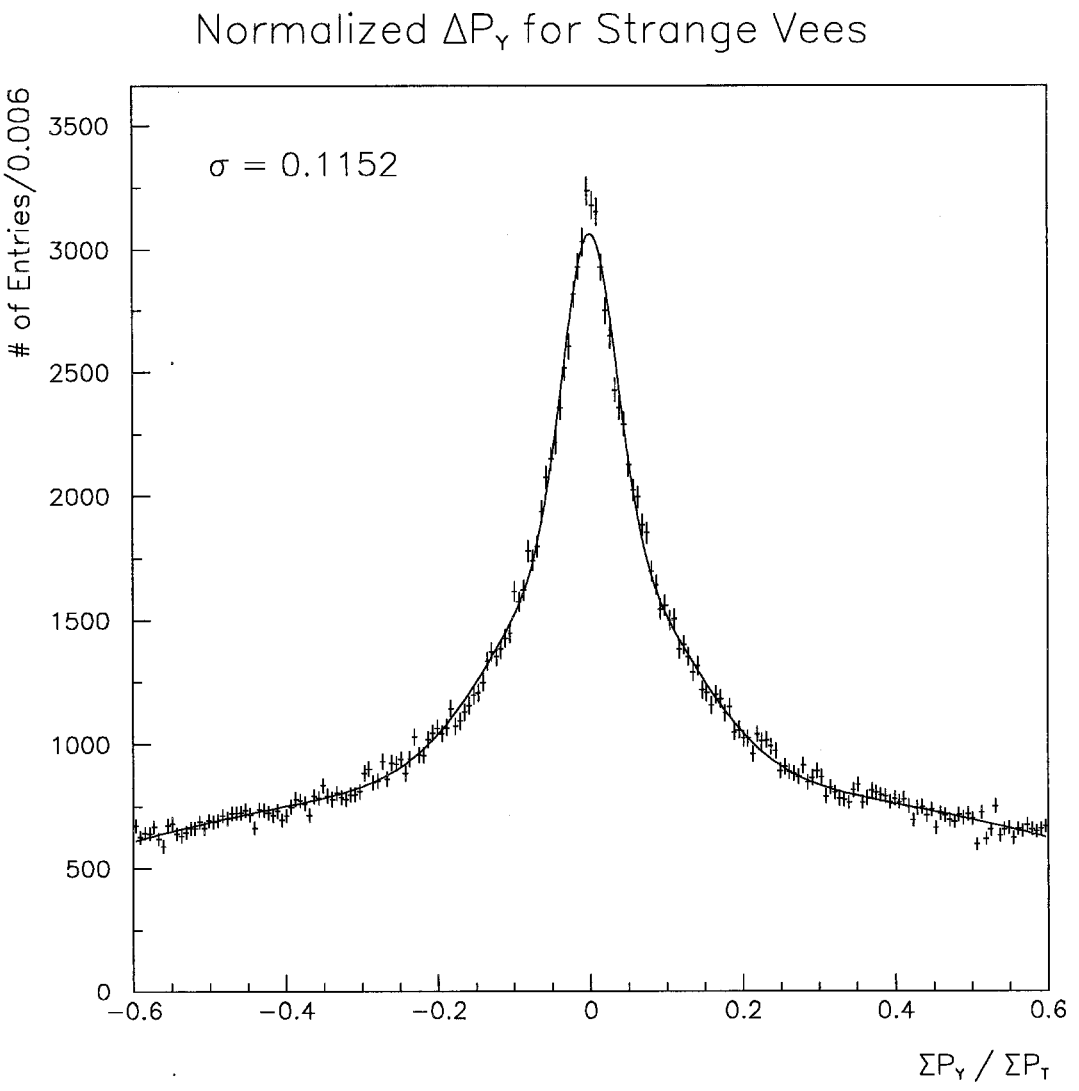

Figure 5.4: Normalized ΔP_Y for reconstructed secondary vees. P_Y is with respect to the candidate neutral strange particle.

After the momenta of the two decay tracks was determined, we checked the P_T of the tracks with respect to the strange particle trajectory to see how well they balanced. We used the following normalized variable:

$$\Delta^{Normalized} P_T = \frac{\|\vec{P}_T^{\pi^+} + \vec{P}_T^{\pi^-}\|}{\|\vec{P}_T^{\pi^+}\| + \|\vec{P}_T^{\pi^-}\|} \tag{5.1}$$

This variable gave us an indication of how well our algorithm did in the reconstruction of a strange particle vee (see figure 5.2.) $\vec{P}_T^{\pi^+}$ consists of two components, e.g. ($P_X^{\pi^+}$, $P_Y^{\pi^+}$), which are taken with the z-axis along the momentum vector of the candidate strange particle.

With the momentum information we could now test the hypotheses of our vee being due to the decay of a strange particle (either a K^0, Λ or $\overline{\Lambda}$). The K^0 hypothesis involved assuming that the decay tracks were due to charged pions and used this assumption to calculate the $\pi^+\pi^-$ invariant mass. Similarly, the Λ hypothesis assumed that the positively charged track was due to a proton and the negatively charged track was due to a π^-, while the $\bar{\Lambda}$ hypothesis assumed a $\bar{p}$ and a π^+.

5.3 Cuts On Strange Particle Candidates

In order to enhance the signal to background ratio in our strange particle sample, we subjected the data to various cuts. These cuts were motivated by extensive use of the Monte Carlo and by our assumptions of the properties of the strange

particles.

The various cuts are listed below:

- For the K^0, Λ and $\bar{\Lambda}$ hypothesis each track was required to have b/$\sigma > 1.0$, where b is the impact parameter of the track at the primary vertex and σ is the uncertainty in the track projection at the primary vertex.
- The z coordinate of the decay had to be between 12 cm from the downstream end of the last piece of beryllium and the center of the magnet.
- The normalized ΔP_T between the two decay tracks in the rest frame of the strange particle had to be less than 0.6.
- The decay tracks had to be oppositely charged
- The P_T of the strange particle, relative to the beamline, had to be greater than 0.25 GeV.
- K^0–Λ Ambiguity
  1. The K^0 candidates had to have a value of $\|cos(\Theta^*)\| > 0.75$
  2. The pπ^- pair which made a Λ candidate had to have a $\pi^+\pi^-$ invariant mass < 0.477 GeV.
  3. The $\bar{p}\pi^+$pair which made a $\bar{\Lambda}$ candidate had to have a $\pi^+\pi^-$ invariant mass < 0.477 GeV.

- mass cut

  1. In order to satisfy the K^0 hypothesis the $\pi^+\pi^-$ invariant mass had to be between 0.35 and 0.65 GeV.
  2. In order to satisfy the Λ hypothesis the $p\pi^-$ invariant mass had to be between 1.055 and 1.175 GeV
  3. In order to satisfy the $\bar{\Lambda}$ hypothesis the $\bar{p}\pi^+$ invariant mass had to be between 1.055 and 1.175 GeV

each of these cuts will be discussed in turn in the following sections.

5.3.1 The Impact Parameter/σ cut

Since we were looking for the decay tracks of a strange particle which had been created in the primary hard scatter and subsequently decayed at a later time, we expected this secondary vertex to be displaced from the primary vertex. Therefore, in order to avoid making spurious combinations with tracks that come from the primary vertex, we eliminated these at the start by imposing the requirement that the impact parameter (b) of the downstream y-view tracks at the primary vertex be sufficiently large. To calculate the impact parameter we used the downstream slope and intercept in the yz view (the non-bend view) to project the track back to the primary vertex. Then we looked at the difference between the y coordinate of the primary vertex and the y coordinate of the projection at the z coordinate

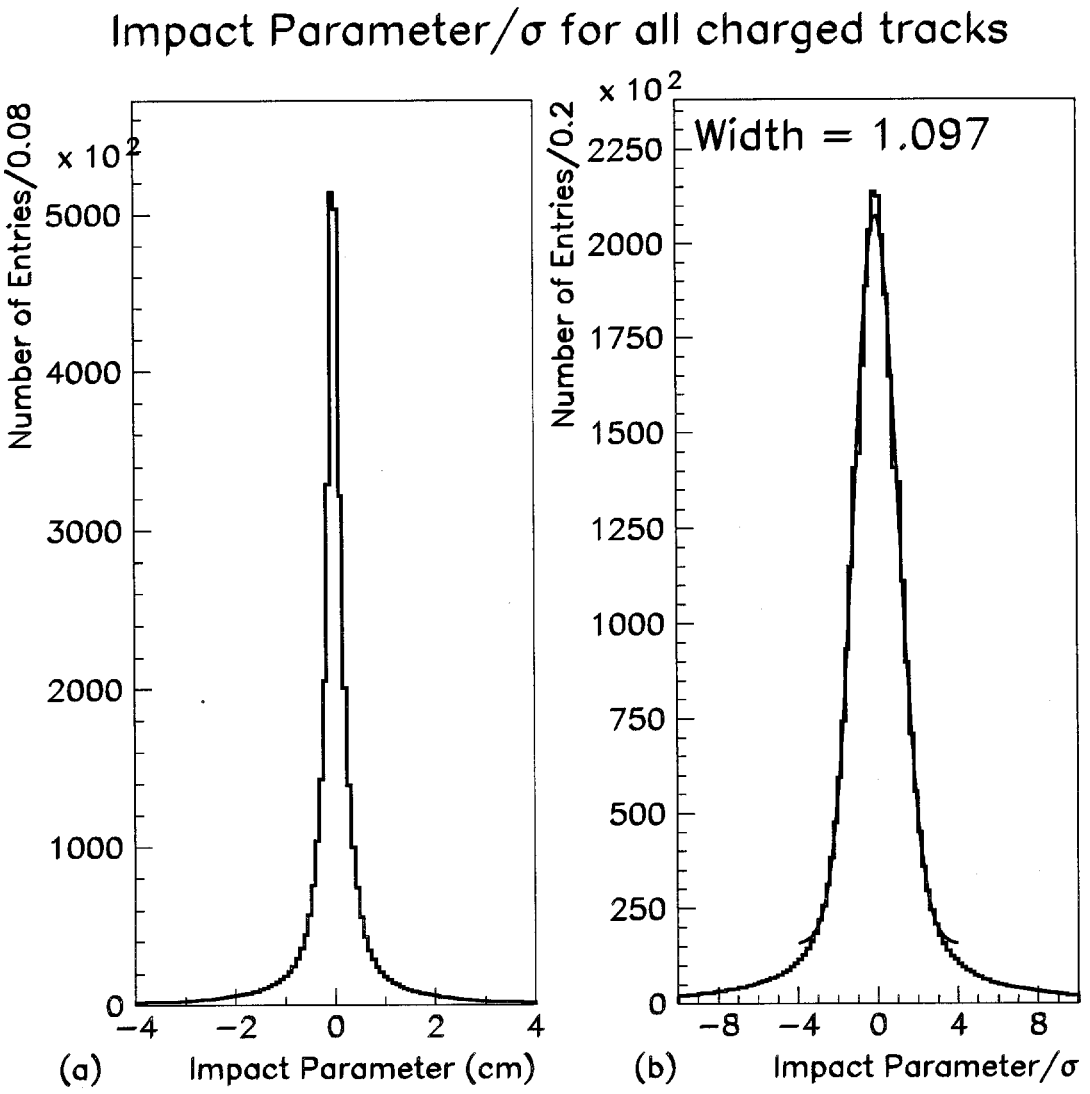

Figure 5.5: (a) Impact parameter and (b) impact parameter/projection uncertainty for all charged tracks.

of the primary vertex (see figure 5.5.) This projection had uncertainties associated with it which depended on such things as the uncertainties in the calculated slope and intercept of the downstream track. We then formed a dimensionless quantity by taking the impact parameter and dividing it by its theoretical uncertainty. (see figure 5.5.)

We chose a loose cut of $b/\sigma > 1.0$ to enhance the signal to background ratio but not loose too much in the way of statistics. Some care had to be taken because the distance that the strange particle travels is proportional to its momentum. However to first order this dependence cancels in the calculation of the impact parameter [2]

5.3.2 Z Window Cut

For this analysis we allowed the decay to occur between 12 cm from the downstream end of the last beryllium piece in the target and the center of the dipole analysis magnet. The $\pi^+\pi^-$ invariant mass in this region is plotted in figures 5.6 and 5.7. a shift in the K^0 mass peak was observed near the upstream end of the magnet, at $z \approx 80$cm. This shift was due to fringe field effects not taken into account in the momentum determination. The effect of this fringe field is to shift the mean mass slightly ($\approx$ 5 MeV or less than one σ). For the present study, however, this

[2] Simple geometry will show that impact parameter $b \propto d\theta$ where d is the distance from the primary to the secondary vertex and θ is the opening angle between the two decay tracks. $d = \gamma\tau$ while $\theta \propto \frac{1}{\gamma}$

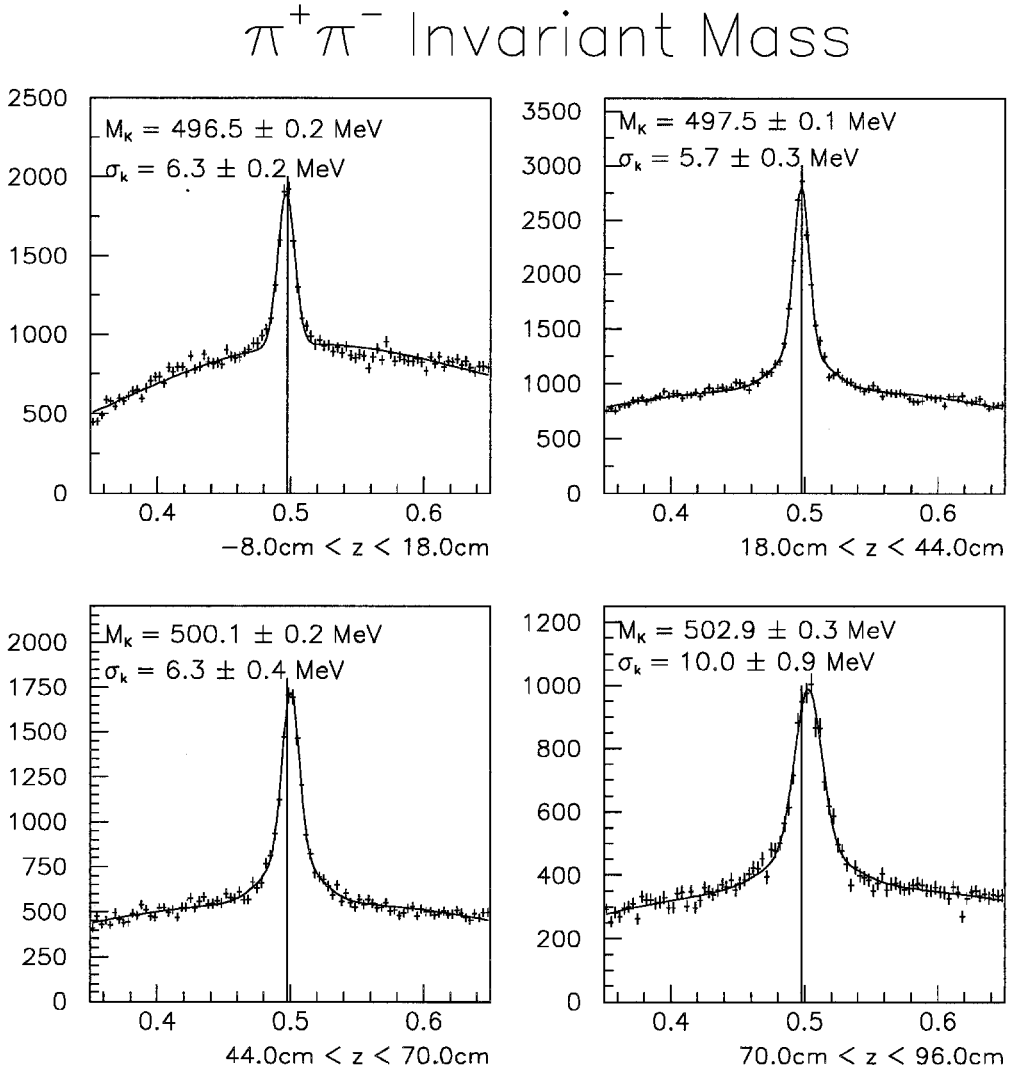

Figure 5.6: $\pi^+\pi^-$ invariant mass in different z bins, part 1.

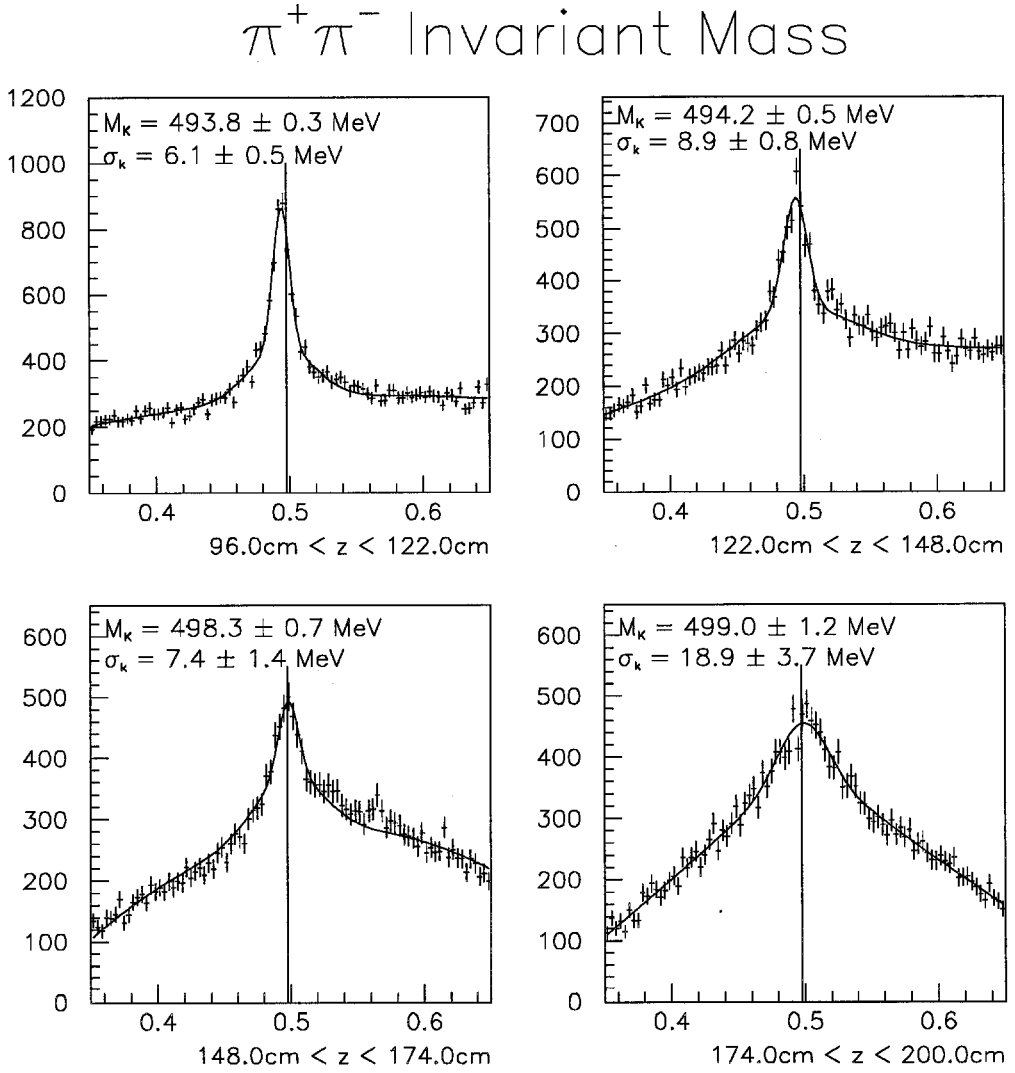

Figure 5.7: $\pi^+\pi^-$ invariant mass in different z bins, part 2.

was not an important issue. For this work, the number of entries above a fitted background, within a signal region of about 3σ from the mean, was used in a ratio. Any dependence in z appeared in both the numerator and denominator of this ratio. See chapter six for further details.

5.3.3 ΔP_T Of Decay Tracks

Under the assumption that in the rest frame of the strange particle the transverse momentum of the two decay tracks should balance, we imposed a cut on a normalized ΔP_T defined in the following manner:

$$Normalized\Delta p_T = \frac{\|\vec{P}_T^{\pi^+} + \vec{P}_T^{\pi^-}\|}{\|\vec{P}_T^{\pi^+}\| + \|\vec{P}_T^{\pi^-}\|} \tag{5.2}$$

This variable gave us an indication of how well our algorithm did in the reconstruction of the the secondary vee. The distribution is plotted for the region between the downstream end of the target to the center of the magnet in figure 5.2. The peak near zero is due to the correctly reconstructed vees while the background is from vees that were not consistent with the decay hypothesis. By using GEANT in single particle mode, so that all tracks were due to K^0's, it was discovered that the distribution for vees consistent with the kaon hypothesis cut off at a Normalized ΔP_T of 0.2. However, because the single track mode approximation does not take into account the amount of confusion that typically arises in a real event due to the much higher track multiplicities, we decided to move the cut out to 0.6. This

value is approximately a six σ deviation from the mean. To illustrate this, the y component of this variable was fit to two gaussians and a second order polynomial background (see figure 5.4). The value of σ shown in the figure represents the width of the wider of the two gaussians. The means of the two gaussians were constrained to be the same. The width of the x component of ΔP_T is negligible as shown in figure 5.3. The reason that the widths are so different is that the x position of the vertex is chosen by minimizing the difference in P_X of the decay products relative to the strange particle candidate.

Figures 5.8, 5.9, and 5.10 show the invariant masses under the $\pi^+\pi^-$, $p\pi^-$, $\bar{p}\pi^+$ hypotheses. Only the cuts discussed above have been applied to this plot. From these plots we estimate that we have 1,139,000 K^0's, 161,000 Λ's, and 93,000 $\bar{\Lambda}$'s after applying these cuts.

5.3.4 P_T

To remain consistent with the jet studies, it was decided to apply a P_T requirement of 0.25 GeV on the strange particle candidates. This cut was applied in the E706 jet analysis on all tracks in the jet. The contribution of low P_T particles to the jet direction was shown to be negligible [20]

5.3.5 $Cos(\Theta^*)$

Figure 5.8: $\pi^+\pi^-$ invariant mass after the impact parameter significance cut, the normalized ΔP_T cut, the z window cut, and chosing only decay tracks with opposite charges. The z range is from the berylium target to the center of the magnet. The curve used to fit the signal region is composed of two gaussian functions (for a total of six independent parameters). The mean value and width quoted in the figure are of the narrower gaussian function. The background region has been fit to a third order polynomial (four independent parameters). Using this fit it is estimated that we have 1,139,000 K^0 candidates.

Figure 5.9: $p\pi^-$ invariant mass after the impact parameter significance cut, the normalized ΔP_T cut, the z window cut, and chosing only decay tracks with opposite charges. The z range is from the berylium target to the center of the magnet. The function superimposed on this plot is a gaussian, for the peak region, with a second order polynomial background. Using this fit, it is estimated that we have 161,000 Λ candidates.

Figure 5.10: $\bar{p}\pi^+$ invariant mass after the impact parameter significance cut, the normalized ΔP_T cut, the z window cut, and chosing only decay tracks with opposite charges. The z range is from the berylium target to the center of the magnet. The function superimposed on this plot is a gaussian, for the peak region, with a second order polynomial background. Using this fit, it is estimated that we have 93,000 $\bar{\Lambda}$ candidates.

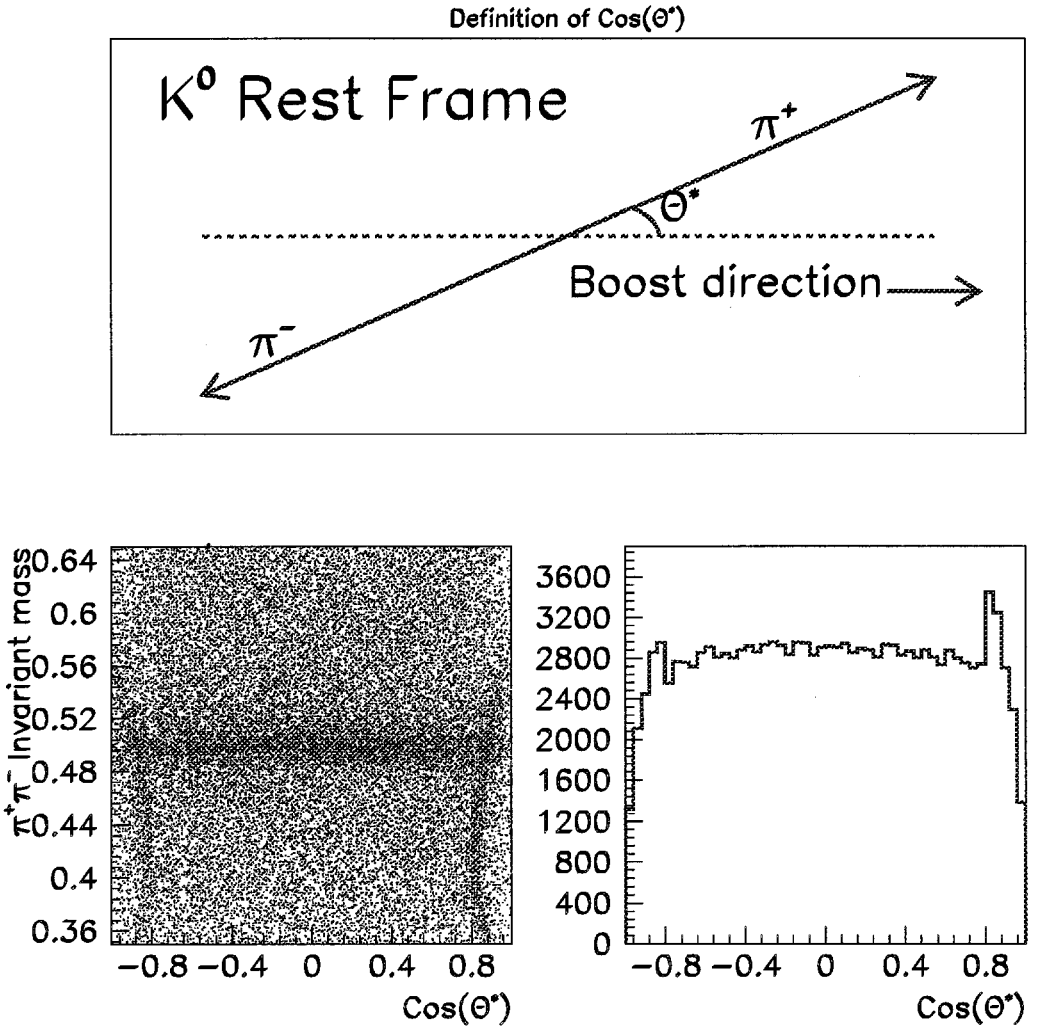

Figure 5.11: $\pi^+\pi^-$ Invariant Mass vs CosΘ^*

Θ^* was defined as the angle of the positive decay track with respect to the direction of the boost necessary to get to the strange particle rest frame (see figure 5.11.) This variable was defined using either a K^0, Λ or $\bar{\Lambda}$ hypothesis. For the K^0 hypothesis it was assumed that the positively charged track was a π^+. The π^+ was given a boost which depended on the momentum of the vee and the reconstructed $\pi^+\pi^-$ invariant mass. Similarly, for the Λ and $\bar{\Lambda}$ hypothesis the boost depended on the vee momentum and either the reconstructed $p\pi^-$ or $\bar{p}\pi+$invariant mass. Plots of the reconstructed invariant mass under K^0, Λ or $\bar{\Lambda}$ hypothesis versus CosΘ^* were used to understand the levels of contamination in the samples.

Since the K^0 is a spin 0 meson it was expected that, in its rest frame, the pions would be ejected at any angle with equal probability. This is shown in a plot of $cos(\theta^*)$ which should be flat for the generated K^0's. [3] If the proton from a Λ decay was improperly interpreted as a π^+ from the decay of a K^0, it would appear to be emitted at a small angle Θ^* in the center of mass. This is because the momentum of the misidentified proton would be given the wrong boost to the center of mass frame. Thus the misidentified proton would have a value of $cos(\Theta^*)$ around 1.0.

Similarly, in a $\bar{\Lambda}$ decay the π^+ would be given too large of a boost and appear to have a very large Θ^*. Thus for misidentified $\bar{\Lambda}$ decays we expect to see a value of $cos(\Theta^*)$ around -1.0. In the $cos(\Theta^*)$ plot (see figure 5.11) one can see a relatively flat inner region bounded by two peaks at $||cos(\Theta^*)||$ greater than 0.8.

[3] Actually it is not flat due to the limited acceptance of our spectrometer and possibly reconstructor effects and background.

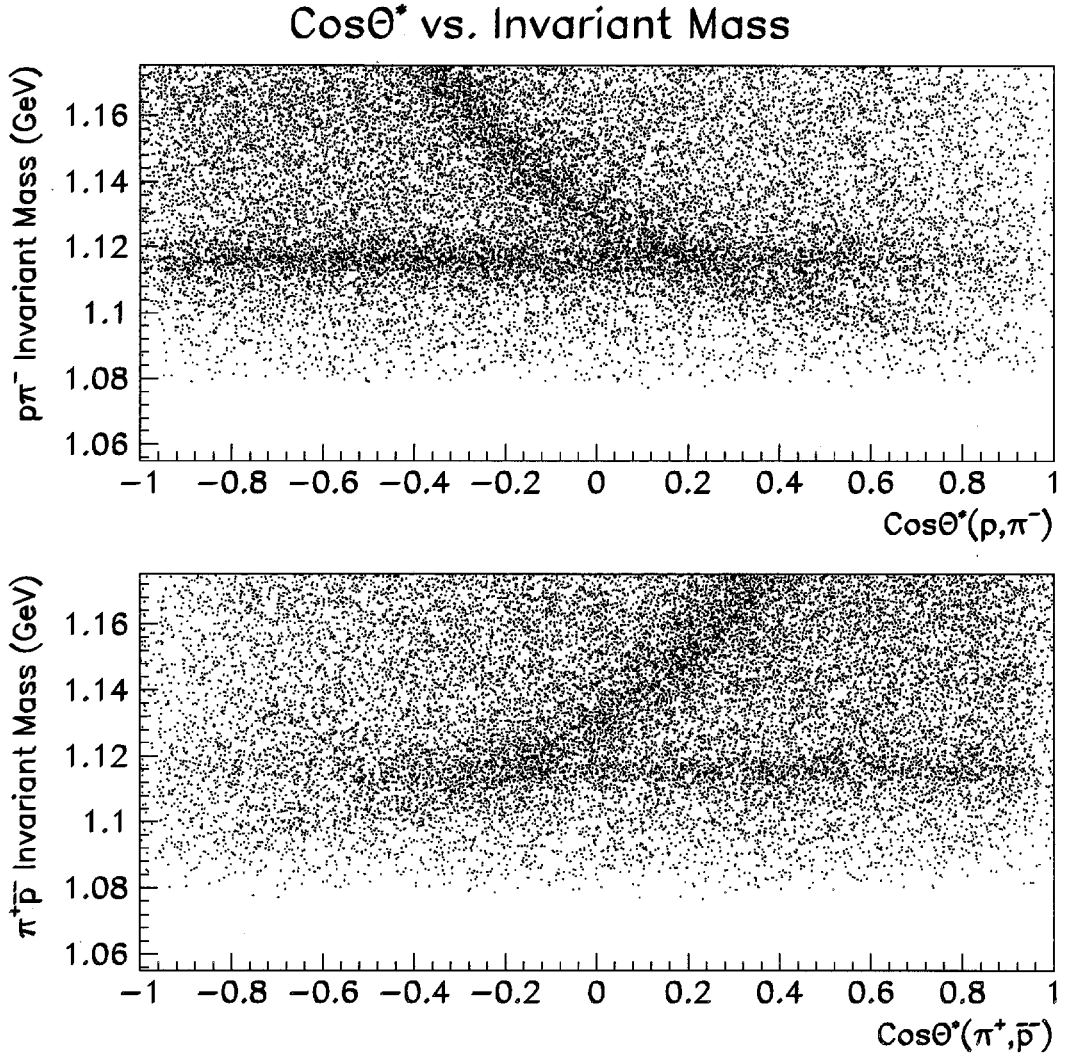

Figure 5.12: p π^- and $\bar{p}\pi^+$ Invariant mass versus CosΘ^*

These peaks are attributed to protons and π^+'s from Λ's and $\bar{\Lambda}$'s misidentified as π^+'s from K^0's. Figure 5.11 shows a plot of the $\pi^+\pi^-$ mass vs $cos(\Theta^*)$. In this plot we see an enhancement around the K^0 mass. In addition, we see two arcs running vertically. These arcs are attributed to misidentified Λ and $\bar{\Lambda}$ contributions to the $\pi^+\pi^-$ sample.

To study this further we used the E706 Monte Carlo. We alternately excluded generated K^0's, Λ's and $\bar{\Lambda}$'s and plotted the cosΘ^* distributions. In figure 5.13 plots of the $\pi^+\pi^-$ invariant mass versus cosΘ^* are shown alternately with K^0's and Λ's excluded. Shown in (a) is the $\pi^+\pi^-$ invariant mass versus $\|cos\Theta^*\|$ when Λ's and $\bar{\Lambda}$'s are excluded from the sample. There is a clear enhancement of statistics at the mass of the K^0 surrounded by a relatively uniform background. Plotted in (b) is the same thing but with K^0's excluded. In this case we see two arcs near cosΘ^* equal 0.8. These are attributed to Λ and $\bar{\Lambda}$ contamination in the $\pi^+\pi^-$ sample. This contamination complicates the estimation of signal in the K^0 peak.

In order to clean up the K^0 sample we chose to cut at $\|cos(\Theta^*)\|$ equal to 0.75.

It is also possible to have the Λ and $\bar{\Lambda}$ samples contaminated by misinterpreted K^0's decays. A K^0 decay with $\|cos(\Theta^*)\|$ around zero would produce a symmetric decay in the laboratory. Such a decay could be interpreted as a Λ or a $\bar{\Lambda}$ with a small laboratory momentum. Figure 5.12 shows the $p\pi^-$ invariant mass

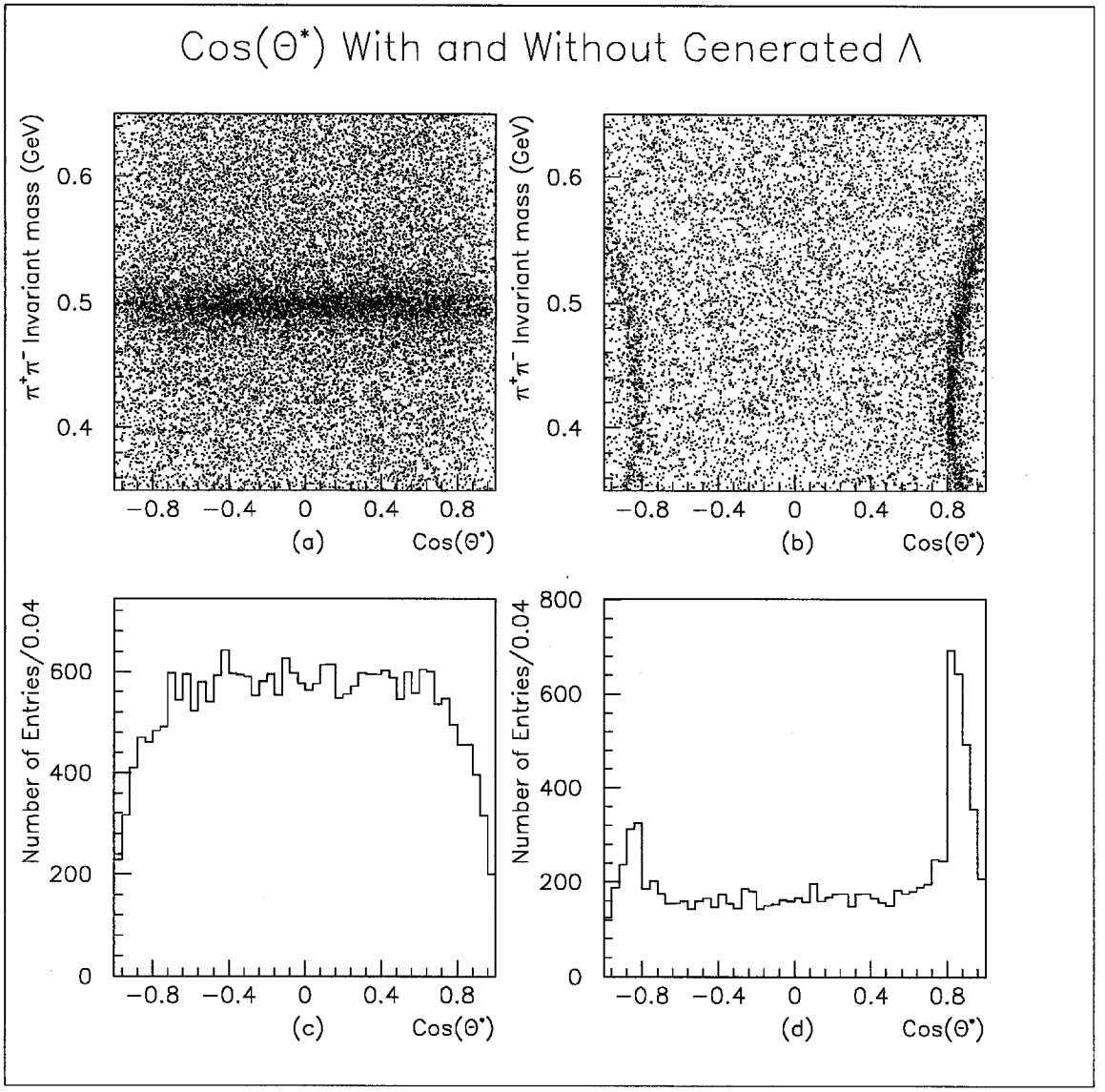

Figure 5.13: $\pi^+\pi^-$ Invariant mass versus CosΘ^* with generated K^0's or Λ's and $\bar{\Lambda}$'s removed from the sample. In (a) the $\pi^+\pi^-$ mass versus CosΘ^* is plotted with Λ's and $\bar{\Lambda}$'s removed. In (b) the same plot is shown with K^0's removed. (c) and (d) show the projections of (a) and (b) onto the CosΘ^* axis.

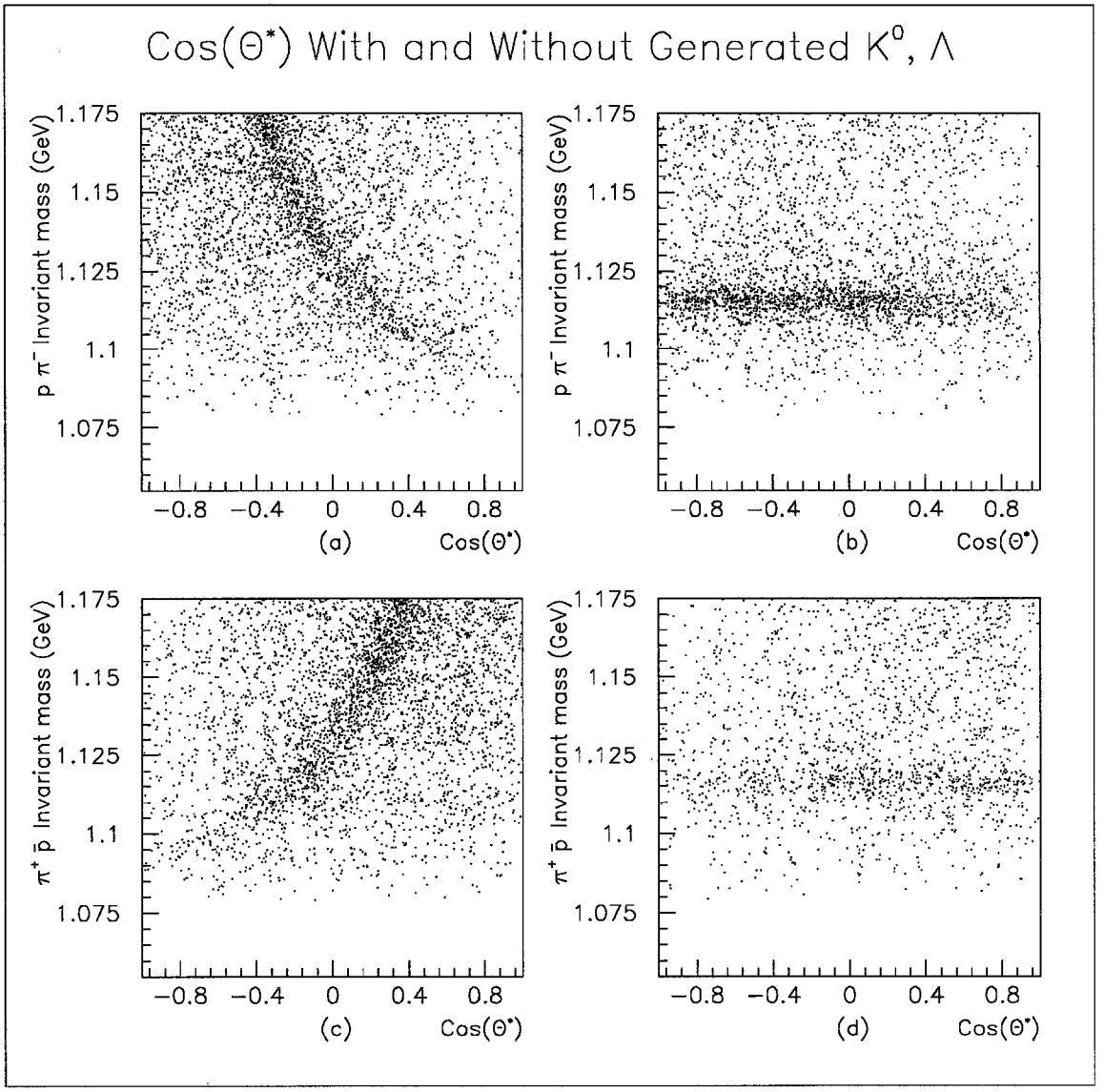

Figure 5.14: $p\pi^-$ and $\bar{p}\pi^+$ Invariant mass versus CosΘ^* with K^0 or Λ and $\bar{\Lambda}$ removed from the sample. When Λ's and $\bar{\Lambda}$'s are removed the K^0 contamination to the (a) Λ and (c) $\bar{\Lambda}$ samples can be clearly seen as an arc. When K^0's are removed from the (b) Λ and (c) $\bar{\Lambda}$ samples an enchancement at the Λ mass surrounded by a relatively uniform background can be seen.

versus Cos(Θ^*) and the $\bar{p}\pi^+$ invariant mass versus cos(Θ^*) under Λ and $\bar{\Lambda}$ hypotheses. Both plots show an enhancement at the Λ or $\bar{\Lambda}$ masses as well as an arc due to misreconstructed K^0's which merges into the mass bands around cos(Θ^*) equal to zero.

Kaon contamination of the Λ and $\bar{\Lambda}$ samples were also studied using the Monte Carlo. Figure 5.14 shows the $p\pi^-$ and $\bar{p}\pi^+$ reconstructed invariant mass distributions as a function of cosΘ^*. In (a) and (c) we have excluded generated Λ's and $\bar{\Lambda}$'s from the sample. The arc extending from the high mass region is due to misidentified K^0 contamination in the sample. Again this contamination makes the task of counting Λ's and $\bar{\Lambda}$'s in the signal region more difficult.

For the Λ's and $\bar{\Lambda}$'s the cosθ^* cut was more difficult to apply than in the case of the K^0's. The problem is that when a simple cut in cosθ^* is made as in the case of the K^0's, a large portion of the sample is lost. A different cut was used. The $p\pi^-$ invariant mass distribution was plotted versus the $\pi^+\pi^-$ invariant mass (see figure 5.15.) This plot clearly shows where the ambiguity exists. It was decided to require that the $\pi^+\pi^-$ invariant mass be less than 0.477 GeV for the Λ or $\bar{\Lambda}$ reconstruction.

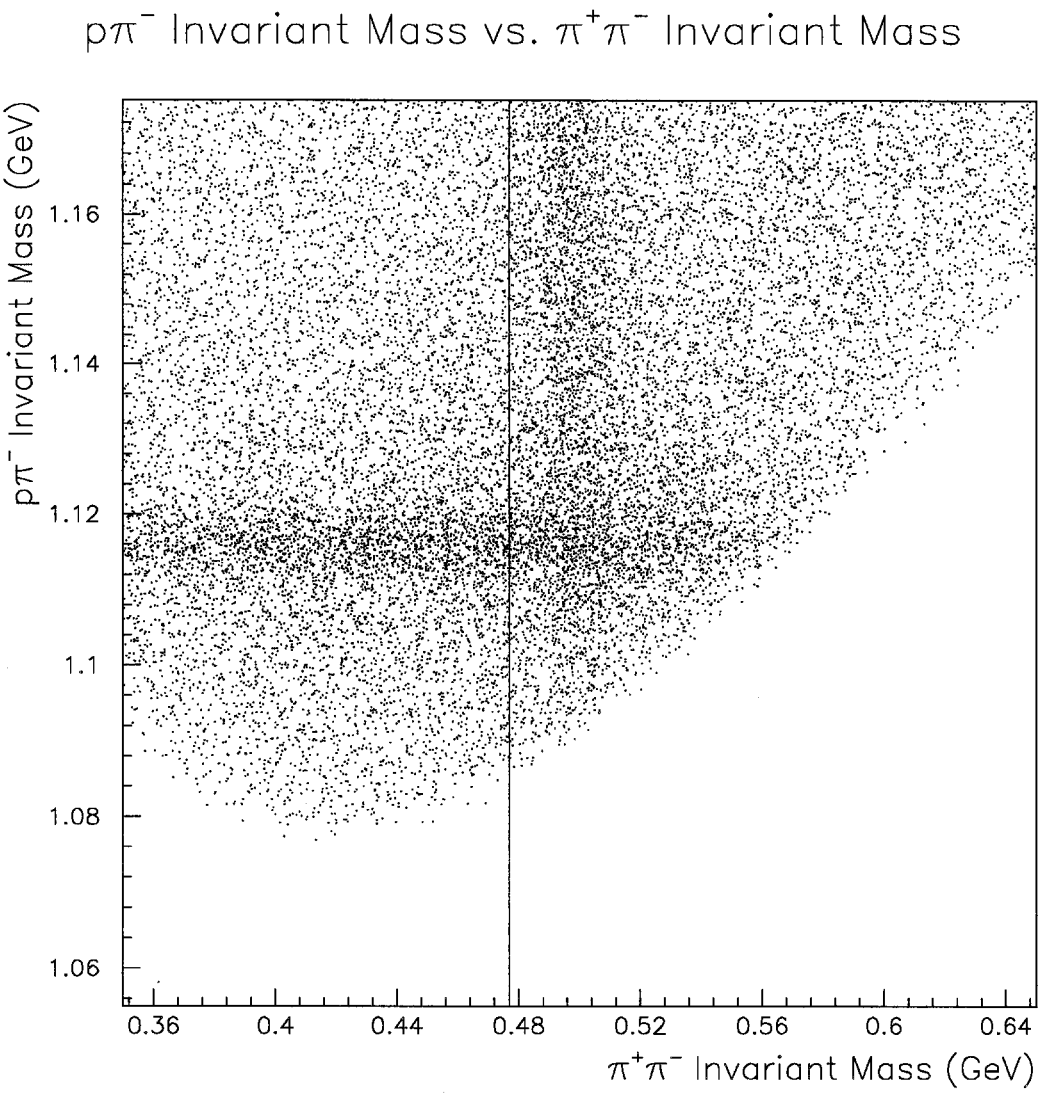

Figure 5.15: The invariant masses formed by taking two tracks under the $\pi^+\pi^-$ and $p\pi^-$ hypotheses. The region of ambiguity exists at the crossing of the two mass bands. It was required that the candidate Λ decay tracks, when interpreted as a $\pi^+\pi^-$, have an invariant mass of less than 0.477 GeV. A similar cut was made for the $\bar{\Lambda}$'s.

5.4 Identification Of The Trigger Particle

The aim of this analysis was to study the properties of strange particles in the recoil jets in π^0 and direct photon triggered events. The following cuts were used to define π^0's and single photons:

- Single local high trigger fired in octant of EMLAC where π^0 or single photon was reconstructed.
- P_T of π^0 or single photon $\geq$ 4.0 GeV.
- LAC Fiducial cuts
    1. 22.7cm $\leq$ Radius of shower $\leq$ 149.5 cm
    2. ϕ position $\geq$ 2 strips away from a quadrant or octant boundary
- E_{front}/E_{total} must be $\geq$ 0.2 for each photon Where E_{front} is the energy in the front section of the electromagnetic calorimeter.
- Muon bremsstrahlung cuts
    1. directionality (δ_r)
        (a) $\delta_r \leq 0.2$ if R $\leq$ 40 cm. Where R is the distance from the beamline to the position of the shower.
        (b) $\delta_r \leq 0.0048 \times$ R, if R $\geq$ 40 cm.

2. Veto wall cut = (upstream VW)⊗[(Downstream VW1)⊕(Downstream VW2)]

- $\frac{AwaysidePT}{TriggerParticlePT} \geq 30\%$
- π^0 signal definition
  1. Two photon asymmetry ≤ 0.75
  2. 100 MeV $\leq M_{\gamma\gamma} \leq$ 180 MeV π^0 mass band
  3. 80-100 MeV and 190-210 MeV side band region for $P_T \leq 7$ GeV
  4. 90-100 MeV and 190-220 MeV side band region for $P_T \geq 7$ GeV
- Distance from direct photon candidate to nearest charged track ≥ 1.5 c.m.

These cuts on the data will be described in each of the following sections.

5.4.1 EMLAC Fiducial Volume

In order to reconstruct a π^0, the EMLAC had to first reconstruct the two candidate photons. In order to insure accurate energy and position measurements of the photons it was necessary to add some constraints on the photon coordinates. The energy and position resolution near the edges of the calorimeter were degraded since part of the showers would occur in the uninstrumented regions. In order to avoid this problem the following fiducial cuts were imposed on the reconstructed photons:

- The photon position must be at least 2 R strips away from the inner radius of the octant.
- The photon position must be at least 2 R strips away from the outer radius of the 235th R strip.
- The photon position must be at least 2 R strips away from the octant and quadrant ϕ boundary

5.4.2 Hadron Rejection

E706 took several steps in order to reject charged and neutral hadrons masquerading as photons in the calorimeter. First, the EMLAC was built with a front and a back section capable independent readout. This enabled us to take advantage of the fact that hadrons tend to shower later and so leave fractionally less of their energy in the front part of the EMLAC. In contrast, an electromagnetic shower tends to deposit most of its energy in the first few layers in the EMLAC. Therefore by looking at the ratio $\frac{E_{front}}{E_{total}}$ which is the ratio of the energy deposited in the front section of the EMLAC to the total energy deposited in both sections, we can differentiate between an electromagnetic shower and a hadronic one. Figure 5.16 shows typical $\frac{E_{front}}{E_{total}}$ distributions. The peak at high values of $\frac{E_{front}}{E_{total}}$ is due to electromagnetic showers. $\frac{E_{front}}{E_{total}}$ was required to be greater than 0.2 for the electromagnetic shower definition.

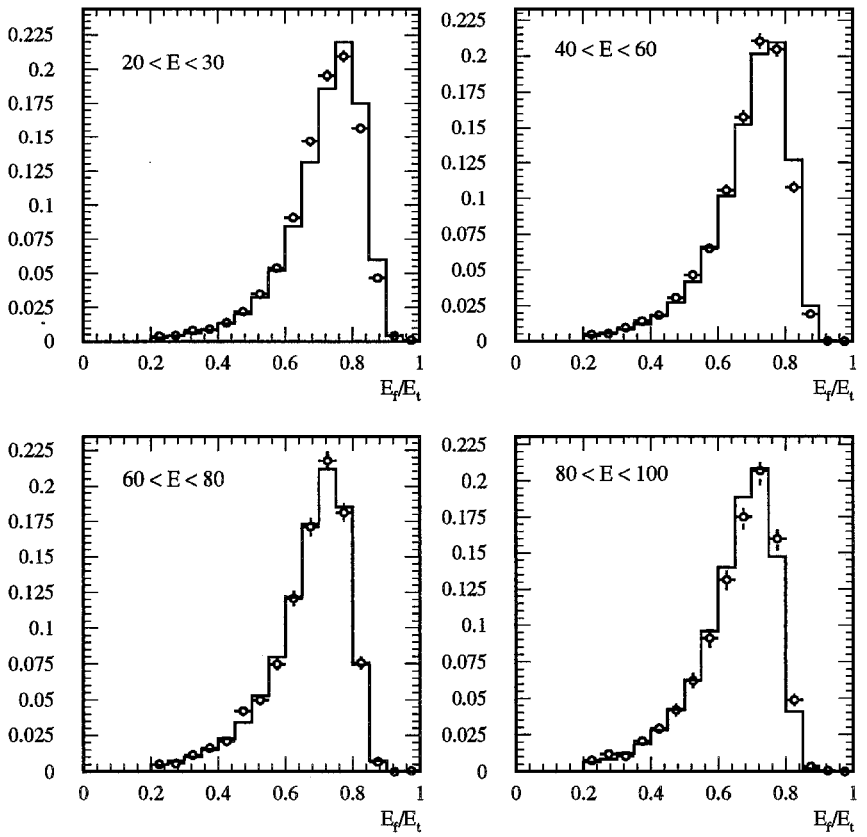

Figure 5.16: $\frac{E_{front}}{E_{total}}$ distributions for different shower energy bins. The histogram is the data while the points are from the E706 Monte Carlo. The distribution has been cut at 0.2.

5.4.3 Background Due To Muon Bremsstrahlung

The π^- secondary beam was often accompanied by a halo of muons from the primary production target. These muons were displaced from the beam axis and could interact in the LAC and produce bremsstrahlung photons. Because of the transverse displacement of these muons the apparent P_T of the bremsstrahlung photons were large. Since E706 triggered on high P_T electromagnetic showers in the EMLAC many of our events would have been due to muons if we had not taken several precautions.

The first precaution taken was an online veto wall requirement. The trigger logic rejected events in which there was a coincidence in signals from the upstream veto and either of the two downstream veto quadrants which shadowed the triggering octant. The veto walls were mounted such that a particle coming from the primary vertex could not pass through them. The veto wall signal had to occur within ± 75 nanoseconds of the interaction time. Due to inefficiencies in the veto walls, gaps between the scintillation counters, and dead time some muons escaped online detection.

Because of this fact an offline veto wall cut was also used. For each quadrant of the EMLAC, if the logical expression VW = (VW1+VW2)×VW3 was true then the event was cut. The logicals VW1, VW2 and VW3 were true if there was a signal from the corresponding veto wall within a ± 20 ns time window. The logical OR of

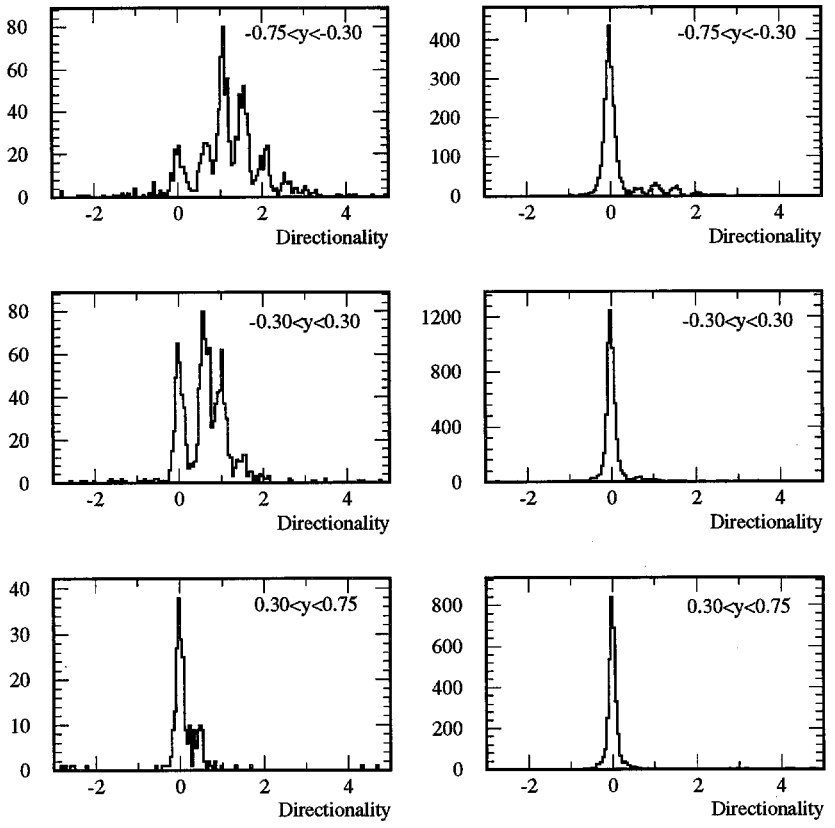

Figure 5.17: Photon directionality histograms for different rapidity ranges. Histograms on the left *require* the offline veto wall signal while those on the right are binned with the offline veto wall cut invoked.

the VWs was formed in a 300 ns wide window centered around the interaction.

Another anti-muon cut was the cut on directionality defined as $\delta_R \equiv R_{front} - \frac{Z_{LAC}^{front}}{Z_{LAC}^{back}} R_{back}$. In this definition, R_{front} is the radial position of the shower in the front section of the EMLAC while R_{back} is the radial position in the back section. Z_{front} is the z position of the front section of the EMLAC and Z_{back} is the z position of the back section. If a shower is due to a photon which originates in the target region then it will have a directionality near zero. However a shower due to a muon bremsstrahlung would yield larger values of directionality since $R_{front} \sim R_{back}$. Since muons tend to be displaced from the beam axis by several centimeters, we can clearly resolve the directionality distributions due to muons and those due to photons originating in the target region. Figure 5.17 shows the effect of the offline veto wall cut. The peak near zero is clearly seen along with other peaks due to muons displaced from the beam axis.

In addition to the offline veto wall cut and the directionality cut, we also applied a balanced P_T cut. The idea here is that in a typical hard scatter event, the P_T on the trigger side and on the awayside must balance. However, if an event was triggered by a muon induced shower in the LAC rather than from a high P_T interaction, then we would expect an event with little very little P_T deposited on the recoil side. Figure 5.18 shows the effect of applying the offline veto wall cut to the balanced P_T distribution. The ratio of away-side P_T with respect to π^0 P_T is shown requiring the offline wall cut and with the cut applied.

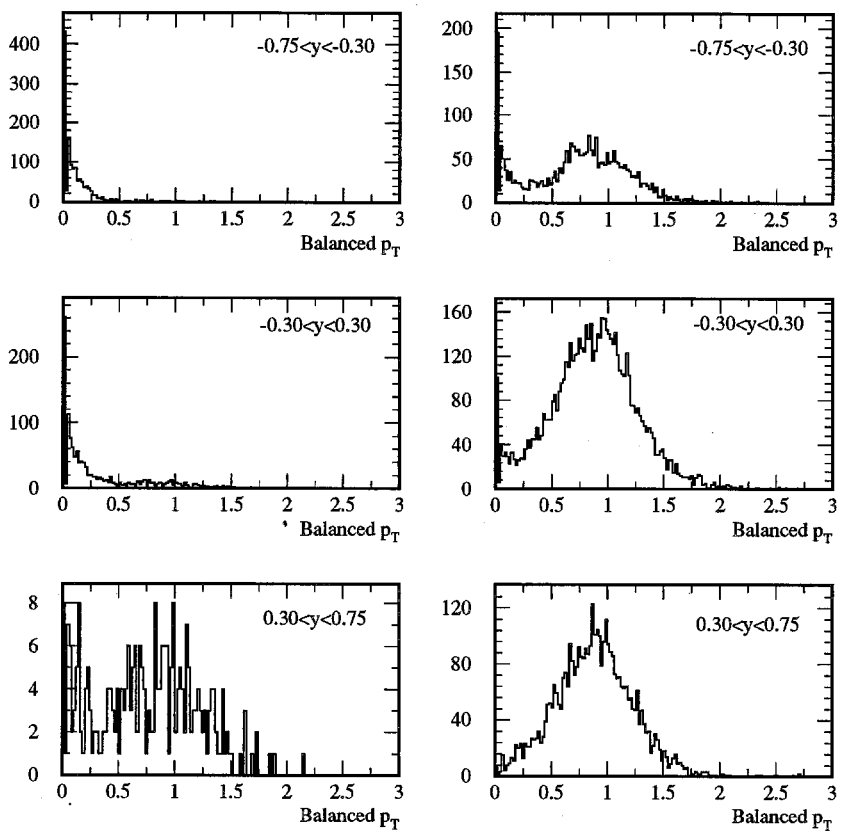

Figure 5.18: Balanced P_T histograms for reconstructed π^0's with $P_T \geq 5.5$ GeV. On the left side are events requiring the offline veto wall signal. On the right, events with the offline veto wall cut applied.

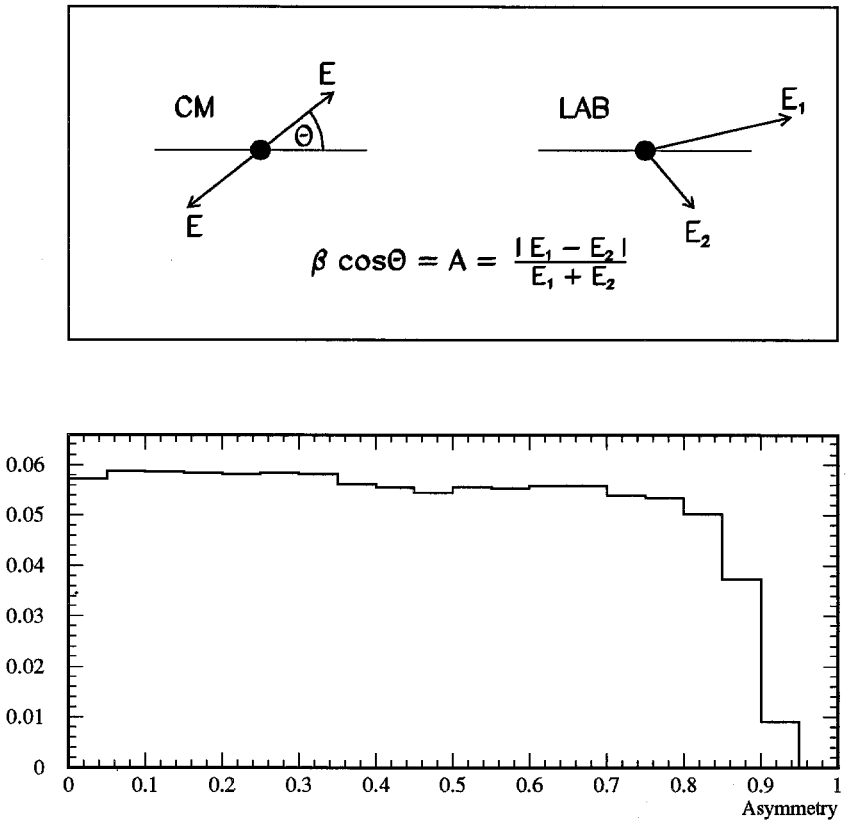

Figure 5.19: Two photon energy asymmetry definition (top) and distribution in data (bottom) for π^0's

5.4.4 Two Photon Asymmetry

Since the π^0 is a spin zero particle, we don't expect the cross section of the decay $\pi^0 \rightarrow \gamma\gamma$ to depend on the angular distribution of the decay photons. There is relationship between the energy assymetry, A = $\frac{\|E_1 - E_2\|}{E_1 + E_2}$, and the angle, θ, between one of the photons and the π^0 momentum vector. The relationship, which can be

derived using kinematic arguments, is A = βcosΘ. In the rest frame of the π^0 the two photons will have an equal amount of energy. However, when they are boosted into the lab system, their energies generally can be different. This situation can cause difficulties in the reconstruction of the π^0 from the photon energies. If one of the photons has too little energy or is ejected from the π^0 at an angle such that it misses the EMLAC then it will not be reconstructed. This situation becomes an inefficiency in the reconstruction of the π^0 and contributes to the background of the direct photon. The definition of asymmetry as well as an asymmetry distribution is shown in figure 5.19. For this study we only looked at π^0's with asymmetry less than 0.75.

Figures 5.20, 5.21 and 5.22 show histograms of the invariant masses under the different hypotheses after the cuts described above.

5.5 The E706 Monte Carlo

To motivate some of the cuts to the data and to compare results with theoretical expectations, extensive use of the E706 Monte Carlo was made. This Monte Carlo used HERWIG as the event generator and GEANT was used to simulate the response of the spectrometer. The details of the E706 Monte Carlo can be found elsewhere [20, 24] Only the details relevant for this analysis will be discussed here.

A histogram of the reconstructed $\pi^+\pi^-$ invariant mass from the Monte Carlo

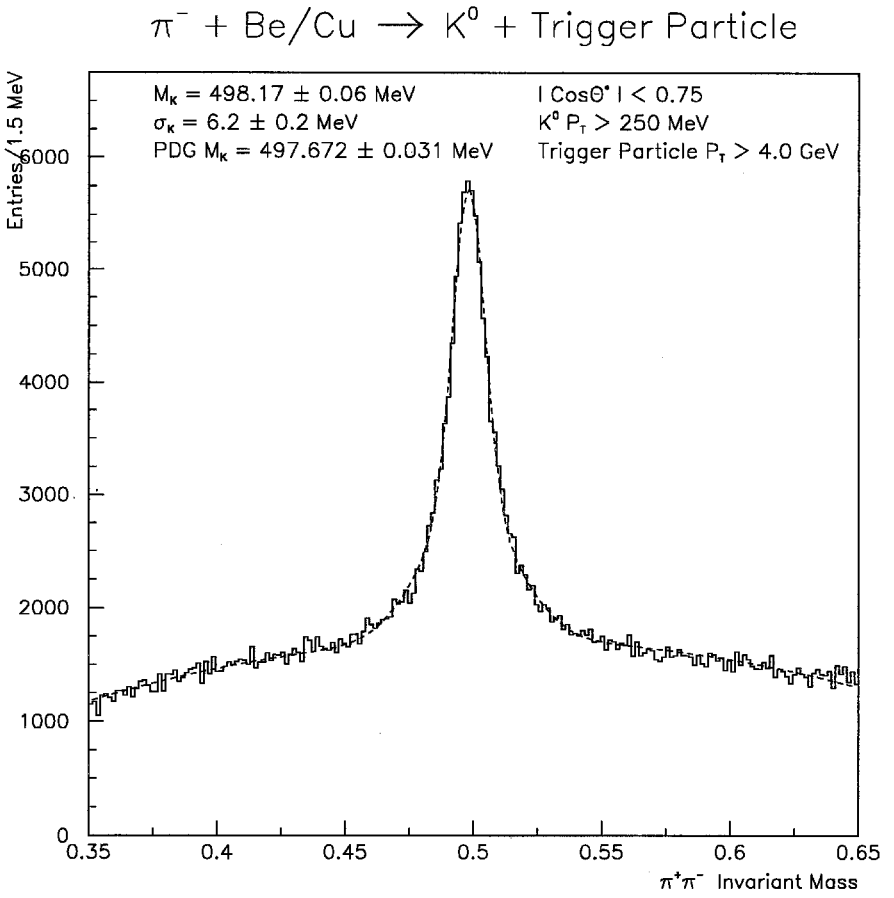

Figure 5.20: $\pi^+\pi^-$ invariant mass after applying the trigger P_T cut, the cosΘ^* cut, the requirement that the K^0 have a $P_T > 0.25$ GeV, and requiring the reconstruction of both the trigger and awayside jet in the event. In addition a single local high trigger was required as well as an $E_{Front}/E_{Total} > 0.2$. The muon veto requirements discussed above were also applied. No attempt was made to distinquish the origin of the photons at this point (i.e. whether they were direct photons or from π^0 decays). Based on the fitted curve shown it is estimated that we have reconstructed 64,000 K^0's.

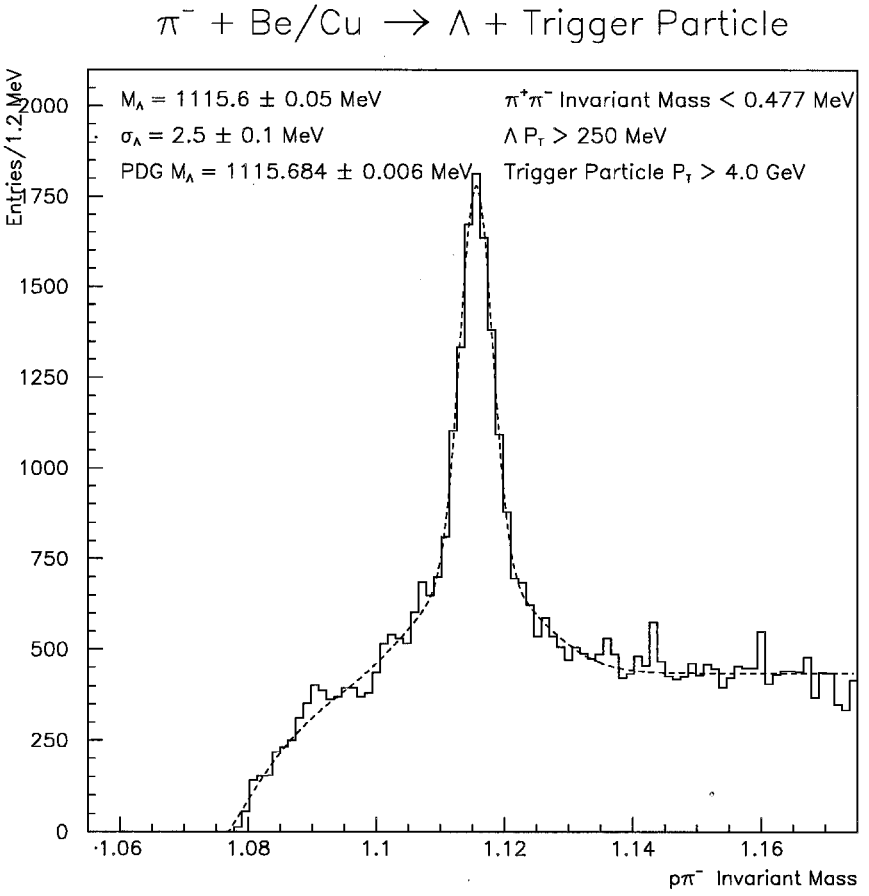

Figure 5.21: p π^- invariant mass after applying the trigger P_T cut, the $\pi^+\pi^-$ invariant mass cut, the requirement that $\Lambda P_T > 0.25$ GeV, and requiring the reconstruction of both the trigger and awayside jet in the event. In addition a single local high trigger was required as well as an $E_{Front}/E_{Total} > 0.2$. The muon veto requirements discussed above were also applied. No attempt was made to reconstruct π^0's at this stage. Based on the shown fitted curve it is estimated that we have reconstructed 11,000 Λ's.

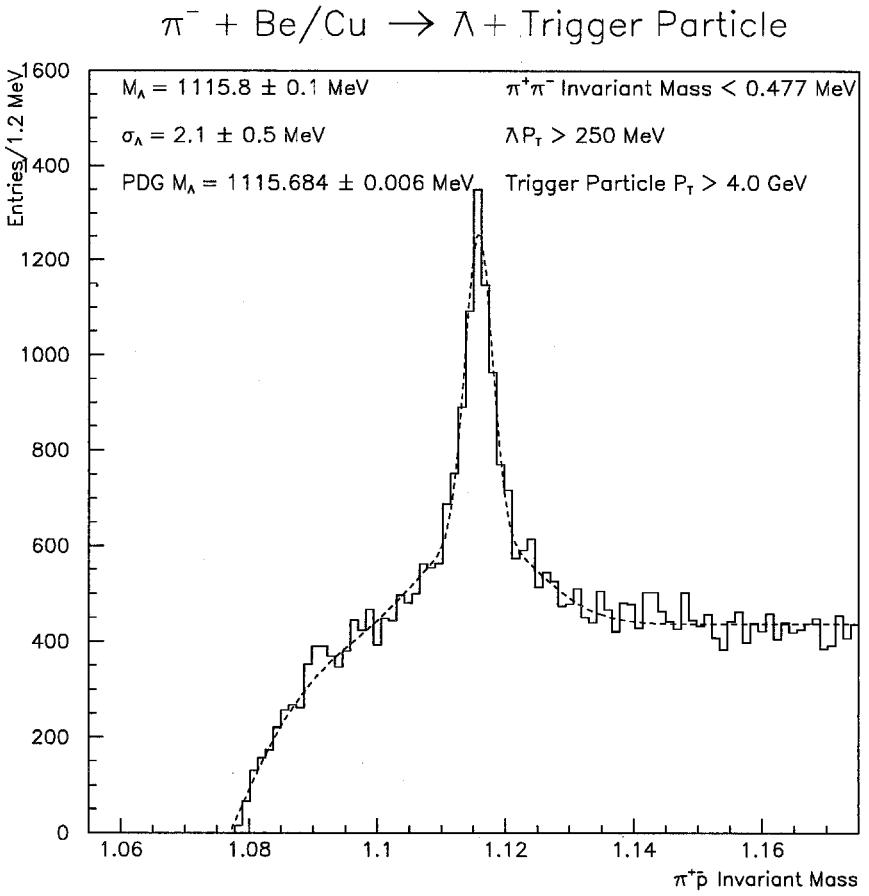

Figure 5.22: $\bar{p}\pi^+$ invariant mass after applying the trigger P_T cut, the $\pi^+\pi^-$ invariant mass cut, the requirement that the $\bar{\Lambda}$ have $P_T > 0.25$ GeV, and requiring the reconstruction of both the trigger and awayside jet in the event. In addition a single local high trigger was required as well as an $E_{Front}/E_{Total} > 0.2$. The muon veto requirements discussed above were also applied. No attempt was made to reconstruct π^0's at this stage. Based on the fitted curve shown it is estimated that we have reconstructed 6,000 $\bar{\Lambda}$'s.

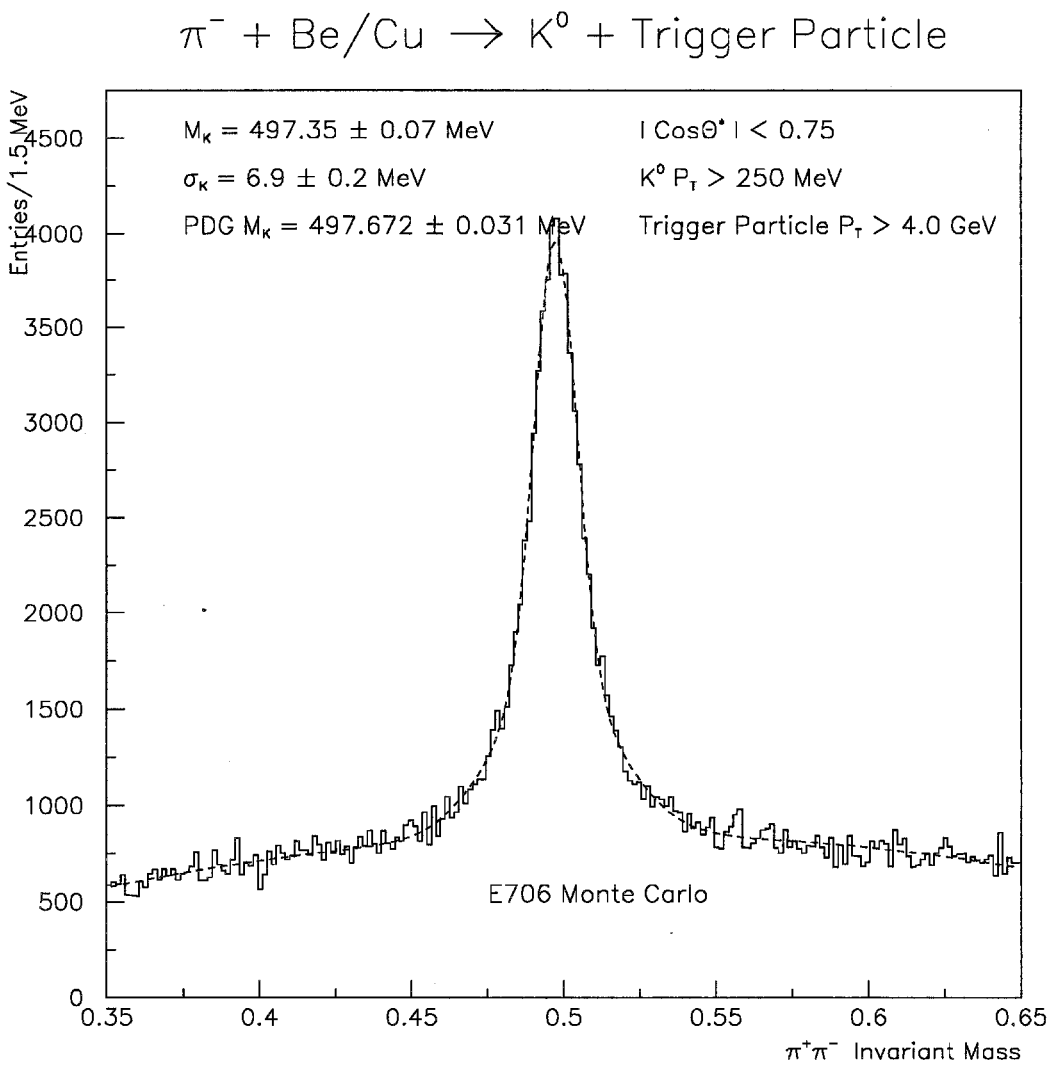

Figure 5.23: $\pi^+\ \pi^-$ invariant mass in Monte Carlo.

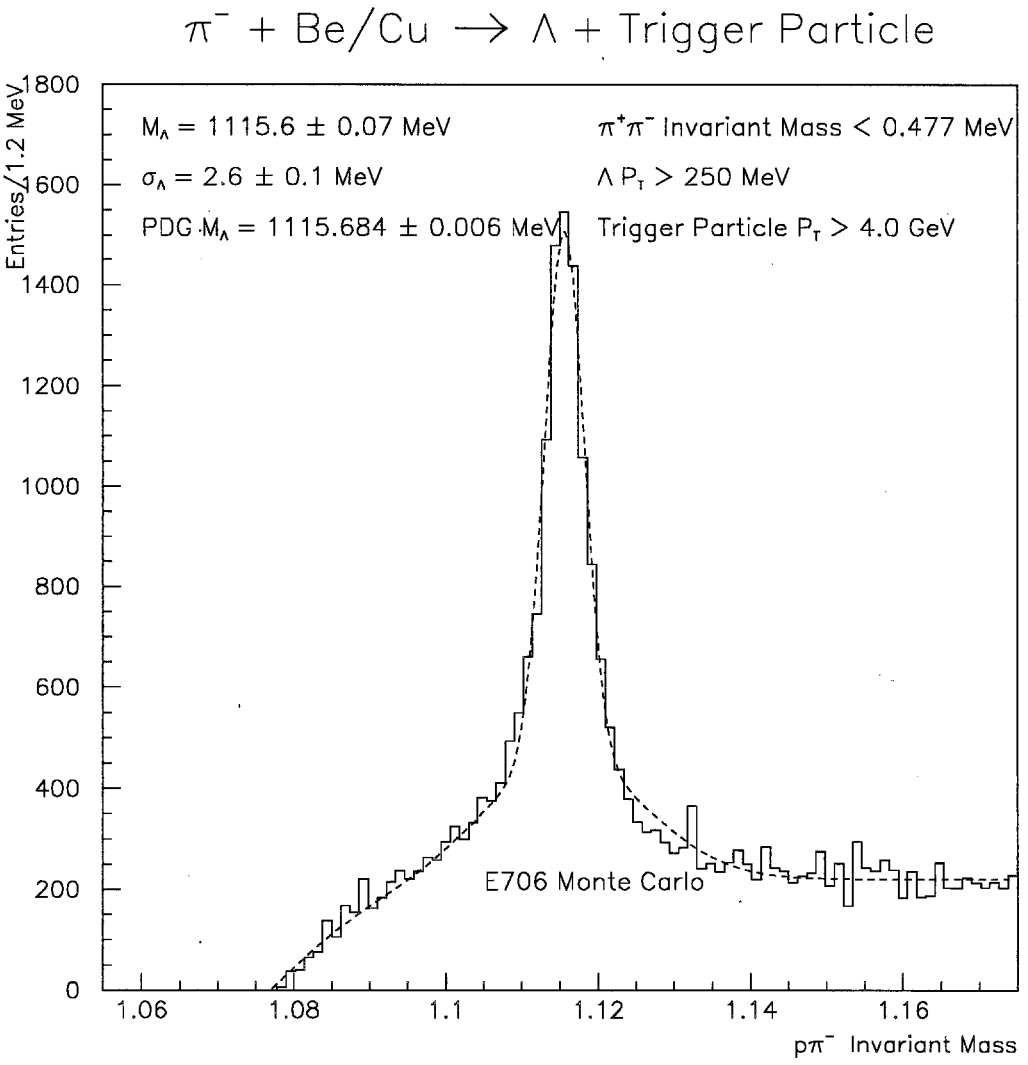

Figure 5.24: p π^- invariant mass in Monte Carlo.

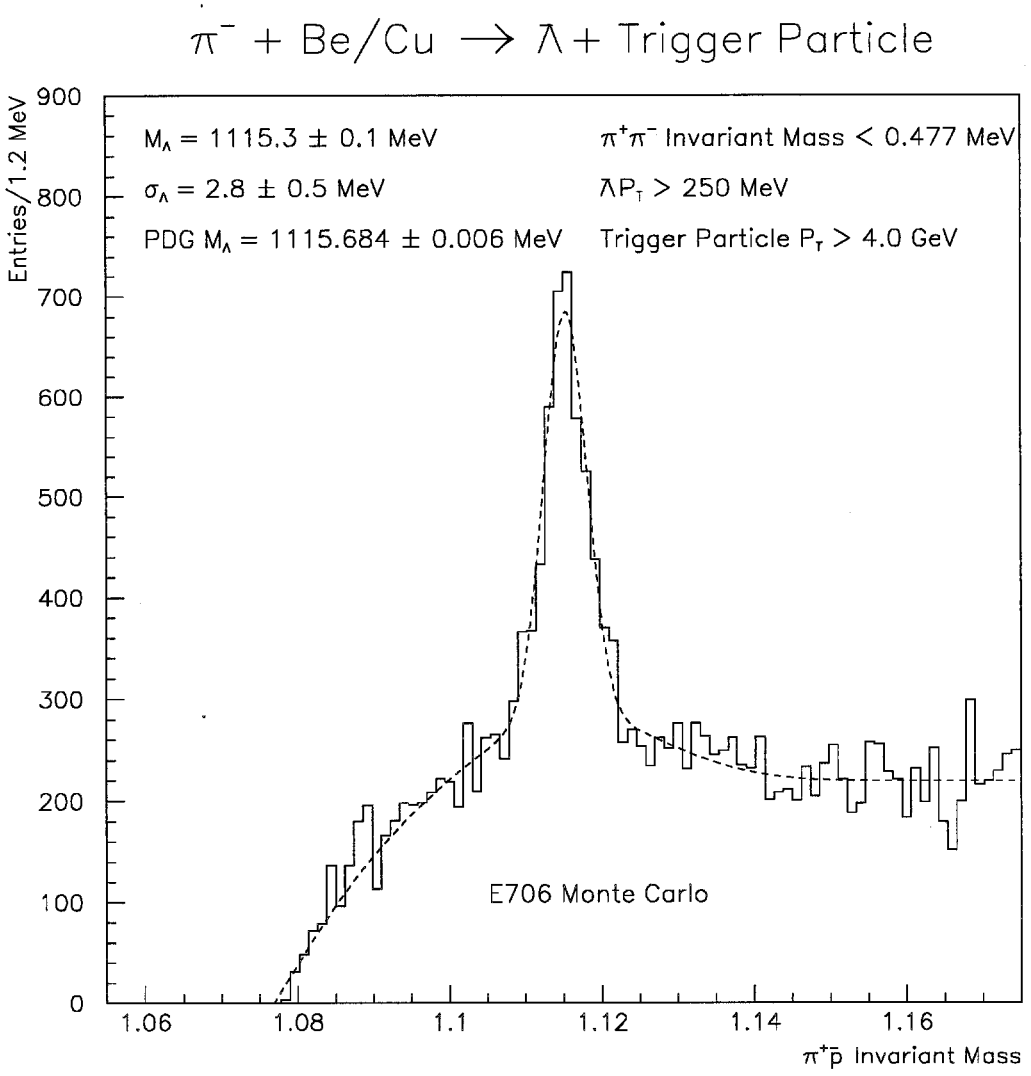

Figure 5.25: $\bar{p}\pi^+$ invariant mass in Monte Carlo.

is shown in figure 5.23. Figure 5.24 and figure 5.25 show the Monte Carlo mass distributions for the Λ and $\bar{\Lambda}$. A fit of the peak region shows that the Monte Carlo does a good job of modeling the data. (Compare with figures 5.20, 5.21, and 5.22.)

5.6 The Strange Sample

Using the cut sample described above, the following was determined:

- Whether the trigger was due to a single photon or a π^0 decay.
- Whether the strange particle was reconstructed in the awayside jet.

This was the sample in which the comparisons of the following chapter were made. Figures 5.26, 5.27, and 5.28 show the final invariant mass distributions.

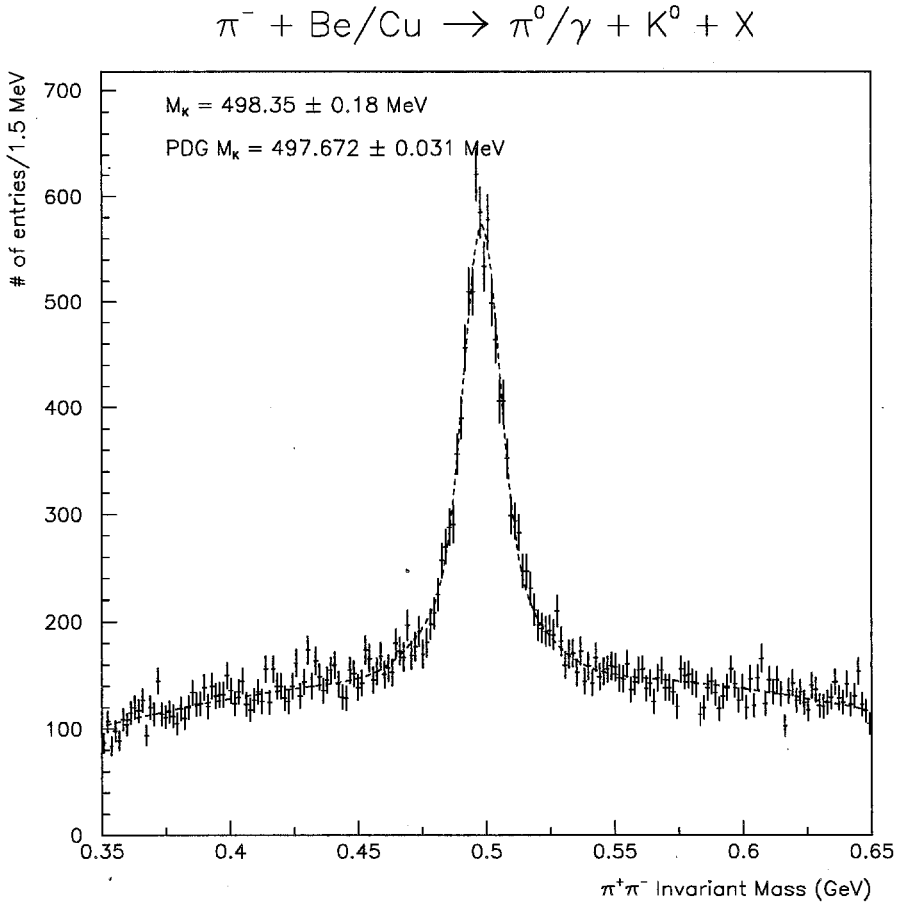

Figure 5.26: π^+ π^- invariant mass in the awayside jet. This plot contains all of the above listed cuts including the criteria that the K^0 must be part of the awayside jet and a π^0 or single photon trigger with $P_T > 4.0$ GeV must be reconstructed. This represents the sample that is used for the results in chapter 6.

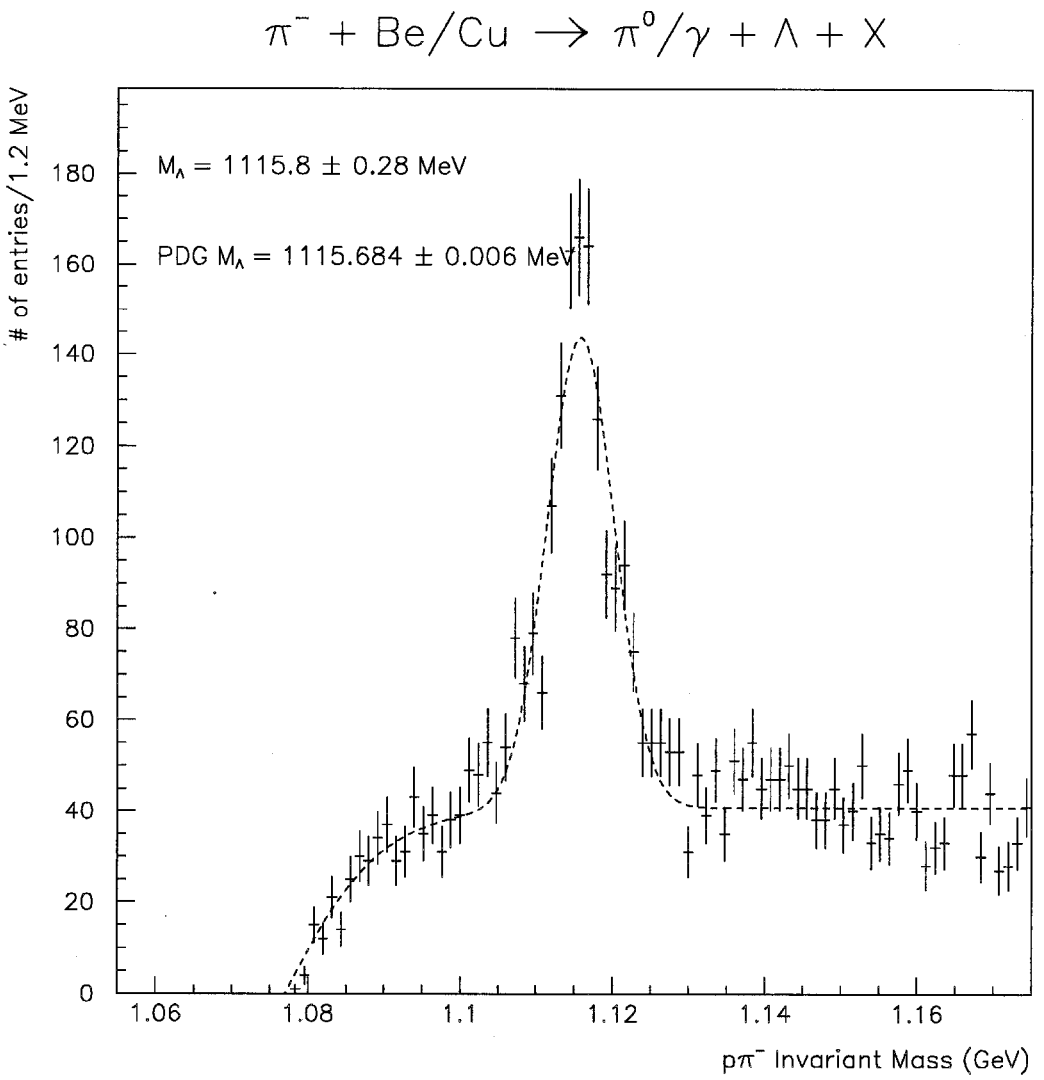

Figure 5.27: p π^- invariant mass in the awayside jet. This plot contains all of the above listed cuts including the criteria that the Λ must be reconstructed as part of the awayside jet and a π^0 or single photon trigger with $P_T > 4.0$ GeV must be reconstructed. This represents the sample that is used for the results in chapter 6.

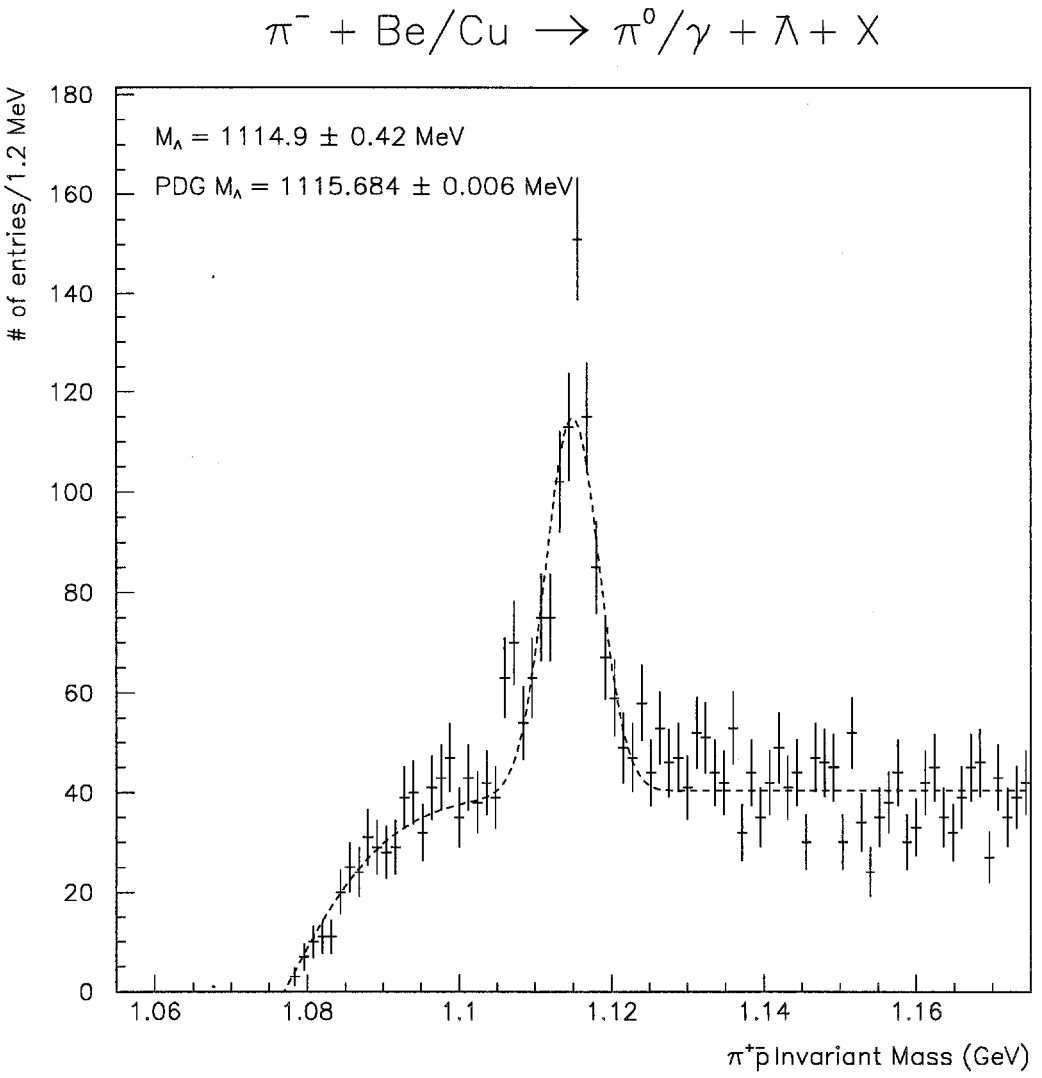

Figure 5.28: $\bar{p}\pi^+$ invariant mass in the awayside jet. This plot contains all of the above listed cuts including the criteria that the Λ must be reconstructed as part of the awayside jet and a π^0 or single photon trigger with $P_T > 4.0$ GeV must be reconstructed. This represents the sample that is used for the results in chapter 6.

Chapter 6

Results

The goal of this study was to compare the properties of neutral strange particles in away side jets opposite direct photon or π^0 triggers. Direct photon interactions gave us a unique opportunity to study quark and gluon initiated jets in our sample. In the lowest order QCD approximation, there are only two diagrams which contribute to direct photon production. The contribution due to each of these diagrams varies with beam particle type and direct photon P_T. The P_T dependence of the relative fractions of the Annihilation and Compton diagrams to the total is shown in figure 1.5.

In QCD, one expects a difference between quark and gluon jets because of the greater color charge carried by the gluon. Qualitatively, it is expected that gluon jets would have higher multiplicities, softer fragmentation, and be broader in angle

than quark jets. This thesis seeks to study whether these differences include a predominance of strange particles in either type of jet. Further, a comparison is made for mesons (K^0) and baryons (Λ) separately, and baryons and anti-baryons. One might expect, since strange quarks must come from the sea i.e. from gluon splitting, that gluon jets would show a harder strange particle fragmentation function than quark jets. This is because the strange quark-antiquark pair could be created sooner in the fragmentation process in the gluon initiated jet. The quark would first have to emit a gluon before it could subsequently split into a $s\bar{s}$ pair.

Comparisons were made between direct photon and π^0 triggered events as a function of trigger particle P_T and the momentum fraction, z, of the strange particle with respect to the away-side jet. The following reactions were studied:

- $\pi^- + p \rightarrow \pi^0 + K^0 + X$
- $\pi^- + p \rightarrow \pi^0 + \Lambda + X$
- $\pi^- + p \rightarrow \pi^0 + \bar{\Lambda} + X$
- $\pi^- + p \rightarrow \gamma + K^0 + X$
- $\pi^- + p \rightarrow \gamma + \Lambda + X$
- $\pi^- + p \rightarrow \gamma + \bar{\Lambda} + X$

6.1 Jet Finding Algorithm

The algorithm used to find jets was the cone algorithm. The implementation of this algorithm involved an iterative approach:

- An initial jet direction was defined
- This axis was used as a reference to construct the quantities $\Delta\eta$ and $\Delta\phi$ for each track
- It was decided whether a track belonged in the jet by requiring $\Delta R = \sqrt{(\Delta\eta)^2 + (\Delta\phi)^2} \leq 1.0$
- The momenta of tracks consistent with $\Delta R \leq 1.0$ were summed. The total summed momentum was used to define a new jet axis.
- The procedure was repeated using the new jet axis until no tracks were added or removed from the jet.

6.1.1 Initial Jet Directions

An initial jet direction was constructed as a seed direction for the cone algorithm. The decision as to whether a track belonged to a jet was made using this seed direction as a reference for the first iteration. Both the trigger jet and the away side jet were reconstructed for this analysis.

Trigger Jet Direction

The trigger particle direction was defined as the direction of a π^0 or single photon with $P_T \geq 4.0$ GeV. The trigger particle had to satisfy all of the criteria for a π^0 or direct photon discussed in chapter 5. This direction was used as a seed for the trigger jet finding.

Recoil Jet Direction

The seed direction on the away side was defined by the highest P_T particle having a $\Delta\phi$ with respect to the trigger particle of ≥ 1.75 radians measured in the P_T plane. The seed direction for the away side jet was called the leading particle direction. The leading particle had to have a $P_T \geq 500$ MeV. Charged or neutral particles were acceptable as leading particles. For photons there were the following additional requirements:

- A leading photon had to have energy in the range 5 GeV $\leq$ E $\leq$ 250 GeV.
- A leading photon couldn't have matching charged tracks within 1.5 cm at the face of the EMLAC.

6.1.2 Jet Track Requirements

The tracks used in the reconstruction of the trigger and away side jets had to meet the following criteria:

- Each charged track had to have $P_T \geq 0.25$ GeV.
- Each charged track had to have pseudorapidity $\mid \eta \mid \leq 1.75$
- Each charged track had to have a y view impact parameter at the primary vertex of ≤ 1.5 cm.

Only the leading particle was allowed to be neutral in the jet algorithm.

6.1.3 Trigger And Recoil Jet Requirements

The reconstructed trigger and away side jets had to satisfy the following criteria:

- The reconstructed P_T of the away side jet had to be $\geq 30\%$ of the P_T of the trigger particle.
- The azimuthal angle between the away side jet axis and the trigger particle had to be ≥ 1.75 radians.
- The rapidity of the away side jet had to be $-1.0 \leq \eta_{jet} \leq 1.0$. This requirement minimized the overlap from the beam and target jets.

6.2 Inclusion Of Strange Particles In Jet

The algorithm for including strange particles in the jet calculations was defined as follows:

- The strange particles candidates in the event were reconstructed according to the strange particle definitions in chapter 5.
- The strange particle candidates were included in the track array for each π^0 or single γ capable of triggering the event,
- The jet reconstruction was done once for each strange particle candidate. The trigger and away side jet four vectors were calculated.

The strange particles were included in the jet one by one. That is, for each candidate strange particle which satified the track cuts, the decay tracks would be removed from the jet and the neutral strange track would be added in its place. This allowed an invariant mass histogram to be reconstructed for each value of z (defined in section 6.3) or P_T. In this way, the background distribution for each value was fit and subtracted from the signal region.

6.3 Definition Of Z

One of the variables useful in the study of parton fragmentation to jets is the fractional momentum carried by the hadron in the direction of the jet:

$$P_L \equiv \vec{P_i} \cdot \frac{\vec{P_{jet}}}{|\vec{P_{jet}}|} \tag{6.1}$$

$$z = \frac{P_L}{|\vec{P_{jet}}|} \times \frac{P_T(awayside)}{P_T(trigger)} \tag{6.2}$$

This equation describes what fraction of the particle's momentum is in the direction of the away side jet. Since the jet direction is defined by the sum of the momenta of all reconstructed tracks in the jet, z tells us how much the jet direction has been determined by the particle. A value of z near one indicates a high probability that the particle is the leading particle in the away side jet.

The z variable is rescaled to the P_T of the trigger particle. This procedure assumes that the effects of intrinsic parton momentum (K_T) are small. The rational for this rescaling is that the trigger side P_T is known more accurately than the awayside P_T.

6.4 Background Subtraction

There were two important forms of background to deal with in this study: The combinatorial background from the reconstruction of secondary vee candidates and the background from misreconstructed π^0's in the direct photon sample.

To remove the combinatorial background, plots of the invariant mass regions were made for each bin of the variable in question. For example, when the fragmentation function for the K^0's was plotted, a $\pi^+\pi^-$ invariant mass histogram was filled for each z bin. The background region was then fit to a second order polynomial. The curve resulting from the fit was used to subtract the background from the bins in the signal region.

What we had left after this procedure was an estimate of the number of K^0's in the bin. However, because we were interested in the fragmentation functions in direct photon triggered events, we had to account for the single photon background. To this end, the π^0 Monte Carlo was put through the same event reconstructor as the data. A certain number of the generated π^0's were reconstructed and therefore eliminated as direct photon candidates. The rest were direct photon candidates provided that they passed the direct photon cuts outlined in chapter 5. The ratio of the number of these candidates to the number of reconstructed π^0's was used to estimate the single gamma contamination in the data due to π^0's that were not reconstructed [20]. The $\frac{\gamma}{\pi}$ ratio was multiplied by the number of reconstructed π^0 in the data. The following formula illustrates the technique:

$$\begin{aligned} N_\gamma^{true} &= N_\gamma^{recon} - N_\gamma^{fake} \\ &= N_\gamma^{recon} - N_{\pi^0}^{recon} \times \frac{N_\gamma^{mc}}{N_{\pi^0}^{mc}}. \end{aligned} \tag{6.3}$$

This technique was used to handle the direct photon background subtraction for the fragmentation functions.

$$\begin{aligned} (dn_{ch}/dz)_\gamma^{true} &= (dn_{ch}/dz)_\gamma^{recon} - (dn_{ch}/dz)_\gamma^{fake} \\ &= (dn_{ch}/dz)_\gamma^{recon} - (dn_{ch}/dz)_{\pi^0}^{recon} \times \frac{(dn_{ch}/dz)_\gamma^{mc}}{(dn_{ch}/dz)_{\pi^0}^{mc}} \end{aligned} \tag{6.4}$$

The same technique was used for the (dn_{ch}/dP_T) distributions. This technique assumes a resonable agreement between the P_T distributions of Data and the

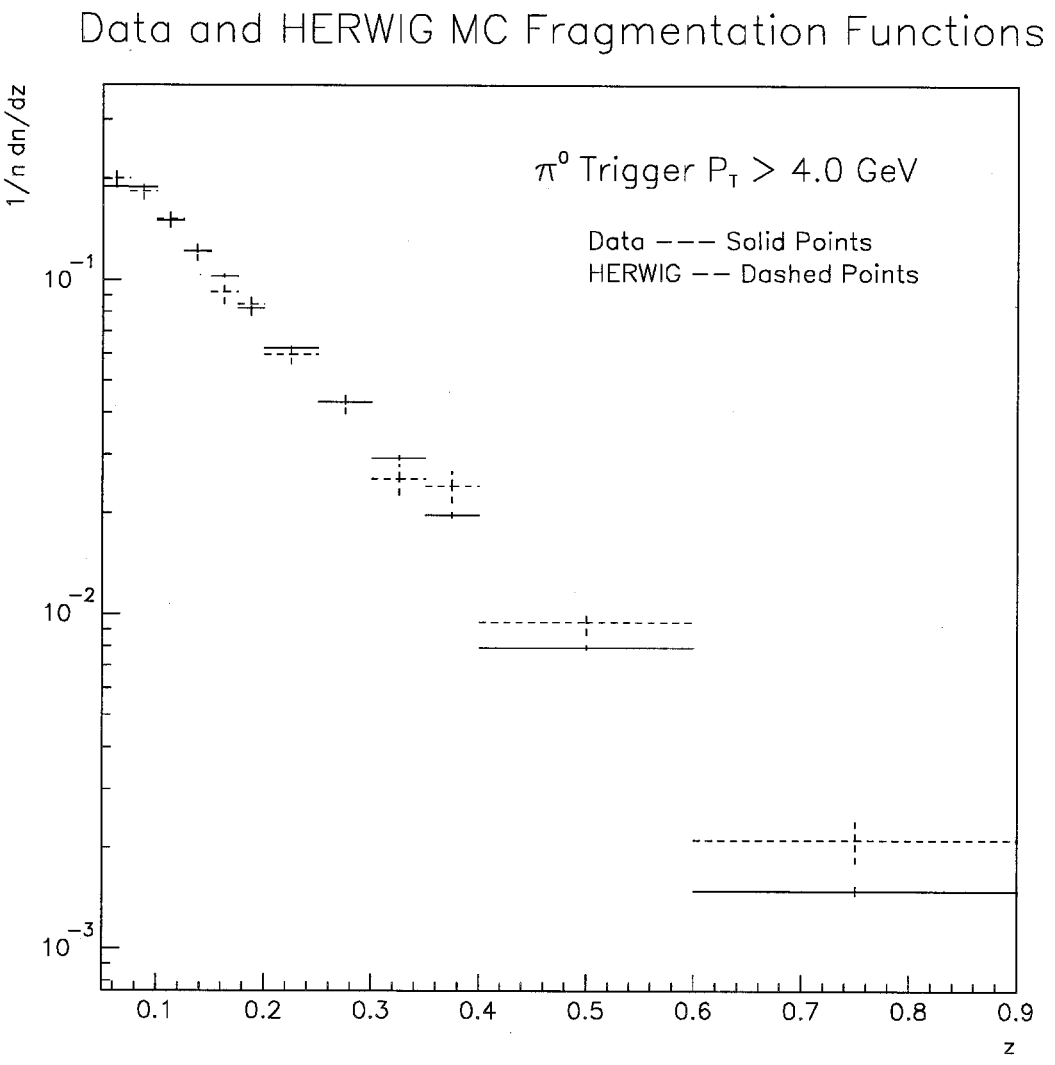

Figure 6.1: Comparison of the fragmentation functions of data and the HERWIG Monte Carlo. The full GEANT detector simulation has been included in the Monte Carlo. The Monte Carlo events were generated with $P_T > 3.0$ GeV. In this comparison, a π^0 trigger with $P_T > 4.0$ GeV was required.

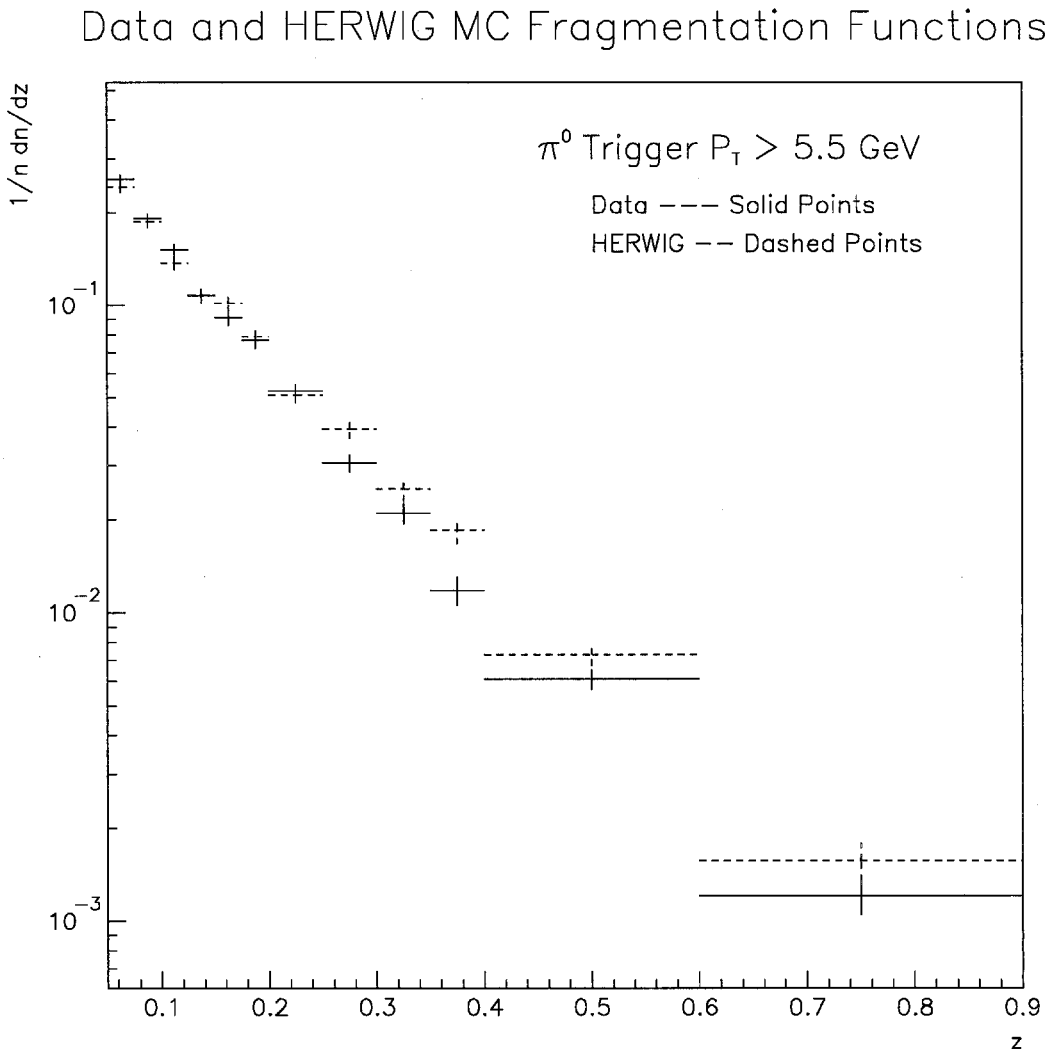

Figure 6.2: Comparison of the fragmentation functions of data and the HERWIG Monte Carlo. The full GEANT detector simulation has been included in the Monte Carlo. The Monte Carlo events were generated with $P_T > 5.0$ GeV. In this comparison, a π^0 trigger with $P_T > 5.5$ GeV was required.

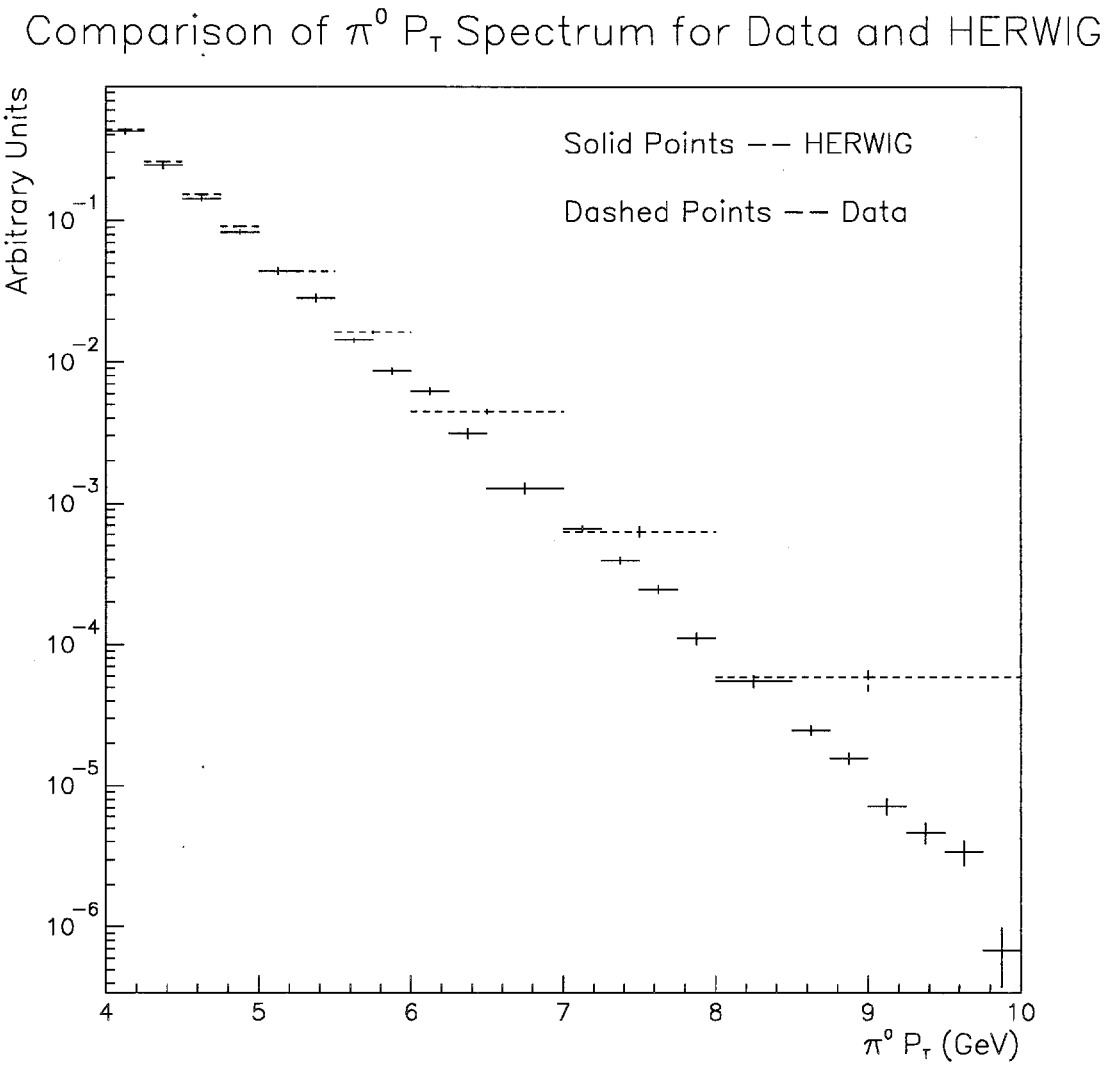

Figure 6.3: Comparison of the P_T spectrums of data and the HERWIG Monte Carlo. The full GEANT detector simulation has been included in the Monte Carlo. The Monte Carlo events were generated with $P_T > 3.0$, 4.0, 5.0, 6.5, and 8.0 GeV. In this comparison, a π^0 trigger with $P_T >$ the generated $P_T + 0.5$ GeV was required.

E706 Monte Carlo. This correction could contribute to systemic errors in the final answers. To investigate the agreement between the E706 Monte Carlo and data figure 6.1 shows a comparison between fragmentation functions from data and from HERWIG Monte Carlo with detector effects included. The Generated P_T starts at 3.0 GeV and only events with π^0 trigger $P_T > 4.0$ GeV are accepted in this comparison. Figure 6.2 shows HERWIG with a P_T threshold of 5.0 GeV in which only events with Trigger $P_T > 5.5$ GeV are accepted. Also shown in the figure is the data with a π^0 trigger $P_T > 5.5$ GeV. Figure 6.3 shows a comparison between the $\pi^0 P_T$ spectrums of the HERWIG Monte Carlo and data. This plot shows that the HERWIG spectrum is softer that the data. This is consistant with the fragmentation comparisons considering the P_T rescaling. These plots are shown without corrections for the various cuts discussed in chapter five as well as any geometric or acceptance considerations.

6.5 Results

The results presented in this section are in the form of ratios plotted versus P_T or z. It was assumed that corrections due to the various cuts discussed in chapter 5 as well as geometric and other corrections would cancel in the ratio. Therefore no corrections to this data have been applied.

All error bars shown on the figures in this section represent statistical errors

only.

6.5.1 HERWIG predictions for K^0 and Λ production vs. P_T

Since it was expected that the fraction of gluon jets in the direct photon triggered sample would increase with photon P_T, it was natural to make comparisons as a function of this variable. The HERWIG [7, 8] Monte Carlo generator was used to compare theoretical predictions with the experimental data from this analysis. The cone algorithm was used to define jets in HERWIG and to determine whether the jets were initiated from gluons or quarks. The results plotted here do not include detector effects. The generated information was put through the cone algorthim, as was the data, with the same cuts and parameters (i.e. cone size, minimum P_T, etc). Figure 6.4 shows the HERWIG prediction for the ratio of the number of K^0 present in gluon jets to the number present in quark jets as a function of P_T. Each bin has been normalized by the the ratio of the total number of gluon jets to the total number of quark jets in that P_T bin. The HERWIG result is consistent with no difference in the ratio as a function of the P_T of the trigger particle. The HERWIG Λ results, also shown in Figure 6.4, are more difficult to interpret. They could be interpreted as having a P_T dependence within a one sigma deviation however more statistics are needed to make a conclusive statement.

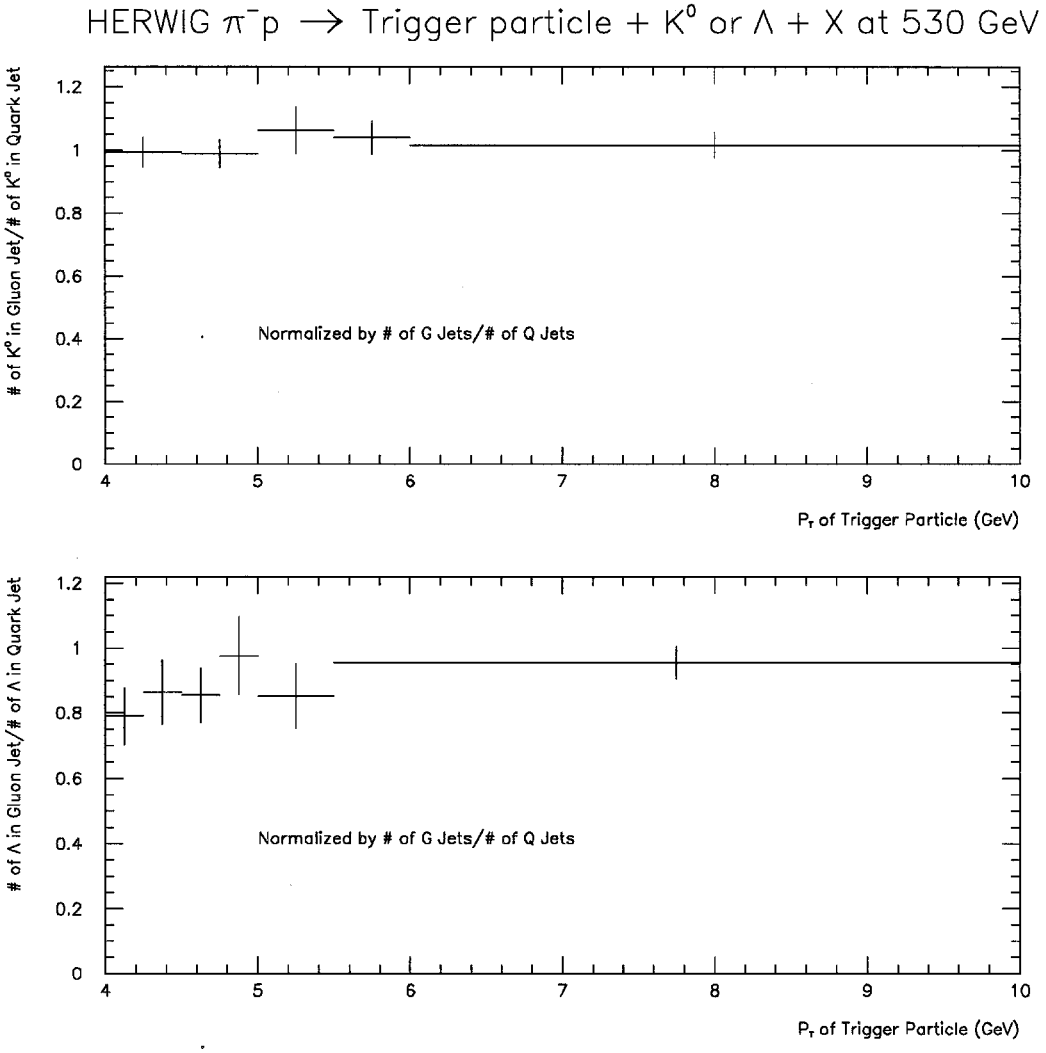

Figure 6.4: TOP: The ratio of the number of K^0's generated in gluon initiated away side jets to the number generated in quark initiated away side jets vs. trigger particle P_T. BOTTOM: The same ratio for Λ's generated in the away side jet. Note: This plot is HERWIG Generated events with detector effects not taken into account.

Bringing the MC study one step closer to what was examined in data, the ratio of direct photon selected events with a K^0 produced in the away side jet to π^0 selected events with a K^0 produced in the away side is shown in figure 6.5. Again, only HERWIG generated information is shown. Detector effects have not been included nor has any strange particle reconstruction been done. The purpose here is to study the ratios at the HERWIG generator level and look for any P_T dependence. Also shown is the same distribution for Λ's. It was expected that at higher trigger particle P_T values, a purer sample of gluon away side jets would be produced in the direct photon sample. Similarly, it was shown [20] that high P_T π^0 triggered events produced a predominantly quark initiated away side jet. Both distributions are consistent with no trigger particle P_T dependence within statistical errors.

6.5.2 K^0's and Λ's reconstructed in the away side jet

To examine this effect in the data, an invariant mass distribution was made for each trigger particle P_T bin for K^0's and Λ's ($\bar{\Lambda}$'s). The distributions contained both signal and background. In order to subtract the background, a signal region was defined and excluded from a fit to the invariant mass distribution. The resulting background fit was integrated and then subtracted from the bins in the signal region. The results are plotted in figure 6.6.

The top figure shows the ratio of the number of reconstructed K^0's produced

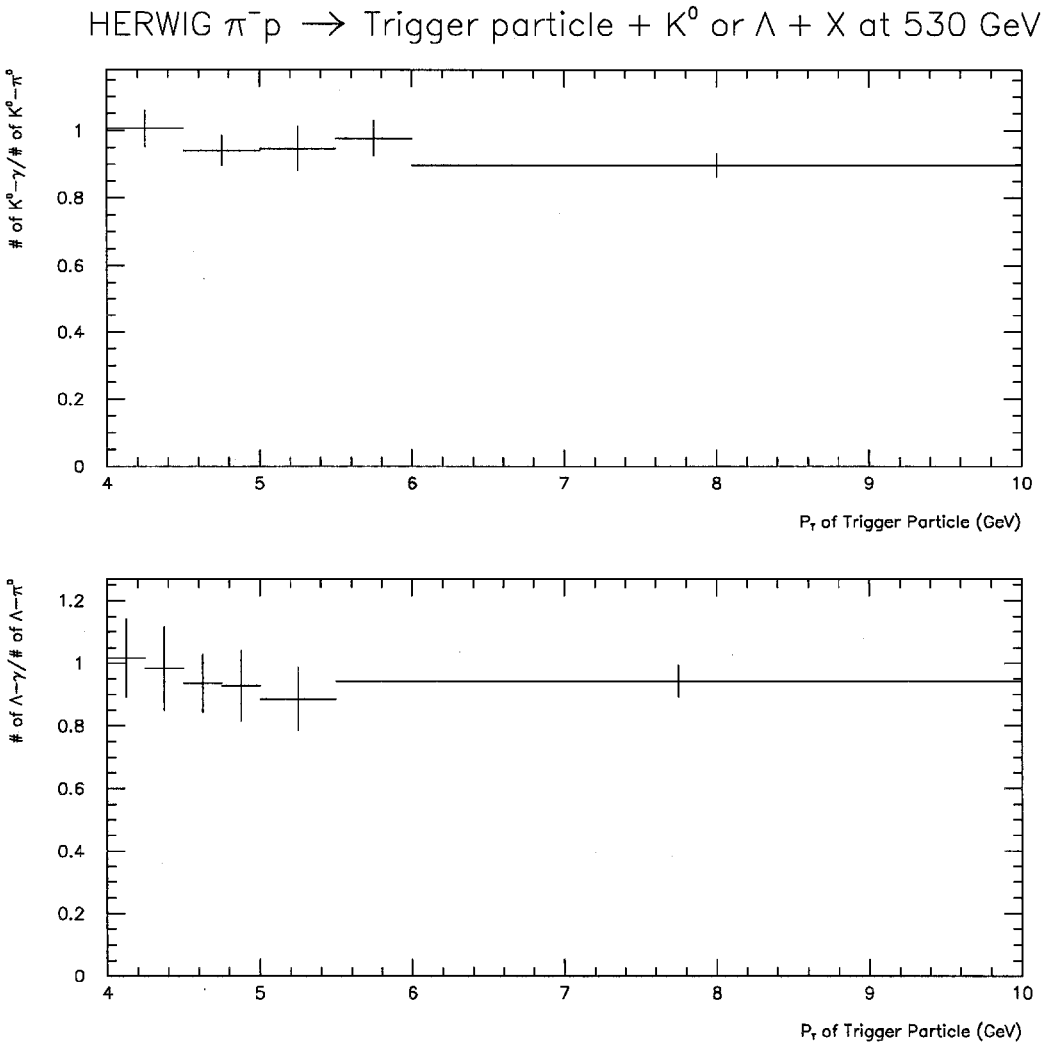

Figure 6.5: TOP: The ratio of the number of K^0's generated in the away side of direct photon triggered events to the number generated in the away side of π^0 triggered events. BOTTOM: The same plot as above for Λ's generated in the away side jet. The ratios are plotted as a function of the P_T of the π^0 or direct photon.

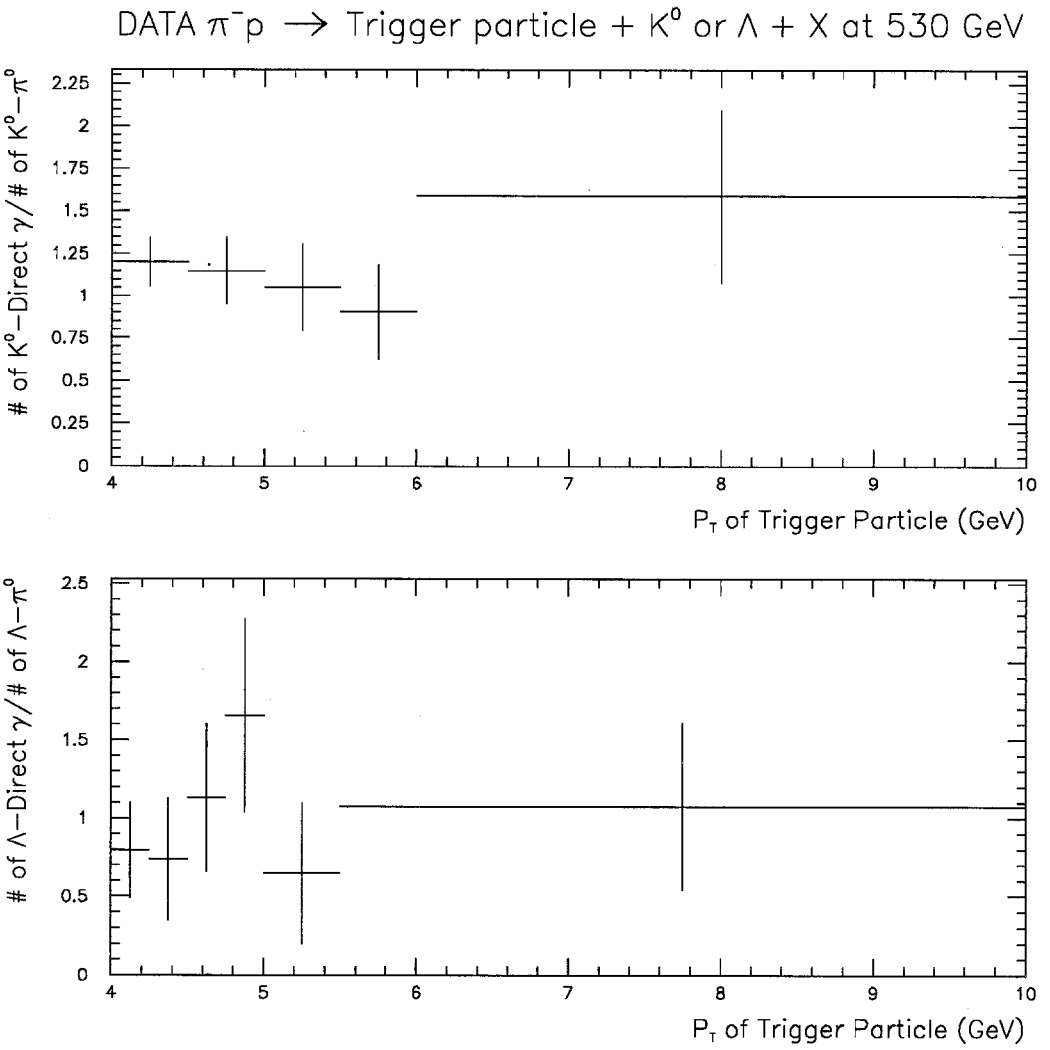

Figure 6.6: The ratio of the number of K^0's reconstructed in the away side of single photon triggered events to the number reconstructed in the away side of π^0 triggered events. The ratio is plotted as a function of the P_T of the π^0 or photon. The bottom plot shows the distribution for Λ's.

in away side jets opposite a direct photon trigger to the number reconstructed opposite a π^0 trigger. The distribution is consistent, within uncertainties, with no P_T dependence. The last bin (6.0 GeV $< P_T <$ 10.0 GeV) shows a possible deviation from unity but within a one sigma uncertainty. This is also true for the first bin. Fig 6.8 shows a direct comparison between HERWIG Monte Carlo, with detector effects included, and data.

The bottom plot in figure 6.6 shows the same distribution for the Λ ($\bar{\Lambda}$) sample. This sample contained both reconstructed Λ's and $\bar{\Lambda}$'s.

In order to study any dependence upon the π^0 background subtraction, the unsubtracted ratios are shown in figure 6.7.

6.5.3 HERWIG Predictions for K^0 and Λ Ratios vs. z

A ratio of fragmentation functions of strange particles was also studied. Figure 6.9 shows the HERWIG prediction for the ratio of fragmentation functions in gluon and quark jets. Again, detector effects are not included in these ratios. Studies [20] have shown that quark jets are harder than gluon jets. This behavior is modeled in HERWIG so the ratio has the expected shape (see figure 6.9.) The plots were made using two samples of HERWIG Monte Carlo events. The first sample has a minimum generated P_T of 3.0 GeV and the second, a minimum P_T of 5.0 GeV. In each case only trigger particles with P_T greater than the minimum plus 0.5 GeV were accepted. At the time of this study, a sample with minimum generated P_T of

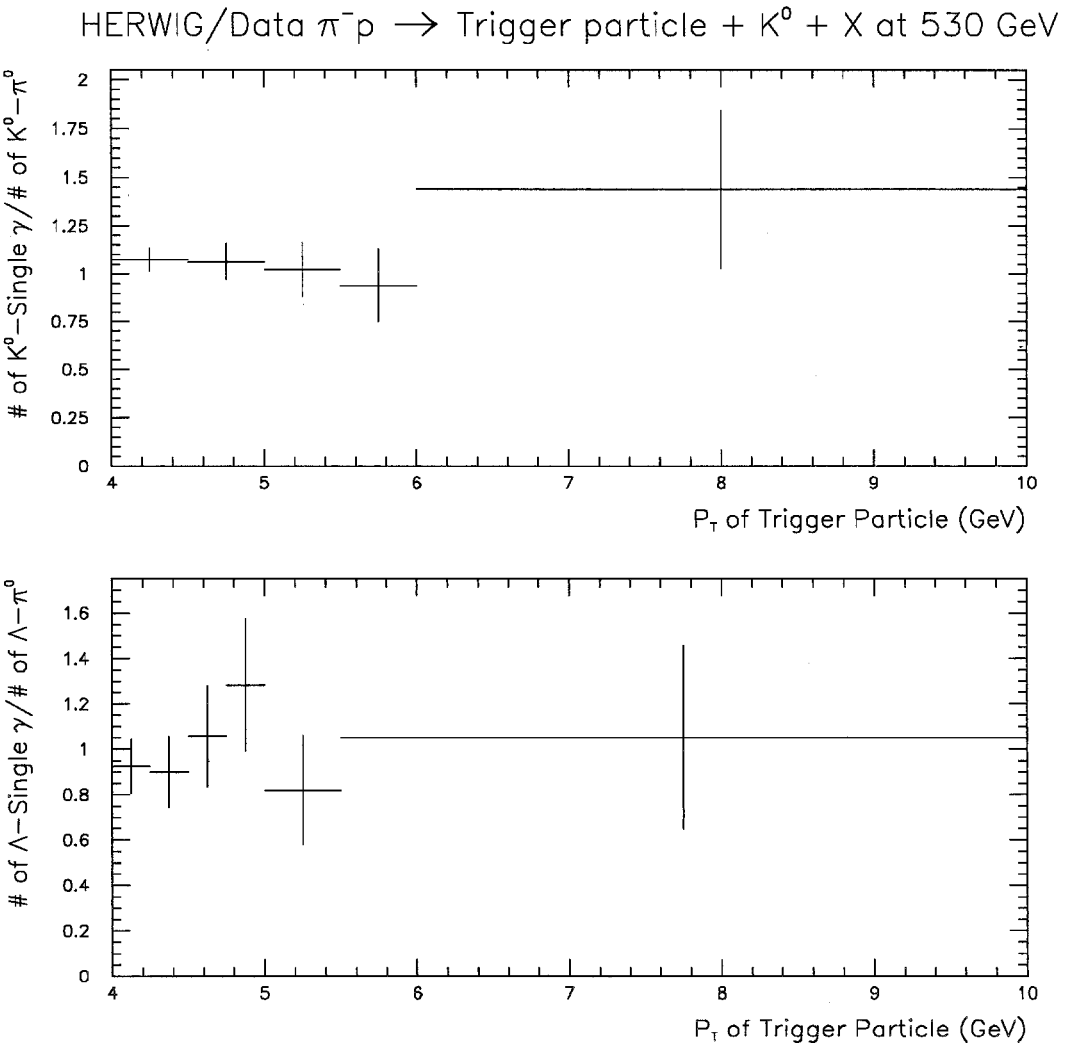

Figure 6.7: The ratio of the number of K^0's reconstructed in the away side of single photon triggered events to the number reconstructed in the away side of π^0 triggered events. The ratio is plotted as a function of the P_T of the π^0 or photon. The bottom plot shows the distribution for Λ's. The π^0 background subtraction has not been done for this ratio.

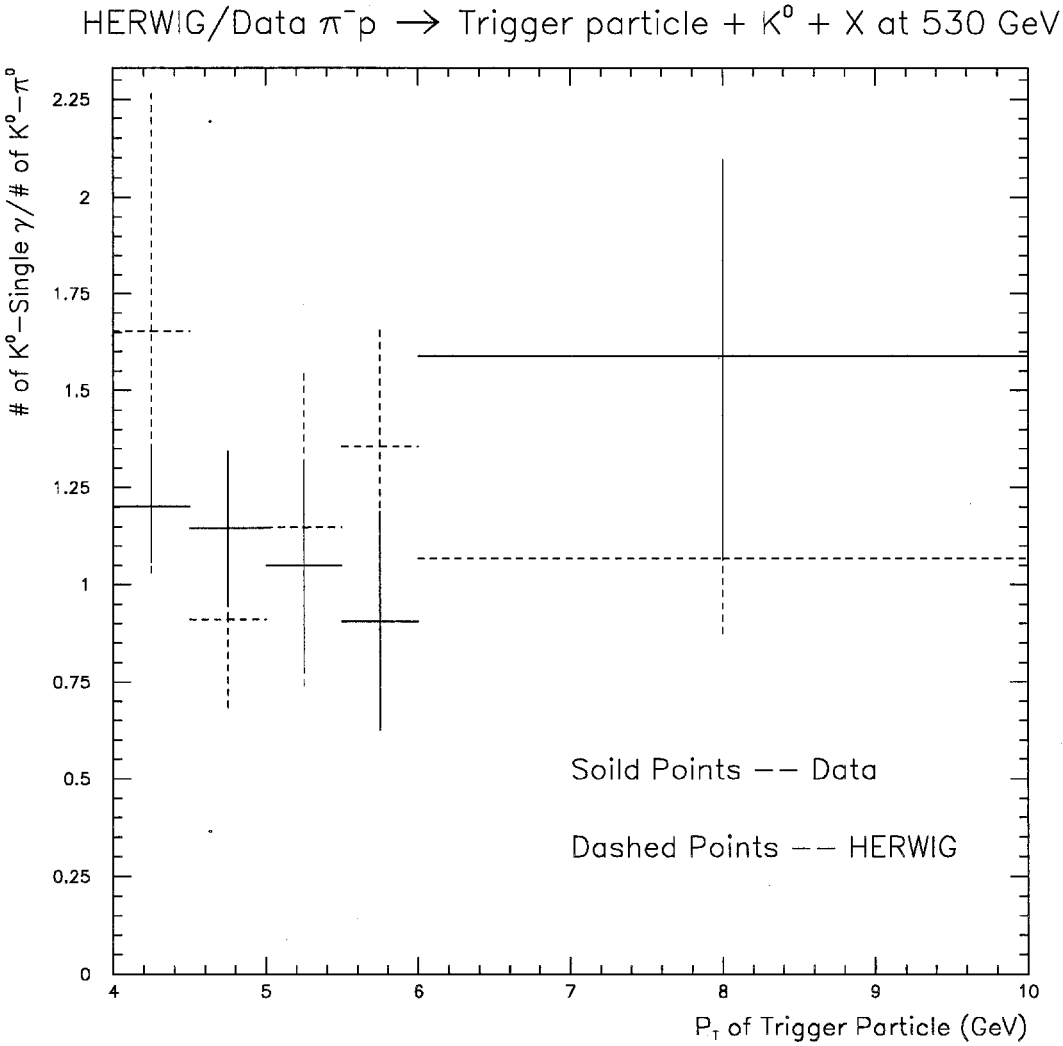

Figure 6.8: The ratio of the number of neutral kaons reconstructed in the awayside jet opposite single photon triggers to the number opposite π^0 triggers. Superimposed on this plot are the results using the HERWIG Monte Carlo with GEANT for detector simulation.

3.5 GeV (allowing a direct comparison with the data) was not available.

Figure 6.10 shows the HERWIG predictions for Λ's and $\bar{\Lambda}$'s. In these plots the difference between gluon initiated and quark initiated jets can also be seen.

Figure 6.11 shows the HERWIG prediction for the ratio of $\bar{\Lambda}$ to Λ separately in gluon and quark initiated away side jets for two values of minimum trigger particle P_T. In all the plots the average ratio is ≈ 0.6. A ratio less than one is expected since the Λ's are produced in the target jet as well as the away side jet while the $\bar{\Lambda}$'s are produced mainly in the away side jet.

When the ratio of single γ to π^0 events is plotted a slight z dependence is observed in the HERWIG Monte Carlo. The $P_T > 5.5$ GeV sample shows more of an effect than the $P_T > 3.5$ GeV sample (see figures 6.12 and 6.13.) This behavior is expected from examination of figure 1.5 which predicts a higher fraction of gluon jets for the higher P_T sample.

Finally figure 6.14 shows the ratios of $\bar{\Lambda}$ production to Λ production in away side jets.

When we examine this ratio in the data as a function of z of the K^0 we see a possible trend. It looks as if the number of kaons produced on the away side of direct photons initially increases as a function of z until a plateau at ≈ 1.25 around z $= 0.2$. However, this is only a one sigma effect and the distribution is also consistent with no z dependence. The error bars shown represent statistical errors only. (See figure 6.15.)

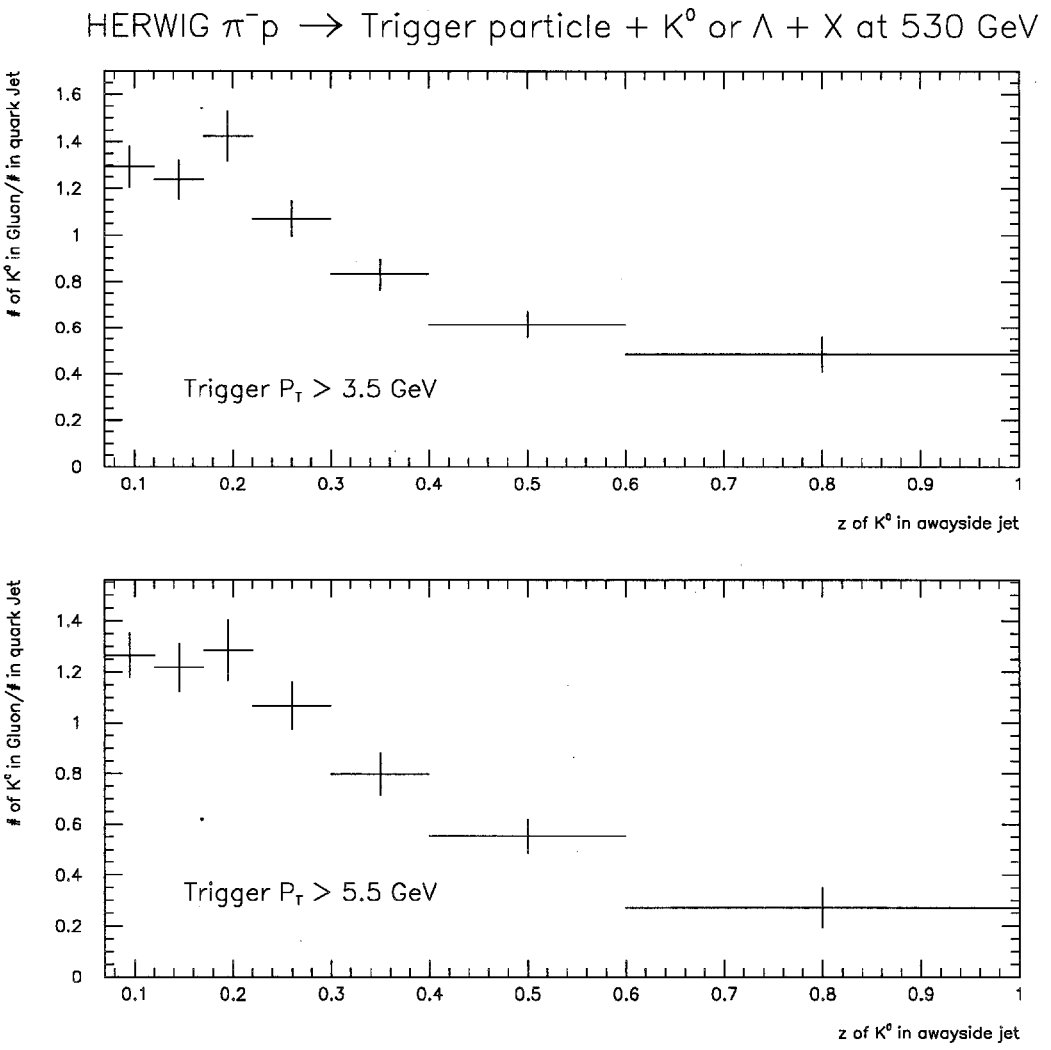

Figure 6.9: The ratio of the number of K^0's generated in gluon initiated away side jets to the number generated in quark initiated away side jets. Detector effects are not included. The away side jets are in a cone of radius 1 opposite to a π^0 or single photon with a minimum P_T of 3.5 GeV (top) or 5.5 GeV (bottom). The ratio is plotted as a function of z of the K^0. Both plots show that HERWIG predicts a harder z distribution for quark initiated jets than for gluon initiated jets.

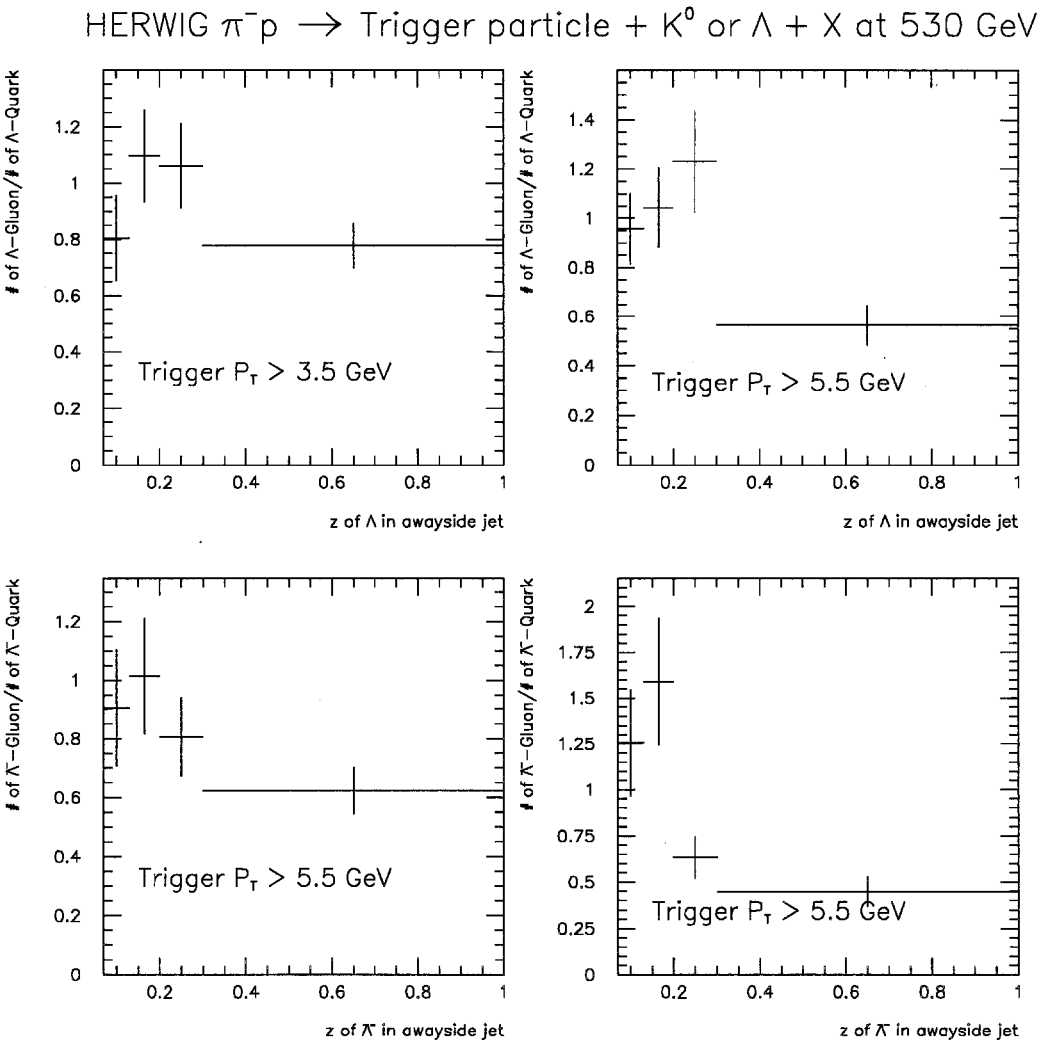

Figure 6.10: (a) The ratio of the number of Λ's generated in gluon initiated away side jets to the number generated in quark initiated away side jets with trigger $P_T >$ 3.5 GeV. (b) The same ratio as (a) with trigger $P_T > 5.5$ GeV. (c) The same ratio as (a) but for $\bar{\Lambda}$'s. (d) The same ratio as (c) with trigger $P_T > 5.5$ GeV. The ratios are plotted as a function of z of the Λ or $\bar{\Lambda}$.

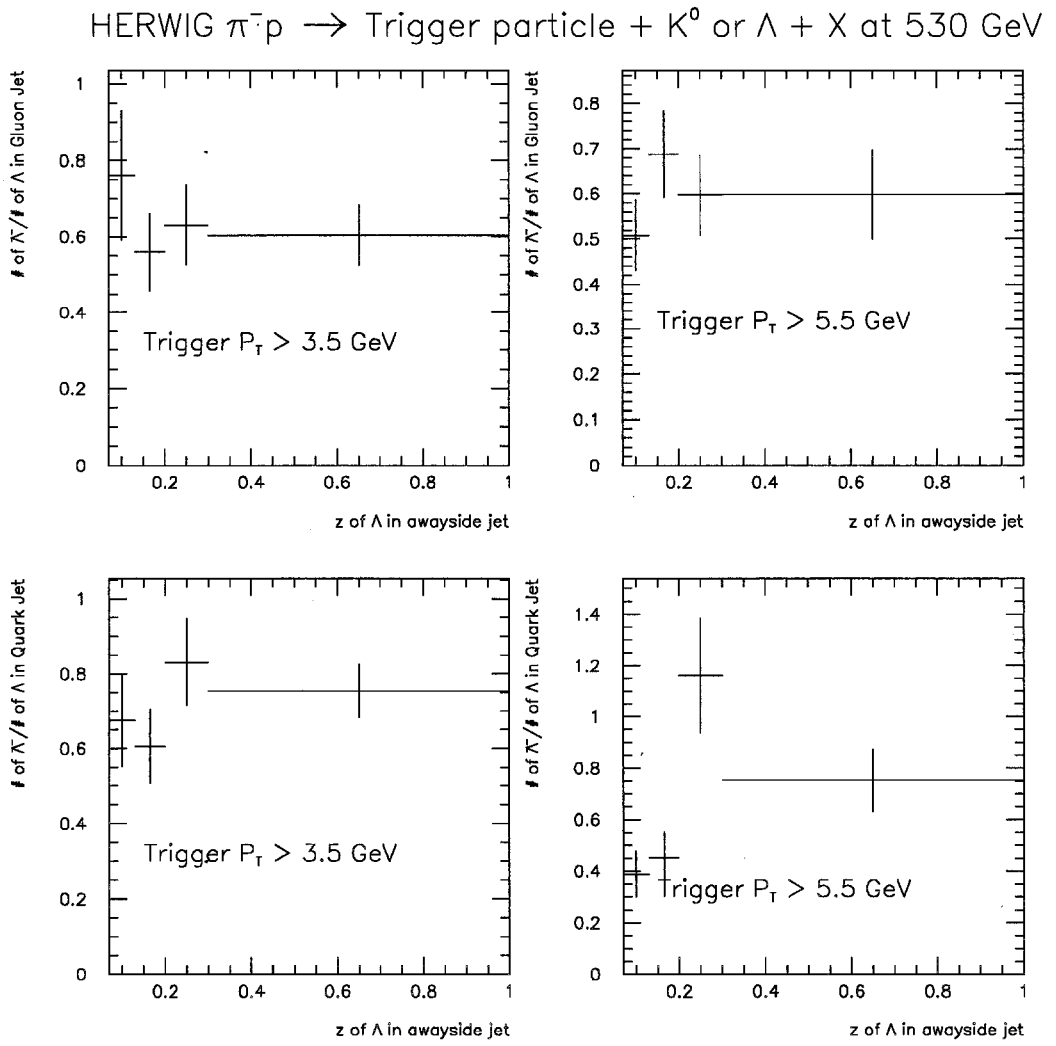

Figure 6.11: (a) The ratio of the number of $\bar{\Lambda}$ to Λ's generated in gluon initiated away side jets with trigger $P_T > 3.5$ GeV. (b) The same ratio as (a) with trigger $P_T > 5.5$ GeV. (c) The same ratio as (a) but for quark initiated away side jets. (d) The same ratio as (c) with trigger $P_T > 5.5$ GeV. The ratios are plotted as a function of z of the Λ or $\bar{\Lambda}$.

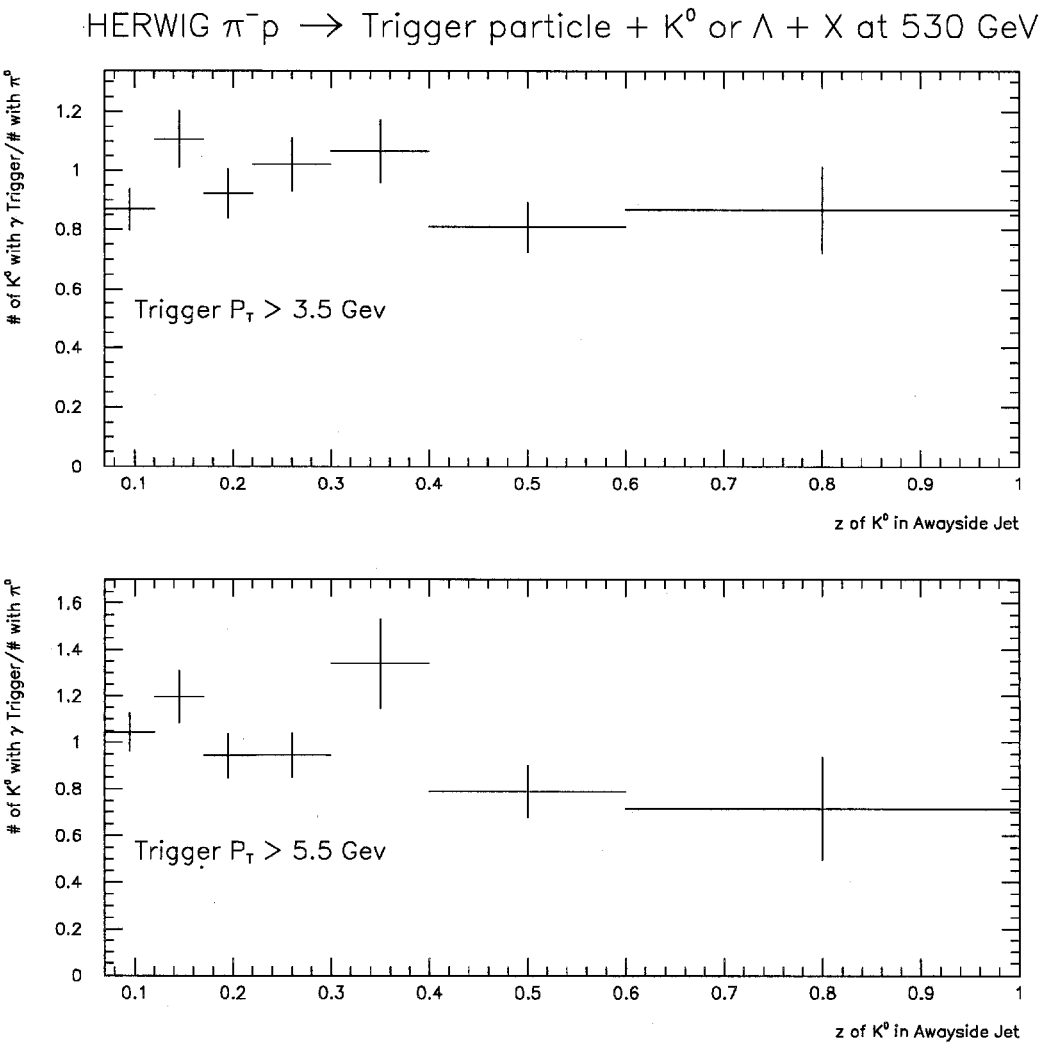

Figure 6.12: The ratio of the number of K^0's generated in the away side of direct photon triggered events to the number generated in the away side of π^0 triggered events versus z. The top plot shows the $P_T > 3.5$ GeV sample and the bottom shows the $P_T > 5.5$ GeV sample.

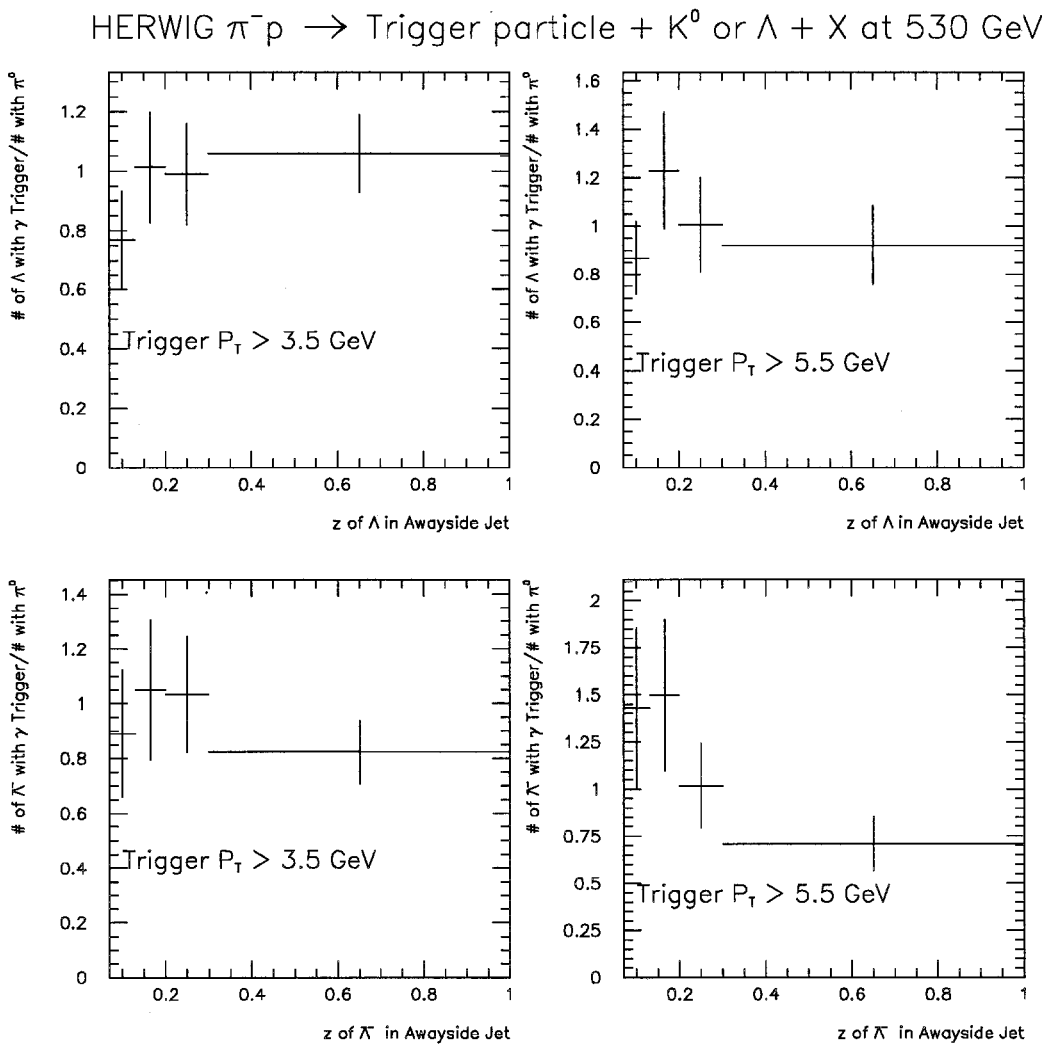

Figure 6.13: The ratio of the number of Λ's and $\bar{\Lambda}$'s generated in the away side of direct photon triggered events to the number generated in the away side of π^0 triggered events versus z.

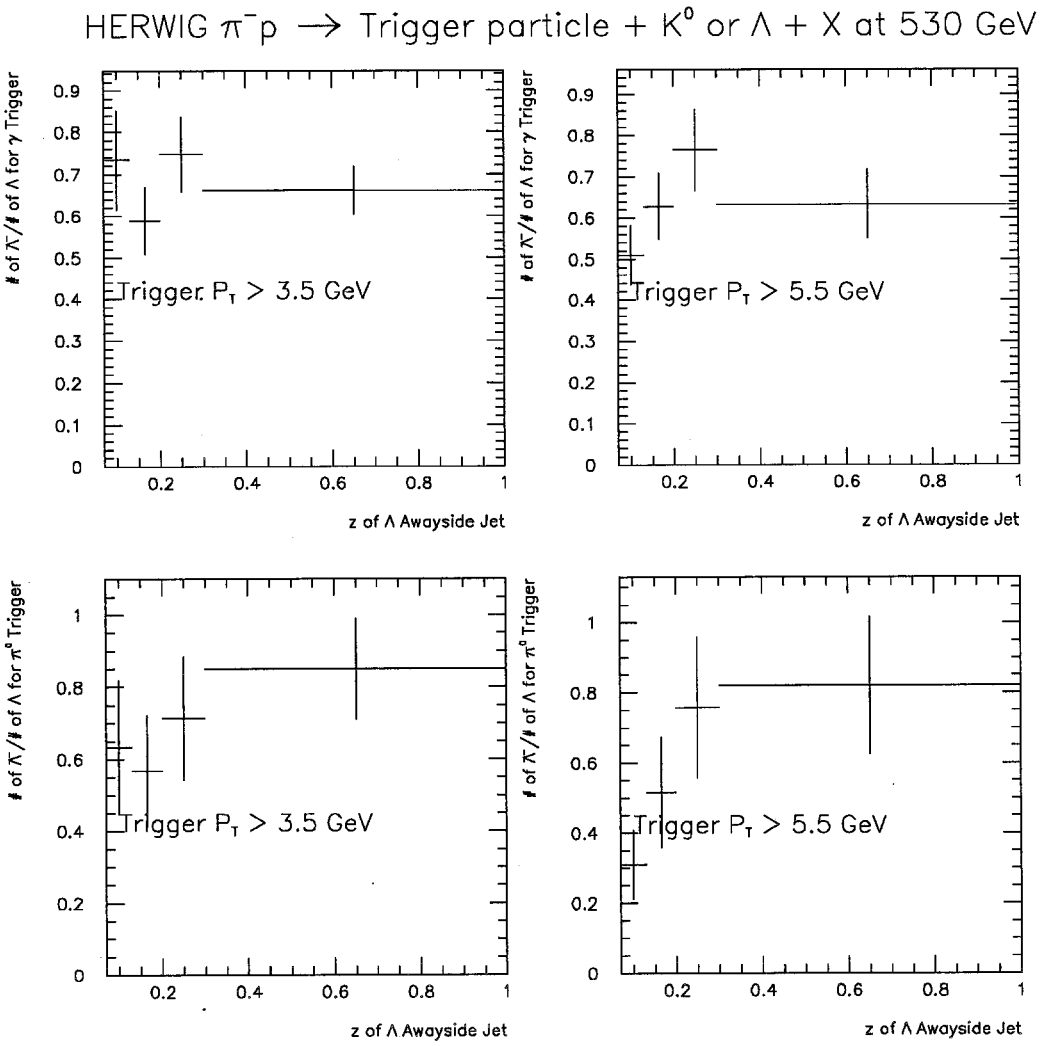

Figure 6.14: The ratio of the number of $\bar{\Lambda}$'s generated in the away side of direct photon or π^0 triggered events to the number of Λ's generated in the away side of direct photon or π^0 triggered events versus z.

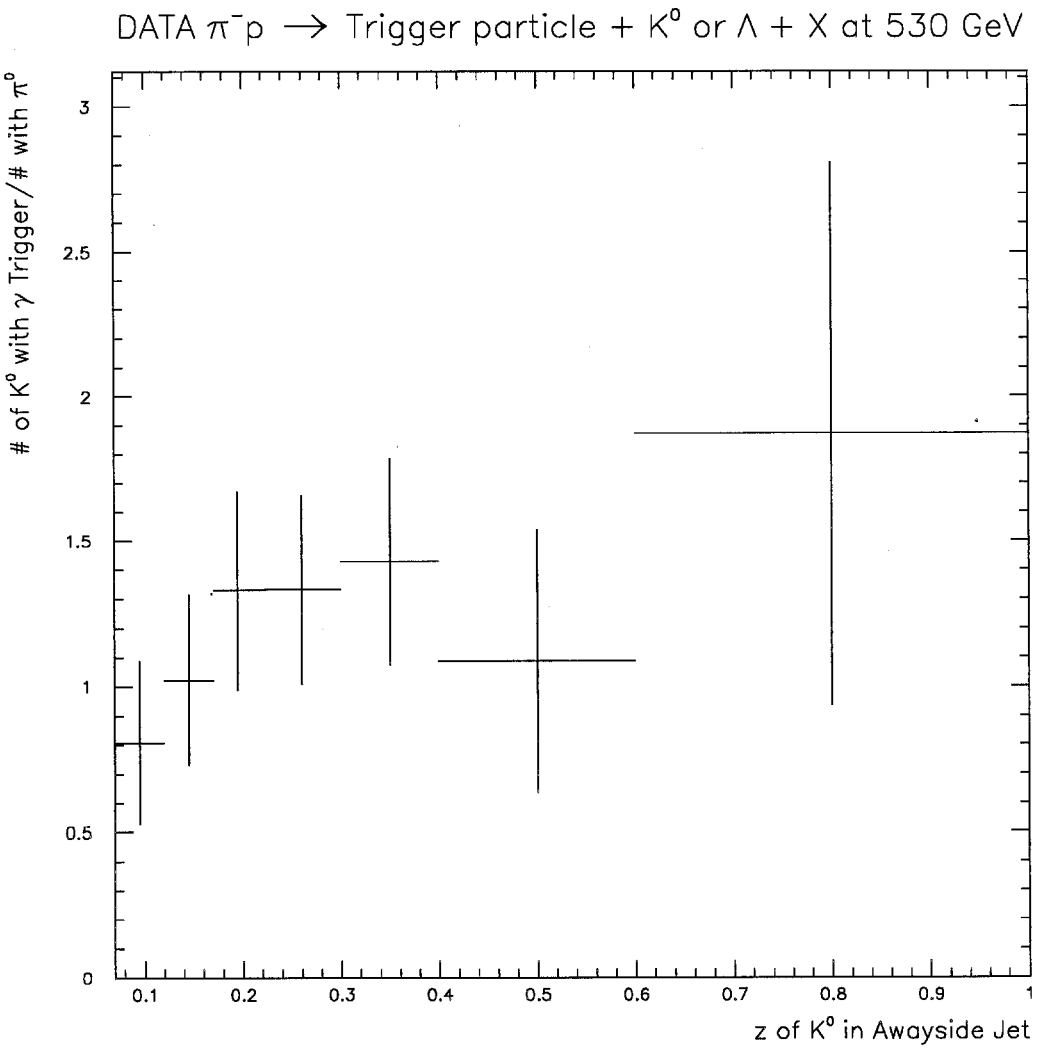

Figure 6.15: The ratio of the number of K^0's reconstructed in the away side of direct photon triggered events to the number reconstructed in the away side of π^0 triggered events. The ratio is plotted as a function of the z of the K^0.

The Λ and $\bar{\Lambda}$ ratios are also consistent with unity within errors. All errors shown represent statistical errors only. No account has been taken of any systematic errors which may exist. (See figure 6.16.)

Figure 6.17 shows the ratio of the number of $\bar{\Lambda}$'s to the number of Λ's reconstructed in the away side jet opposite a direct photon or π^0 trigger. As predicted by HERWIG, there are fewer $\bar{\Lambda}$ produced compared to Λ. Within errors, the distributions are consistent with having no z dependence.

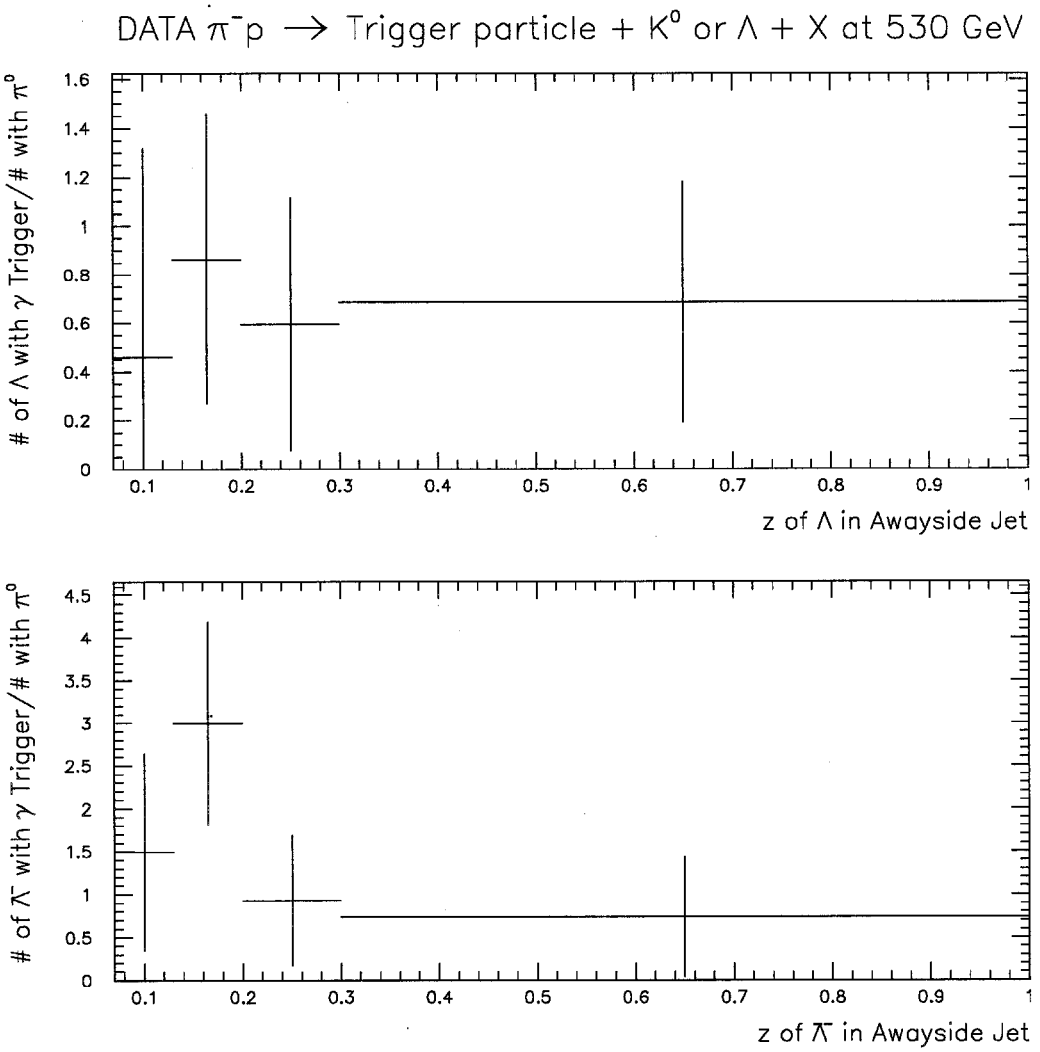

Figure 6.16: TOP: The ratio of the number of Λ's generated in the away side of direct photon triggered events to the number of Λ's generated in the away side of π^0 triggered events versus z. BOTTOM: The same ratio for $\bar{\Lambda}$.

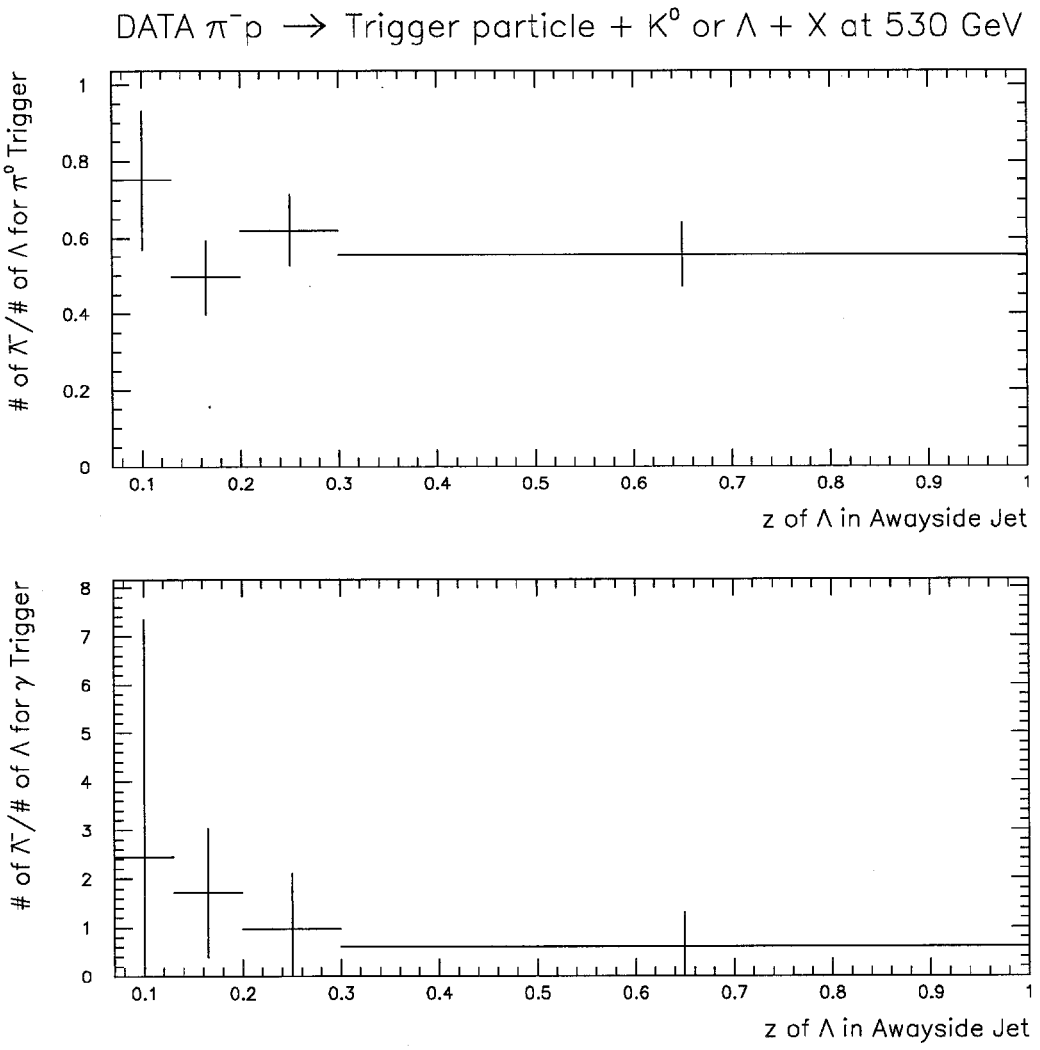

Figure 6.17: The ratio of the number of $\bar{\Lambda}$'s to the number of Λ's reconstructed in the away side of direct photon (BOTTOM) and π^0 (TOP) triggered events.

Chapter 7

Conclusions

One of the outstanding questions that QCD does not address is that of the fragmentation of quarks and gluons into hadron jets. This long range behavior is outside of our current expertise in the theory. Instead, we must rely on phenomenological models which in turn rely heavily on input from experiments. One important aspect of the current fragmentation model is the question as to whether there are differences in the properties of quark and gluon initiated hadron jets.

One of the properties worthy of study is the difference in particle content between quark and gluon jets. e^+e^- experiments studying $\Upsilon \rightarrow g + g + g$ decays have published many results in this area [40, 41, 42]. By comparing data taken on the resonance with data taken in the nearby continuum, DASP2, CLEO, and ARGUS have found that there are more protons in gluon jets as well as more hyperons [39]. ARGUS gave the ratio for Λ production on and off the resonance as 2.9 ± 0.4 [40].

Using the properties of direct photon triggered π^-N interactions, discussed in chapter 1, we were able to study samples consisting of a majority of gluon initiated awayside jets. Using a study [20] with the HERWIG Monte Carlo generator, we were able to make the conclusion that our π^0 triggered data sample would have a majority of quark initiated away-side jets. We examined the ratios of the number of strange particles produced in direct photon to the number produced in π^0 triggered events vs. P_T and the fragmentation momentum fraction, z. The K^0 comparisons were made in a P_T range between 4.0 and 10.0 GeV. In this range, the HERWIG prediction for the ratio of K^0 production in direct photon to π^0 triggered events was consistent with no dependence on trigger particle P_T. The same ratio in the data showed good agreement with the HERWIG sample. The χ^2 between the two samples was used as a measure of their agreement. The calculated χ^2 was 4.96 for 5 degrees of freedom. The probability of getting this value of χ^2 or higher is 0.42. The χ^2 values and their associated probabilities are shown in table 7.1.

The ratio vs. P_T comparison was also made for Λ and $\bar{\Lambda}$ baryons. There is good agreement between the HERWIG sample and the data. The calculated χ^2 was 2.61 with a probability of 0.85 for getting this χ^2 or higher. Recall that at High P_T the fraction of qluon to quark awayside jets increases with the direct photon trigger. No indication of the excess Λ baryon effect seen in the above mentioned experiments was seen here. In the highest P_T bin we expect approximately 60% gluon purity (See chapter one). A higher statistics sample is needed in order to further investigate

this effect.

A comparison of K^0 production in the away-side jet between direct photon and π^0 triggered events using the HERWIG event generator was consistent with no z dependence for the 3.5 GeV HERWIG sample. The 5.5 GeV sample possibly showed a sight z dependence, but within uncertainties it was also consistent with no dependence.

The same ratio in the data was also consistent with no z dependence. Here the χ^2 was 3.45 with a probability of 0.84 of getting this χ^2 or higher when compared with the monte carlo. This is the behavior expected since the contribution of the annihilation and Compton subprocesses are about equal at a direct photon trigger P_T of 4.0 GeV. Due to the steeply falling nature of the P_T spectrum, most of the triggered events have a P_T of 4.0 GeV.

In both the K^0 and $\Lambda(\bar{\Lambda})$ samples, no z dependence can be claimed. In both cases, however, more statistics are needed to make definite statements.

Finally, a comparison of the number of $\bar{\Lambda}$ to the number of Λ produced was made for each type of trigger particle as a function of z. For the HERWIG Monte Carlo, the 3.5 GeV direct photon triggered sample is consistent with no z dependence, while the π^0 sample is shows a possible increase in the ratio with increasing z. Both of the 5.5 GeV P_T triggered samples show possible z dependences, increasing with increasing z, for both types of trigger particle.

The data, analyzed with a 4.0 GeV P_T cut, is consistent with being independent of z for both types of trigger particle. However, using the χ^2 method described above, it is also shown that there is good agreement between the data and HERWIG (see table 7.1).

Both the data and the Monte Carlo show a $\frac{\bar{\Lambda}}{\Lambda}$ ratio of less than unity. This is expected since the $\bar{\Lambda}$ are produced mainly in the recoil jet while the Λ's are produced not only in the recoil jet, but in the target jet as well. The actual value of the ratio will depend on the radius that we use in the cone algorithm jet definition. A smaller radius would tend to bring the ratio closer to one, since there would be less overlap of the target and recoil jets in η—ϕ space. This argument also suggests a reason why one might expect a z dependence in this ratio. Z is a measure of the fraction of the struck quark's momentum that has been imparted to the given hadron. Hadrons with smaller values of z are more likely to come from the overlap of the spectator jets than are particles with larger z values. There is good agreement between data and the HERWIG predictions as shown in table 7.1.

Fragmentation Ratio γ/π^0

$P_T > 3.5$ GeV Sample		$P_T > 5.5$ GeV Sample	
χ^2	Probability	χ^2	Probability
3.45	0.84	5.73	0.62
1.23	0.87	1.29	0.86
2.85	0.58	1.44	0.84

Fragmentation Ratio $\bar{\Lambda}/\Lambda$

$P_T > 3.5$ GeV Sample		$P_T > 5.5$ GeV Sample	
χ^2	Probability	χ^2	Probability
3.85	0.43	6.51	0.16
0.89	0.93	0.86	0.93

Trigger Particle P_T Ratio

$P_T > 3.5$, 4.5, 5.5, 6.5, 8.5 Sample	
χ^2	Probability
4.96	0.42
2.61	0.85

Table 7.1: χ^2 of comparisons of data and HERWIG Generated results. Also shown is the probability of getting this χ^2 or greater. The first three rows are for the fragmentation ratios for K^0_{Short}'s, Λ's, and $\bar{\Lambda}$'s respectively. The middle two rows are the χ^2 and associated probabilities for comparisons, between HERWIG and data, of the $\bar{\Lambda}/\Lambda$ ratios for π^0 and direct photon triggers, respectively. The last two rows are for ratios vs. trigger particle P_T for K^0_{Short}'s and Λ's. A high probability (~ 0.5) suggests good agreement between data and HERWIG.

Bibliography

[1] Vernon D. Barger and Roger J.N. Phillips. *Collider Physics Frontiers In Physics Lecture Note Series*, Addison-Wesley Publishing Company, 1987

[2] Stanley J. Brodsky, *Quantum Chromodynamics And The Dynamics Of Hadrons*, AIP Conference Proceedings No. 55, Particles And Fields Subseries, No. 18, Quantum Chromodynamics, American Institute of Physics, New York, 1979.

[3] Francis Halzen, Alan D. Martin, *Quarks and Leptons: An introductory course in modern particle physics*, John Wiley And Sons Inc., New York, 1984

[4] Perkins, *Introduction to High Energy Physics*, John Wiley and Sons Inc., New York, 1989

[5] J.F. Owens, *Large–momentun–transfer production of direct photons, jets, and particles*, Reviews of Modern Physics, April 1987, Volume 59, Number 2

[6] T. Ferbel, W.R. Molzon, *Direct–photon production in high–energy collisions*, Reviews of Modern Physics, April 1984 Volume 56, Number 2, Part 1

[7] G. Marchesini, B.R. Webber, G. Abbiendi, I.G. Knowles, M.H. Seymour, and L. Stanco, *HERWIG 5.1 – a Monte Carlo event generator for simulating hadron emission reactions with interfering gluons*, Computer Physics Communications, 23 May 1991, Volume 67

[8] G. Marchesini, B.R. Webber, *Monte Carlo simulation of general hard processes with coherent QCD radiation* , Nuclear Physics B, 8 February 1988, volume 310

[9] ZEUS Collaboration, *Neutral Strange Particle Production In Deep Inelastic Scattering at Hera*, hep-ex/9505011, 18 May 1995

[10] WA89 Collaboration, *Measurement of the polarization of* Λ^0, $\bar{\Lambda}^0$, Σ^+, *and* Ξ^- *produced in a* Σ^- *beam of 330 GeV/c*, CERN-PPE/94-86, 8 June 1994

[11] E632 Collaboration, *Neutral strange particle production in neutrino and antineutrino charged–current interactions on neon*, Physical Review D, 1 December 1994, Volume 50, Number 11

[12] Fermilab E665 Collaboration, *Production of neutral strange particles in muon–nucleon scattering at 490 GeV*, Zeitschrift für Physik C, 19 November 1993, volume 61

[13] Birmingham-CERN-Imperial College-München (MPI)–Oxford-University College London Collaboration (WA21), *Neutral strange particle production in neutrino and antineutrino charged current interactions on protons*, Zeitschrift für Physik C, 27 August 1992, volume 57

[14] Fermilab E799 Colaboration, *Polarization of* Λ*, and* $\bar{\Lambda}$ *produced by 800–GeV protons*, Physics Letters B, 23 August 1994, volume 338

[15] HRS Collaboration, *Study of Inclusive* Λ *production in* e^+e^- *annihilations at 29 GeV*, Physical Review D, 8 July 1991, volume 45, Number 11

[16] NA36 Collaboration, *Target dependence of central rapidity* Λ *production in sulfer–nucleus collisions at 200 GeV/c per nucleon*, Physical Review C, 26 December 1991, Volume 46, Number 2

[17] WA85 Collaboration Λ *and* $\bar{\Lambda}$ *production in sulfer-tungsten interactions at 200 GeV/c per nucleon*, Physics Letters B, 10 April 1990, Volume 244, Number 1

[18] HELIOS Collaboration, *Kaon production in 200 GeV/nucleon nucleus–nucleus collisions* Physics Letters B, 30 June 1992, Volume 296

[19] ACCMOR Collaboration, *A Study of the transverse polarization of* Λ^0 *and* $\bar{\Lambda}^0$ *hyperons produced in* π^-*–Cu interactions at 230 GeV/c*, Physics Letters B, 25 February 1994, Volume 325

[20] Woohyun Chung, *Jet Production in proton–Be interactions at 515 GeV/c*, Ph.D Thesis, University of Pittsburgh, June 1995

[21] Vijay Kapoor, *Fragmentation properties of strange particles produced in high transverse momentum hadronic interactions*, Ph.D Thesis, University of Delhi, October 1990

[22] Particle Data Group, *Particle Physics Booklet*, July 1994

[23] R.J. Miller, *A Measurement of the E706 Beam Momentum for the 1990 Negative Runs*, E706 Note

[24] Robert Martin Roser, *Eta Production at High Transverse Momentum by Negative 520 GeV/c Pions Incident on Beryllium and Copper Targets*, Ph.D Thesis, University of Rochester, 1994

[25] Nikos Varelas, π^0 *Production at High Transverse Momenta from* π^- *Collisions at 520 GeV/c on Be and Cu Targets*, Ph.D Thesis, University of Rochester, 1994

[26] David Shaw Brown, *A COMPARISON OF HIGH TRANSVERSE MOMENTUM DIRECT PHOTON AND NEUTRAL PION EVENTS IN NEGATIVE PION AND PROTON-NUCLEUS COLLISIONS AT 31.5 GeV CENTER OF MASS ENERGY*, Ph.D Thesis, Michigan State University, 1992

[27] P.D.D.S. Weerasundara, *A Study of Large Transverse Momentum Direct Photons plus Away-Side Jet Production using 500 GeV/c proton and π^- Beams Incident on a Beryllium Target*, Ph.D Thesis, University of Pittsburgh, 1993

[28] Wieslaw Dlugosz, *The Production of High $p_T\pi^0$ Mesons in 515 GeV/c π^- – Nucleus Collisions*, Ph.D Thesis, Northeastern University, Boston, Massachusetts, August 1994

[29] Paoti Chang, *Massive $\pi^0\pi^0$, $\pi^0\pi^-$, $\pi^0\pi^+$ Production from 515 GeV/c π^- Collisions with Beryllium and Copper Targets*, Ph.D Thesis, Northeastern University, Boston, Massachusetts, August 1994

[30] William Desoi, *A Finely Segmented, High Resolution Electromagnetic Calorimeter*, Ph.D Thesis

[31] David Striley, private communication, University of Mosouri, Columbia

[32] Steve Blusk, private communication, University of Pittsburgh

[33] Richard C. Fernow, *Introduction to experimental particle physics* , Cambridge University Press, 1983

[34] Lee Sorrell, *The E706 Trigger System*, E706 Internal Note Number 201, September 21, 1994

[35] Lee Ronald Sorrell, *Measurement of the Nuclear Dependence of Direct Photon and Neutral Meson Production at High Transverse Momentum by Negative 515 GeV/c Pions Incident on Beryllium and Copper Targets*, Ph.D Thesis, Michigan State University, April 1995

[36] Andre Maul, *A thesis as yet untitled and unpublished* Ph.D Thesis, Michigan State University, 1996

[37] Steve Blusk, *Measurement Of The Production Cross Section Of Charm Mesons At High Transverse Momentum In 515 GeV/c π^-–Nucleon Collisions*, Ph.D Thesis, University of Pittsburgh, 1995

[38] Carl Bromberg, Michigan State University, Private Communication, 1994

[39] Roger Barlow *Jets in high-energy interactions* Reports on Progress in Physics 1993 Volume 56 pp1067-1143

[40] The Argus Collaboration *Observation of octet and decuplet hyperons in e^+e^- annihilation at 10 GeV center-of-mass energy.* Physics Letters B 15 January 1987 Volume 183, number 3,4

[41] P. Avery et al *Hyperon Production in e^+e^- Interactions in the Upsilon Region* Physical Review Letters 2 July 1984 Volume 53, Number 1 pp24-27

[42] H. Albrecht et al (DSP2 Collaboration) *Inclusive Hadron Production in the Υ–Region* Physics Letters 18 June 1981 Volume 102B, number 4 pp291-295

[43] Roland Waldi *ARGUS Results on Quark and Gluon Fragmentation* Proceedings Joint Intertional Lepton–Photon Symposium and Europhysics conference on HEP 1991 Volume 1 pp424-427

E706 Strange Particle Production

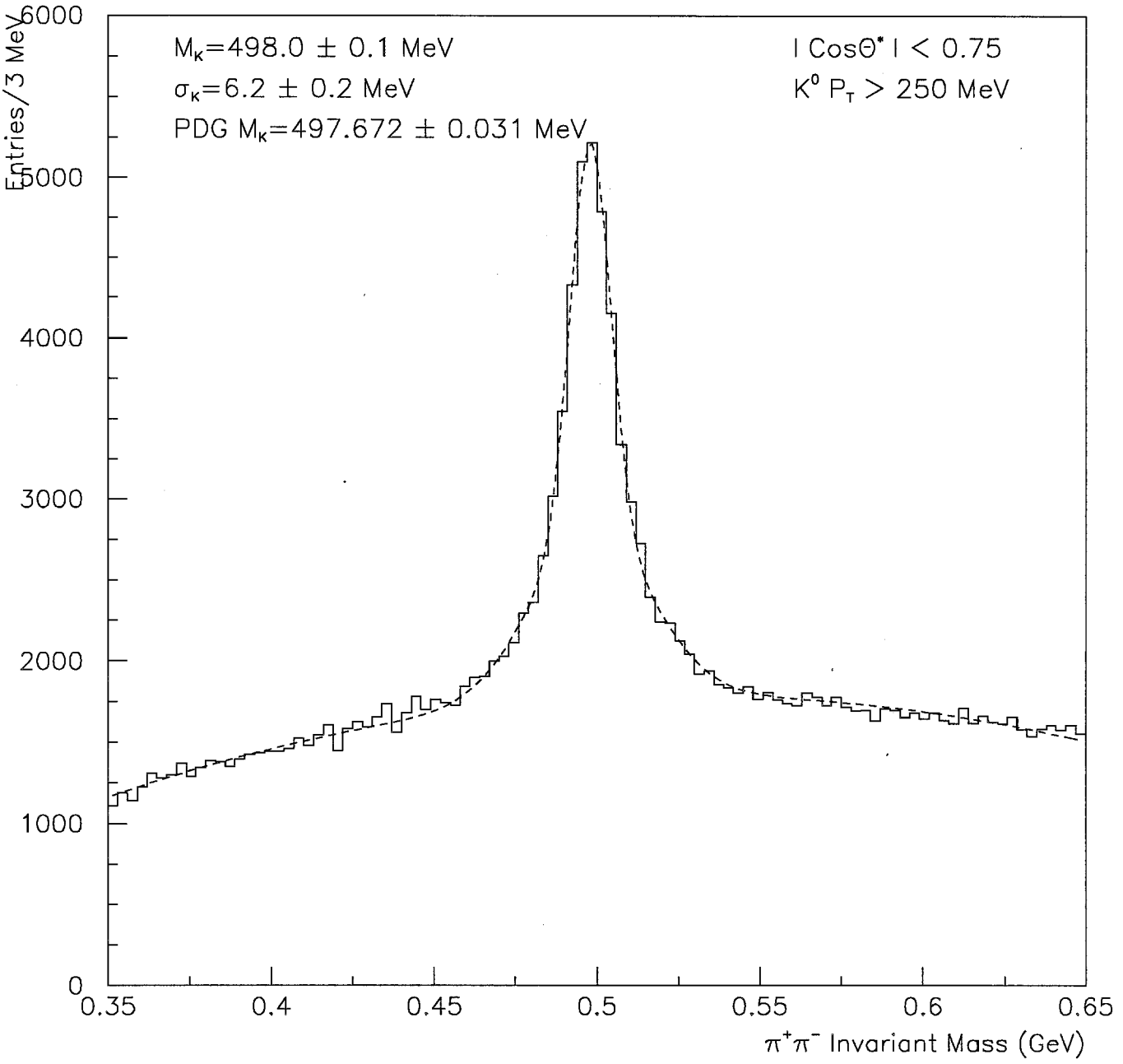

E706 Strange Particle Production

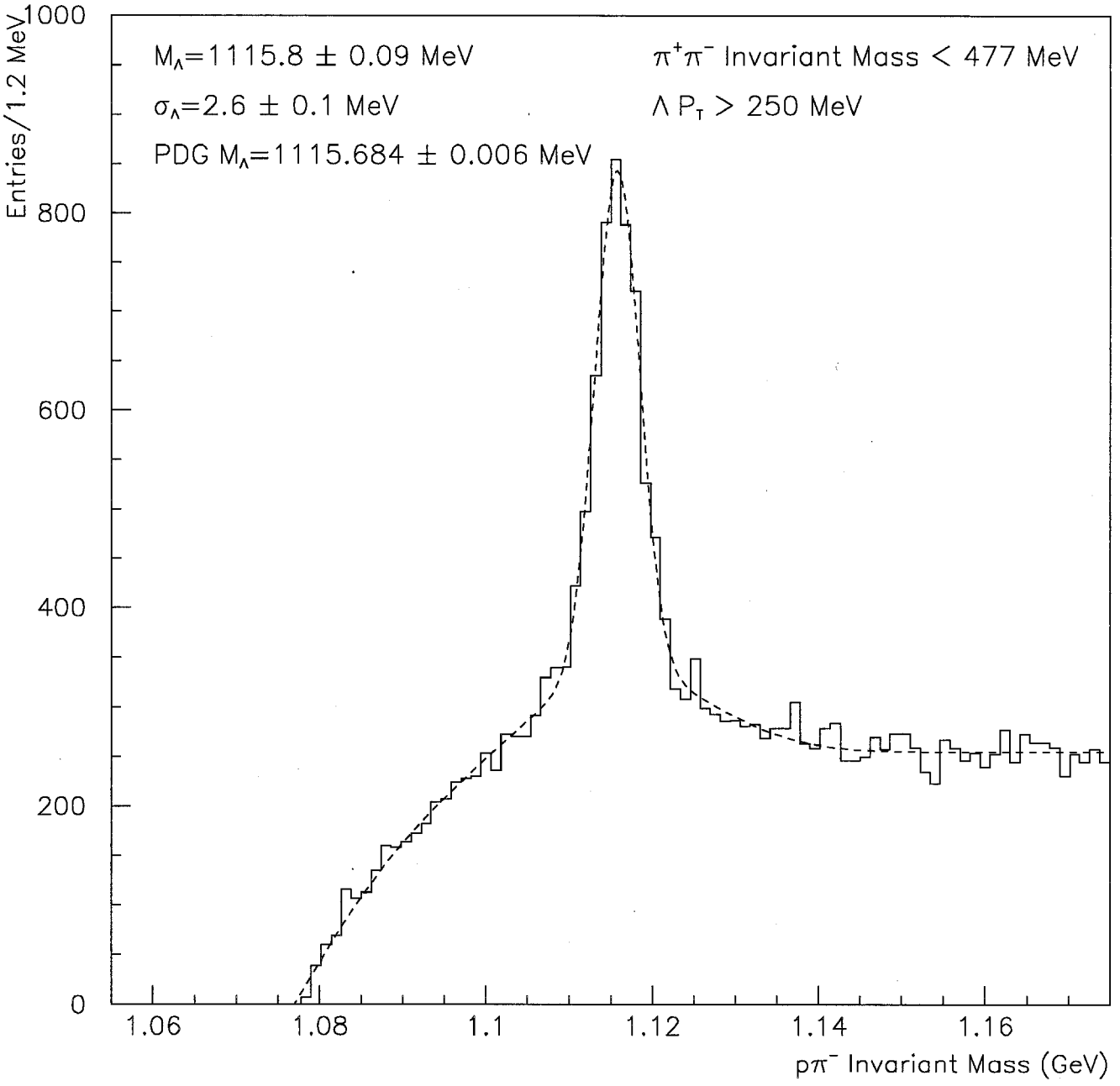

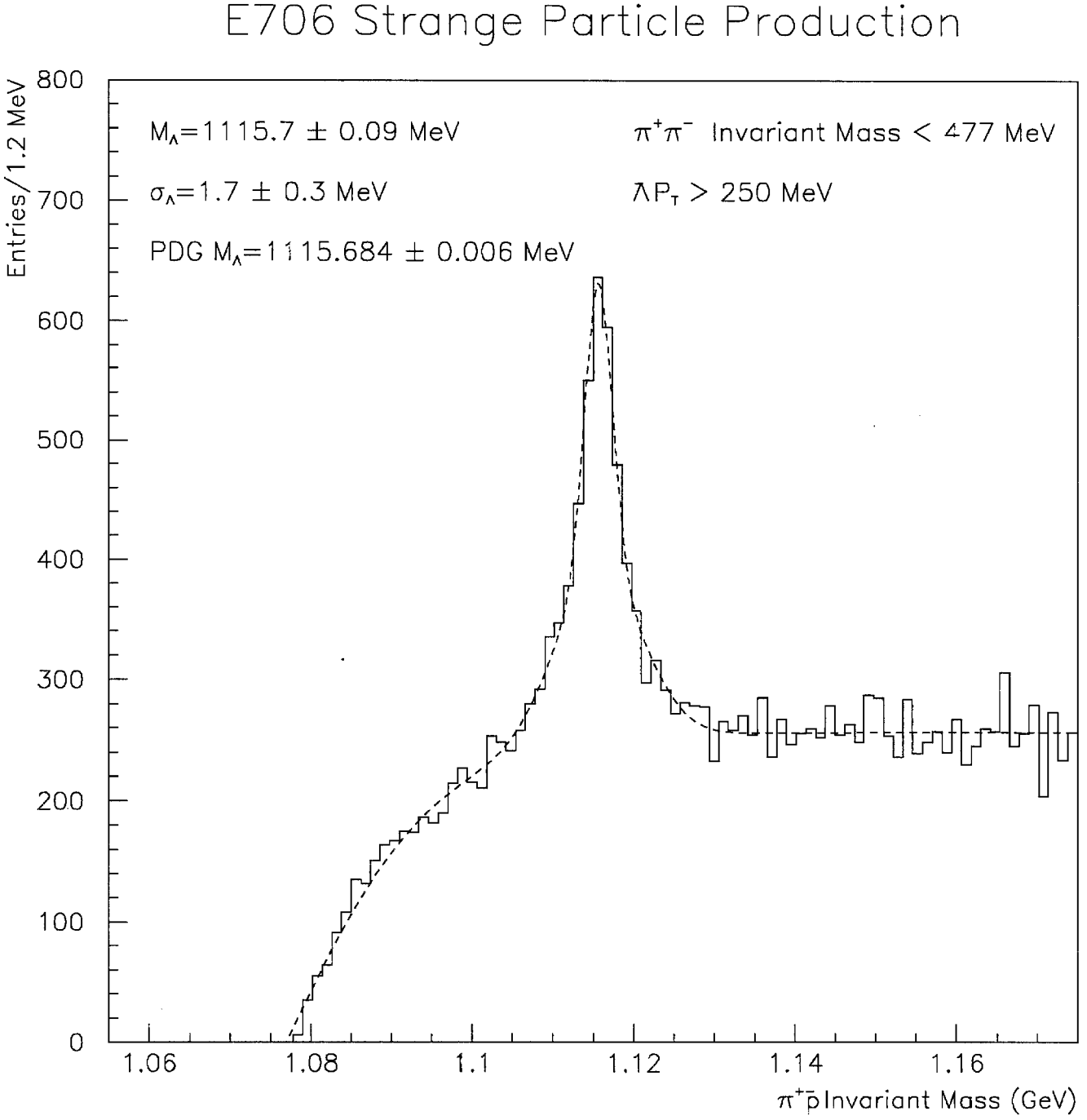
E706 Strange Particle Production
M_Λ=1115.7 ± 0.09 MeV
σ_Λ=1.7 ± 0.3 MeV
PDG M_Λ=1115.684 ± 0.006 MeV
$\pi^+\pi^-$ Invariant Mass < 477 MeV
ΛP_T > 250 MeV
Entries/1.2 MeV
0
100
200
300
400
500
600
700
800
1.06
1.08
1.1
1.12
1.14
1.16
$\pi^+\bar{p}$ Invariant Mass (GeV)